THE UNIVERSITY *of* EDINBURGH

A Study of Magnetic Fluctuations and Ordering in Uranium Compounds by Heat Capacity and Neutron Scattering Measurements

Oliver John Entwisle

Doctor of Philosophy
The University of Edinburgh
April 2018

Abstract

URhGe is the first ferromagnet discovered that shows superconductivity at ambient pressure. It shows a rich temperature-magnetic field phase diagram with a re-emergence of superconductivity at high magnetic field where the moments rotate. This suggests that the quantum fluctuations associated with the moment rotation may provide the pairing interaction for superconductivity. The objective of this thesis was to study these critical fluctuations with inelastic neutron scattering and heat capacity measurements, using the latter to test the bulk nature of the superconductivity and determine the types of gap nodes to help test this hypothesis.

To perform the heat capacity measurements, it was necessary to develop an apparatus that measures milligram samples in the temperature range 50-1000 mK, and magnetic field range 0-12 T. The field exerts a mechanical force upon the sample, which causes it to rotate, perturbing the system destructively. The apparatus developed in this thesis overcomes this difficulty by holding the sample with tensioned kevlar wires. Testing was done by making measurements on UPt_3, a well characterised superconductor. It was then used to measure URhGe in zero magnetic field. The extension to measurements in high magnetic field were not performed however, due to the structural integrity of the apparatus being weak - this was in an attempt to reduce the thermodynamic signature of the background. After many iterations of apparatus design and build, the device was proved not appropriate for high fields. A discussion of the zero-field data, as well as the design and build process, is given.

The Curie temperature of URhGe is suppressed with magnetic field (applied along the b-axis), reaching zero temperature at the moment rotation transition referred to above. Small angle neutron scattering (SANS) was measured at both zero and finite fields to detect the evolution and relaxation of the

critical fluctuations. The scattering is inelastic and the SANS measurement integrates over energy. Nevertheless it was possible to compare models with different dynamical dependences for the magnetic relaxation. In field, however, the magnitude of the fluctuations was strongly reduced, falling below the detection limit at half the critical field. Comparing Landau damping to various forms of non-Landau damping, a result was found that agrees with that for the ferromagnetic superconductors UGe_2 and UCoGe, but the lack of critical scattering at field is found to be in contradiction with NMR measurements, which is discussed.

UAu_2 is a new material on the heavy fermion landscape. The crystal structure found suggests some frustrated magnetism, culminating in a Neél temperature of 43 K and a further transition at 400 mK; this suggests some new quantum criticality not seen before, and so heat capacity measurements were performed with the already-tested apparatus to see if, as the resistivity measurements suggest, a Fermi-liquid state is found. Results revealed differences between annealed and non-annealed samples in their thermodynamic signature, and the behaviour expected for antiferromagnetic spin-fluctuations is found to continue to temperatures below 150 mK, suggesting the existence of a quantum critical point. The validity of these results along with implications are discussed.

Lay Summary

This work attempts to understand a particular set of materials, whose properties come under the banner of Unconventional Superconductors. The property of a material to display perfect electrical conduction, witnessed in lead, tin, mercury under certain conditions, defines superconductivity. What this thesis focusses on are a host of materials that additionally display a property these examples do not: magnetism. Uranium compounds show a range of magnetic behaviours that, when combined with superconductivity, display new properties that are relevant in quantum computing. However, the temperatures required in order to achieve these results are below 1 Kelvin (K), and so in order to study these, bespoke equipment is designed and tested in house.

How a material can be both superconducting and magnetic stems from how electrons are arranged. The signature of that arrangement shows itself in a particular property that is obervable: the heat capacity. This is a measure of the amount of order/disorder present within a system, stemming from whether the electrons are arranged or arranged randomly. Thus, by measuring the heat capacity, one can determine the electron arrangement, and infer if their alignment, either with any external magnetic fields or crystallographic axes, leads to unconventional superconductivity.

Two compounds are studied by these methods, being URhGe and UAu_2. The first, when cooled to below 0.275 K, is simultaneously superconducting and ferromagnetic; this means that all the spins of the electrons are aligned. Difficulties in keeping the temperature stable hinder attempts to measure the heat capacity with large magnetic fields applied. Otherwise, the results reinforce the fragility of single crystals of URhGe to maintain the hybrid state of superconductivity and magnetism, and the temperature dependence of the heat capacity in the superconducting state suggests the electrons do align.

UAu_2, on the other hand, is not a superconductor, despite it containing particular crystal properties that would suggest otherwise. The hexagonal arrangemnt of its atoms causes a frustrated type of magnetism to arise, while already displaying an ordered state of antiferromagnetism. This is somewhat antagonistic, and so the level of order/disorder is expected to change significantly at temperatures around 0.4 K. The heat capacity measured is of a low-quality crystal, resulting in data that contradicts with that of a higher quality crystal, down to temperatures of 0.1 K. The expectation of a transition from one type of magnetism to another was not met. A conclusion is that the higher disorder of the sample leads to a transition that is visible at temperatures below what is accessible here.

Finally, in order to understand how the superconductivity in URhGe is mediated, a measurement of neutron scattering is performed upon a sample. The neutrons scatter off large collections of electrons that, at the right temperatures, fluctuate in large densities. The amount a neutron is scattered, quantified in what angle the neutron's path is changed by, is indicative of the energy associated with the spin fluctuations. The results suggest the energy scale is much smaller than expected, meaning future attempts to measure this should take steps to access these lower scales.

This study helps understand the methods of measuring particular properties of small crystals, and reinforces the need for good quality crystal growth in order to better understand these novel materials. The links between superconductivity and magnetism are established more quantitatively, and a model for the electron dynamics that relies on both local and non-local properties is reinforced as representative of uranium compounds' magnetism.

Declaration

I declare that this thesis was composed by myself, that the work contained herein is my own except where explicitly stated otherwise in the text, and that this work has not been submitted for any other degree or professional qualification except as specified.

(*Oliver John Entwisle, April 2018*)

Acknowledgements

I would like to thank my supervisor, Andrew Huxley, for patiently helping me in both the lab when the inevitable problems appeared, and in multiple discussions on the many complications of this field. In addition, Jean-Phillipe Reid, Michal Kepa, Julian Schmehr, and Matthew Neat were great companions on this journey. The master craftsmen who helped bring to life a lot of the equipment used were essential in this respect, being Andrew Downie, Mike Fisher, Toby Fu, Derek Low, and Ronnie Proc.

My office pals who kept me sane and laughed at my stupid jokes must be mentioned, being Martin Gorman, Natasha Nicholson, Alex Slowman, Martina Foglino, Tom Ives, Duncan McCann, Charlotte deGrouchy, Jennifer Wadsworth, Giulio deMagistris, and Eddie Pace.

My various bands AISIAEC, No Swan No Funk / The Operators, Spaceboots, East West Rendevouz, Summerhall Choir and Tinderbox Orchestra are all responsible for allowing me to be musically creative throughout my PhD, for which I am extremely thankful.

Last but not least, I will ever be grateful to Isobel for supporting me with love and brownies, as I will be to Mum, Dad, Eve, George, Nick, and Steffen.

Contents

List of Figures

List of Tables

Chapter 1

Introduction

In modern day condensed matter physics, a researcher is ideally attempting to simplify the huge number of interactions and events happening to and amongst huge numbers of the constituents that govern electricity and magnetism: electrons. The description of electron motion has gone through many stages of understanding, from a primitive ballistic approach to including the seemingly unintuitive rules of quantum mechanics. In this work, an attempt is made to bridge two worlds of thought, where a quantum phenomena is observable from a thermodynamic point of view, connecting research that spans many decades.

With time, it has been discovered that the number of electrons present in any material is beyond the value that any single person can reasonably manage, in terms of performing calculations. If each individual electron can interact with every other, and those interactions can differ in nature (be it Coulomb, gravitationally, through spin, or otherwise), then the number of governing equations can match that number, and even the most advanced computational equipment fail to reduce computation times to within human lifetimes. Thus, a sensible amount of approximation is applied, allowing the knowledge of complex ideas like the band structure of crystalline solids to be determined, and the fruits of these labours are in the results, which can be surprisingly accurate when compared to nature.

The Coulomb interaction, named for the electrostatic repulsion/attraction between like/oppositely charged bodies, generally governs the motion of all electrons, but the nature of this interaction leads to non-analytic Hamiltonians.

Thus, if one were to simplify the system by removing interactions, what's left is called the Fermi gas, a collection of non-interacting electrons (or fermions) that obey a particular set of quantum mechanical rules, the Fermi-Dirac distribution. This relatively simple construct turns out to be invaluable for describing a large number of systems, including many of the uranium compounds investigated in this work. However, the sensitivity of this phase of matter to parameters like temperature and magnetic field leads to the possibility of a single material transitioning in and out of this phase at unexpected points of the phase-space. The third law of thermodynamics tells us that as temperature reduces to 0 K, so too must entropy follow suit, and so an ordered phase usually comes at a temperature lower than a non-ordered phase; for example, the transition from paramagnetism to ferromagnetism as the temperature is cooled below 9.5 K in URhGe. Additionally, transitions at such low extremes of temperature, far below 10 K, can suggest the presence of quantum criticality.

Quantum criticality, the name given to the type of physics that occurs about a zero-temperature phase transition [3], opens up another world of scientific interest. In the vicinity of phase transitions at relatively high temperatures (i.e. more than 1-5 K), the physics and general thermodynamic properties are governed by classical thermal fluctuations, those which bring about phenomena such as Critical Opalescence, where boiling water briefly appears completely black due to large, slow fluctuations in the density [4]. However, in the vicinity of a quantum critical point - the point in the phase diagram at which the transition occurs at 0 K- quantum fluctuations govern the physics. What one must realise is that a T=0 K transition implies there are actually two competing phases, or phrased another way, two degenerate ground states. This delicate balance can lead to singularities in quantities like the heat capacity, being a differential of the free energy, and thus a tangible window exists in the potential to detect quantum phenomena through thermodynamic variables (for example, in UAu_2 as a bulk transition is measured at 420 mK [5]).

A method of experimentally accessing this quantum phenomena is through the process of the suppression of a second-order transition temperature. This entails, usually, the reduction of, say, a magnetic transition temperature, through the application of magnetic field [6], pressure [3], or even chemical doping [7].

In this thesis, a quantum critical point is investigated in the superconducting

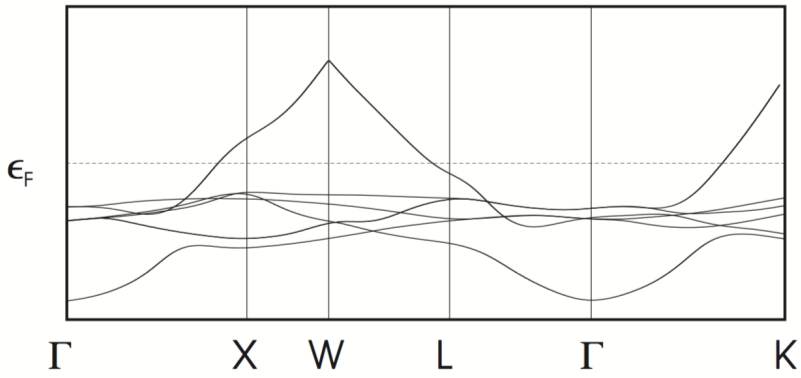

Figure 1.1 *The band structure of Cu, close to the Fermi energy ϵ_F, is shown along lines connecting points of high symmetry in the Brillouin zone [9].*

ferromagnet, URhGe. By applying a magnetic field along a particular axis, although the magnetic transition temperature is suppressed, a superconducting phase that is initially destroyed is activated again, for a limited region of field. The simultaneous existence of these antagonistic phases leads one towards unconventional theories of how they might be mediated, with the current main contender being fluctuations in the spins allowing a binding process between certain quasiparticles [8].

The possibility for a mixture of such correlating features stems from the fact URhGe has narrow bandwidths, as do many f-electron heavy fermion materials [2]. An example of bandwidths is shown in Figure 1.1 for Cu, taken from [9]. Correlation effects are usually possible due to the corresponding large density of states, and thus the energy scale involved in accessing all parts of the phase diagram is realistic with the laboratory magnetic field. Additionally, the energy scale associated with the fluctuations encountered during the magnetic transition can be indicative of electron dynamics, and thus to accompany studies of electron alignment about the Fermi surface, neutron scattering allows a window upon these energies [10], clarifying any links between magnetism and superconductivity.

These experimental endeavours are all unique in that performing them in such conditions has not been attempted in the known literature. Thus, no direct measurement of the evolution of the entropy of URhGe during the high-field transition to superconductivity exists. This gap in the knowledge of the system halts progress with respect to knowing the full degrees of freedom of this interesting material. Thus, the measurements here have several purposes.

First, the phase diagram is attempted to be investigated, using specific heat measurements to elucidate the thermodynamic nature of the transitions as well as determining the phase boundaries themselves. Second, the neutron scattering upon URhGe at extremely small angles will arrive at a quantitative result concerning the energy scale of the electrons that are subject to the fluctuations.

In addition to this, another uranium compound is investigated, UAu_2. Being a little-studied, antiferromagnetic, hexagonal-structured material, this too presents quantum criticality at temperatures below 2 K [5]. It is thought that due to apparent ordering at temperatures around 400 mK, the ability for a material to transition once already within a magnetic phase is suggestive of a new physics; the quantum critical behaviour is within the ordered state, rather than at the point order is suppressed. The measurements here hope to clarify what the phases are down to low temperatures, potentially capturing a second transition that is expected from such crystal geometries and constituents.

This thesis will cover the following different aspects of the project in subsequent chapters: background physics and literature in chapter 1. The theory of heat capacity measurements and how they stem from modelling heat flow is covered in chapter 2, then the equipment and methods used for low-temperature thermometry are reported in chapter 3. Chapters 4, 5, and 6 concern the results for the experiments performed, and then conclusions and appendices, ending with the bibliography. Chapter 6, describing the neutron scattering experiment performed, also includes the theory and literature in the first half.

1.1 Entropy and Heat Capacity

The study presented here looks at phase transitions at extremely low temperatures. The lowering of temperature of a system has consequences, as described by the laws of thermodynamics. The third law concerns what happens when a system approaches $T = 0$, and one consequence is that temperature derivatives of most thermodynamic quantities collapse to zero with T [11]. Thus, when the opposite is seen, for example in URhGe at 275 mK when the material goes superconducting [1], or when a system like UAu_2 transitions into what one would call frustrated magnetism [5], one must understand how the third law is maintained. The subject of phase transitions is covered in many textbooks [4, 12]. Only the aspects that

are relevant to the measurements reported in this thesis will be discussed briefly.

The second law of thermodynamics states that, for a closed reversible thermodynamic path,

$$\oint \frac{dQ}{T} = 0 \tag{1.1}$$

This states that a system transfers no energy with the outside, and the transfer of energy along a particular path can be undone. Expressed here is a property of a thermodynamic state, and so if we define entropy S to be a function of that state, then its differential is given by $dS = dQ/T$. Thus, if we assume that the variables of a system are temperature and magnetic field, then the total differential of entropy, given these as its only dependencies, is

$$dS = \left.\frac{\partial S}{\partial T}\right|_H dT + \left.\frac{\partial S}{\partial H}\right|_T dH \tag{1.2}$$

This equation describes how the entropy changes with temperature and field, and thus we can define two quantities that are measurable. The heat capacity at constant magnetic field, $C_H = \left.\frac{\partial S}{\partial T}\right|_H \times T$, and the magnetocaloric coefficient, $\Gamma = \left.\frac{\partial S}{\partial H}\right|_T \times T$.

Exactly what these measurable quantities probe requires more introduction of concepts. One of these is a Fermi liquid [13]. This is a phase of matter in which adiabatically increasing the magnitude of interaction energy between individual particles results in quasiparticles that mimic the characteristics of non-interacting individual particles. This leads to certain power laws of thermodynamic and transport variables, characterising the phase.

How we get to those power laws requires first formalising the observables, like the heat capacity. This is possible by formalising the internal energy of a system of N particles in terms of wave functions, and then differentiating. From the Schrödinger equation, one can arrive at the result for fermionic particles via a method that Slater first conceived [14]; by placing the wave functions of each fermion into a matrix, then calculating the determinant of that matrix produces eigen vectors with all the minus signs necessary for the antisymmetric exchange symmetry between fermions. After calculating the energy bands $\epsilon_N(k)$, dependent on the index of the band N, and the momentum vector k, and understanding how they fill up the Brillouin zone, then one can arrive at an image of the distribution

of possible states these fermions can fill, defining the Fermi surface. Simple geometries result in spherical Fermi surfaces, where the magnitudes of all possible k_F are equal [9]. However, materials like UPt_3 have Fermi surfaces as shown in Figure 1.3. Here, the size of k_F varies, depending on the direction. Now, knowing the bands results in knowing the energies of each individual electron, and this allows one to define the total energy of the system as the sum of all the individual energies:

$$E = \sum_{\underline{k},\sigma} \epsilon_{\underline{k},\sigma} \langle n_{\underline{k},\sigma} \rangle \tag{1.3}$$

$$= 2 \sum_{\underline{k}} \epsilon_{\underline{k}} \langle n_{\underline{k}} \rangle \tag{1.4}$$

where for a non-interacting system, the spins don't matter, resulting in the 2 and the dropped σ index. This simple expression for the total energy can be evaluated in three dimensions, recognising that the summation can become an integral in the limit of large volumes. This results in the following [9]:

$$E = E_0 + \frac{\pi^2}{6} n(\epsilon_F) \left(k_B T\right)^2 \tag{1.5}$$

$$\therefore C_{el} = \frac{\partial E}{\partial T} = \frac{\pi^2}{3} k_B^2 n(\epsilon_F) T \tag{1.6}$$

where T is temperature, k_B is the Boltzmann constant, and $n(\epsilon_F)$ is the density of states at the Fermi energy. C_{el} represents the electronic specific heat for temperatures less than 10 K, corresponding to about 1 meV (this assumption is applied in a step termed a Sommerfeld expansion, resulting in equation 1.5). The prefactors to T can be collected into the single term γ, termed the Sommerfeld coefficient, and it is this that defines whether a particular system is heavy-fermion or not, due to its implicit (via $n(\epsilon_F)$) dependence on electron mass. What can happen is that this term can be proportional to tens and even hundreds of electron masses, representing the mass of the quasiparticles that the system renormalises itself into during the transition into a Fermi liquid.

From another perspective, it is possible to gain a more pictorial version of the temperature dependence of energy, especially the link between that and Fermi surface geometry. An excitation can be thought of as a charge carrier, occupying some energy just below ϵ_F, boosted upwards to a new energy above ϵ_F, leaving

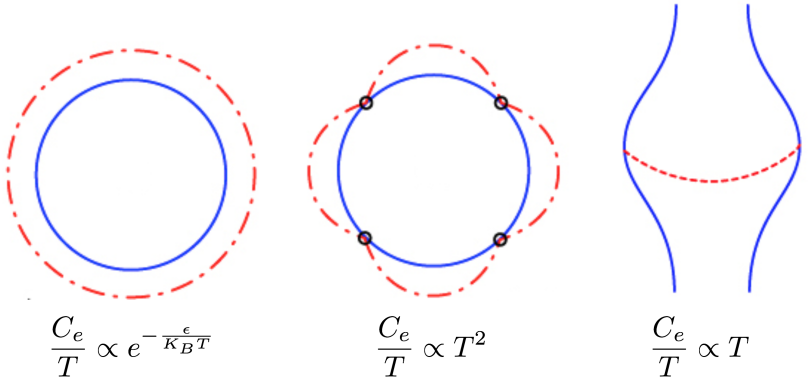

Figure 1.2 *Three possible node structures for the given temperature dependences of the heat capacity. The blue lines represent the lowest possible state, or the state of the superconducting condensate. The red lines represent the energy gap separating the condensate from the rest of the conduction electrons; how these two can come together is given in the text.*

behind a hole of opposite charge[1]. For a spherical Fermi surface, with states distributed evenly, the dependence of the energy on temperature being quadratic is easily seen: the number of states in a thin spherical shell about the surface is proportional to temperature, and the change in energy for a (temperature-limited) small excitation to just above the Fermi surface is equal to $k_B T$, and so the combination gives T^2. Superconductivity will be introduced fully in the next section, but briefly, for superconducting materials the resulting $E(T)$ can be wildly different, and some examples are shown in Figure 1.2. Here we see a Fermi surface that is fully-gapped, has point nodes, and line nodes, from left to right. What is meant by the gap is as follows: when fermions couple to form an effective boson, they overcome the Pauli exclusion principle and occupy the lowest energy state available, represented in Figure 1.2 by the blue lines. The gap then corresponds to the energy needed to excite a boson out of said state. Thus, the first example is an isotropic superconductor, and the corresponding heat capacity follows an exponential T-dependence. If, however, the gap closes at certain points, as shown in the middle-and-right examples, then for particular values of momentum k, electrons will be able to be excited above ϵ_F with little energy required. This results in the possibility of a finite thermal conductivity, which would otherwise be zero for a fully-gapped superconductor. Viewed from above the point node, the resulting chasm in the energy plane leads to[2] a temperature

[1] In the case of anisotropic superconductors, this excitation can take the form of a Bogoliubov quasiparticle [15]

[2] How to arrive at these temperature dependences pictorially is as follows: $E = \text{volume}_\epsilon \times \epsilon = (\text{vol}_{cone} \times K_B T)$ or $(\text{vol}_{valley} \times K_B T)$, for point and line nodes respectively. The cone is the

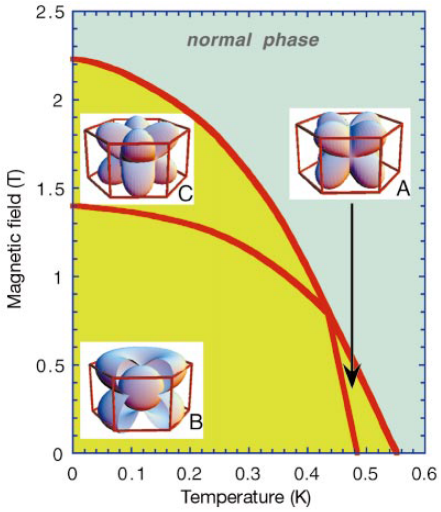

Figure 1.3 *The phase diagram of UPt_3 at low temperature and magnetic field parallel to the hexagonal crystal axis, with critical values found from [18]. The Fermi surfaces shown are from calculations [19], experimentally verifiable from Fermi-surface-probing measurements.*

dependence of $E \propto T^4$, and furthermore if those point nodes form a line across the Fermi surface, then this leads to $E \propto T^3$. Thus, it is possible to determine how the Fermi surface is gapped by measuring the temperature dependence of the heat capacity. An example of this technique is in measurements of Sr_2RuO_4 in both heat capacity and thermal conductivity. What is measured is that below the superconducting temperature, T_c, the heat capacity divided by temperature is proportional to temperature linearly; $C/T \propto T$. Additionally, a small jump $\Delta C/\gamma_N T_c$ is observed. This can be explained by gap-anisotropy via short-range anisotropic ferromagnetic spin fluctuations, and that anisotropy comes in the form of nodes that are measured as vertical line nodes from thermal conductivity (vertical meaning perpendicular to the basal plane) [16, 17].

A similar approach was executed for UPt_3, resulting in a complex phase diagram featuring nodes changing with temperature and field, as shown in Figure 1.3; above 480 mK, the theoretical model used [19] results in a pair of line nodes crossing at right angles, producing bulges of Fermi surface in the corners. Below 480 mK, the vertical line node splits into two point nodes, becoming points of high symmetry. This symmetry can be captured in a single quantity which defines whether the system is in a particular phase or not, called the Order Parameter. Being a quantity that only takes a value when inside the critical phase, this could be the magnetisation for a material transitioning from paramagnetism to ferromagnetism (as it is for URhGe). For an unconventional superconductor

energy-volume a fermion can be excited into from a point node, and the valley the same for a line node. The volume of the cone is related to the area squared $\propto (k_B T)^2$, whereas the valley will be $2\pi\times$ the length of the valley, which is limited to $k_B T$.

like UPt_3, the order parameter is the gap parameter Δ [20]. This has some spatial dependence defined by the Fermi surface, and so for the nodes shown, that parameter can take the form $\Delta \approx \tilde{k_z}(\tilde{k_x} + i\tilde{k_y})^2$ [8]. More will be said about this in the next few sections.

1.2 Superconductivity

1.2.1 Conventional Superconductivity

The combined phenomena of electrons carrying a current without any resistance, and perfect diamagnetism, requires a particular set of conditions which can depend on a variety of material properties. The first few superconductors discovered, being mercury [21], tin, and lead [22], were found to correspond to BCS theory [23]. This describes a process of crystal lattice vibrations that give rise to electron coupling. Written down in 1957, it takes the ideas of the London brothers, namely the penetration depth of magnetic fields into superconductors [24], and explains them microscopically.

The order parameter for all superconductivity, as briefly mentioned in the previous section, is the gap parameter Δ_k. The formulation of Δ_k originates from BCS theory. The effects upon the order parameter are the following: first, there is full inversion symmetry of both Δ_k and ϵ_k, and second, any point group symmetry operation upon Δ_k has no effect upon it [25]. This is summarised as:

$$\Delta_{\hat{R}k} = \Delta_k \tag{1.7}$$

$$\Delta_{-k} = \Delta_k \tag{1.8}$$

$$\epsilon_{-k} = \epsilon_k \tag{1.9}$$

This suggests some isotropic pairing across momentum space, defining Cooper pairs: a pair of electrons of opposite spin coupling together over large distances relative to the lattice parameters. They can exist at opposite points on the Fermi surface, and the non-specificity of the location means any pair of points are equivalent, reinforcing the spherical image. It is on these principles that materials including CuO, Yb, Ce, and U differ, requiring an alternative theory of superconductivity [3].

1.2.2 Unconventional Superconductivity

First, one simple observation that denies BCS theory as a candidate for certain materials is their ability to be both superconducting and magnetic. Especially for ferromagnetism, the alignment of spins contradicts the necessity for opposite-spin-pairing. Thus, including equal-spin-pairing (ESP) in any theory written down is essential, as was done by Fay & Appel in the 1980s [26]. They proposed a pairing interaction that draws similarities with the A1 phase of superfluid ^{3}He[3].

Examples of systems that display unconventional superconductivity include cuprates and heavy-fermion materials. The former appeared when searching for materials with a high superconducting temperature, which can stem from BCS-type electron-phonon interactions [27] amongst the Perovskite-type structure. However, through the tuning of chemical doping and pressure/strain, the same suppression of critical phenomena is observed in uranium compounds [28], suggesting its deviation from any Fermi liquid behaviour suggested.

At temperatures above that for superconductivity, for a transition into a magnetic state, the magnetisation defines the order parameter. Like a regular magnetic transition, there will be a fluctuation of the order parameter in the vicinity of the transition. For an anisotropic superconductor, that order parameter can potentially be key for the activation of superconductivity, due to the idea that fluctuations mediate some coupling. Fay & Appel claim [26] that only longitudinal fluctuations, that is along the easy magnetic axis, contribute to the coupling necessary for superconductivity.

Although not pursued experimentally in this work, it is worth mentioning a key corollary of unconventional superconductivity. This is the concept of the enclosure of a half flux quantum [29]. What this entails can be clarified by discussing the equivalent case in conventional superconductivity. The materials that come under that classification either fall into one of two categories, type I and II superconductors. They differ on whether the application of magnetic field causes a first-order or second-order transition back into the normal state. For type II, a mixed-state can exist for fields below the critical value H_{c2}, where vortices

[3]This phase exists only at some finite magnetic field; the spin & orbital angular momentum is held by rotational symmetry. If the system is fermionic, then the fermions can be represented by $|\psi\rangle = a|\uparrow\uparrow\rangle + b|\downarrow\downarrow\rangle = a|\uparrow\uparrow\rangle$, aligning with the external field. The spin-splitting of the Fermi surface leads to one of the amplitudes being preferential (b=0).

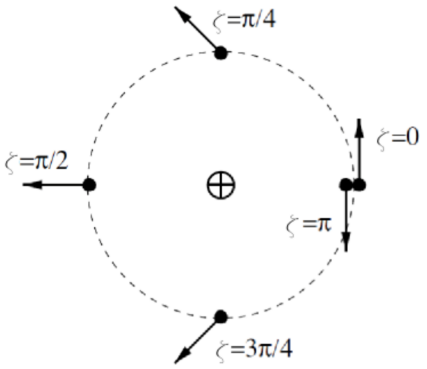

Figure 1.4 *For a p-wave superconductor, a half-quantum vortex is enclosed due to the order-parameter (arrows) changing by* $(\zeta \to \zeta + \pi, \overrightarrow{\eta} \to -\overrightarrow{\eta})$

of normal state penetrate the superconducting condensate. A phenomenon that arises is a supercurrent j that surrounds the vortices, which can be expressed in terms of the superfluid density n_s, electron charge and mass e & m_e, the phase of the superconducting order parameter ζ, and the flux quantum ϕ_0 [25]. If one integrates the curl of j around the vortex, then the supercurrent simply picks up a factor of $2\pi r$:

$$2\pi r j = -\frac{n_s e^2}{m_e}\phi_0 \left(\Delta\zeta + 2\pi\frac{\phi}{\phi_0}\right) \tag{1.10}$$

At large distances from the vortex, the supercurrent decays to zero, leaving the right hand side of equation 1.10 equal to zero.

$$\therefore \frac{|\Delta\zeta|}{2\pi} = \frac{\phi}{\phi_0} \tag{1.11}$$

What this equation says is that the only parameter that can be changed in order to maintain the single-valued nature of an electron wave function as it circumnavigates a vortex is the phase, ζ. Thus, this one-dimensional nature of the description of superconductivity is deemed representative of the conventional brand. For unconventional superconductivity, however, the order parameter $\overrightarrow{\eta}$ contains two variables, ζ and θ.

$$\overrightarrow{\eta} = \Delta \begin{pmatrix} \cos(\theta) \\ \sin(\theta) \end{pmatrix} e^{i\zeta} \tag{1.12}$$

where θ is an angle that defines the direction of this vector. This allows some degree of freedom for the electron's angular momentum, as expected for a p-wave electron-coupling symmetry type. This means that in order to maintain the single-valued nature for the wave function, both ζ and θ can be changed simultaneously. This is shown in Figure 1.4, where the circle represents a full

vortex, but ζ and θ have both only been shifted by π rather than 2π. One crucial corollary from this is that the excitation spectrum of these vortex states include the possibility for Majorana fermions to exist, being a proposed particle that can help realise a quantum computer [30]. Their discovery has not yet come to pass, but candidate materials like UAu_2 contain the anisotropy that could permit the right sort of order parameter required [5]. This would allow the penetration length λ to be longer than the radius over which the supercurrent decays, or in other words, the Meissner effect fails to screen charge currents that is otherwise possible in other geometries [31].

A key property of unconventional superconductors is related to the Fermi surface. The superconducting gap can close to zero, whereas for conventional superconductors the gap remains finite along all momentum vectors. Now, if scattering is possible, especially off magnetic impurities, then any states that obey time-reversal symmetry are now susceptible to being destroyed. The scattering of an excitation from a positive to a negative part of the Fermi surface is only possible from magnetic impurities, and thus the states responsible for superconductivity are especially vulnerable to these impurities. This proposes a challenge to sample growth, requiring low impurity concentrations in order to witness the critical phenomena.

1.2.3 Phonons, Magnons, and UGe_2

It is useful to narrow down the constituents that contribute to the heat capacity. The quanta of a crystal lattice, phonons, have been shown by Debye [32] to display a cubic temperature dependence in the heat capacity, generally applicable at temperatures above 5 K. Magnons on the other hand, being quanta of magnetic correlations, are known to be present when the heat capacity follows $T^{3/2}$ [33] for ferromagnetism, and T^3 [34] for antiferromagnetism.

In order to understand the origin of a change in entropy, the different contributions must be separated. At higher temperatures, this would be done via the Debye model, but at the temperatures relevant in this thesis, Debye's contribution is negligible. Compounds that display magnetic transitions at temperatures in the region of 5-100 K do have some justification to be dissected into the phononic and other contributions, where one example is UGe_2. This was the first compound to display both ferromagnetism and superconductivity in the same region of phase

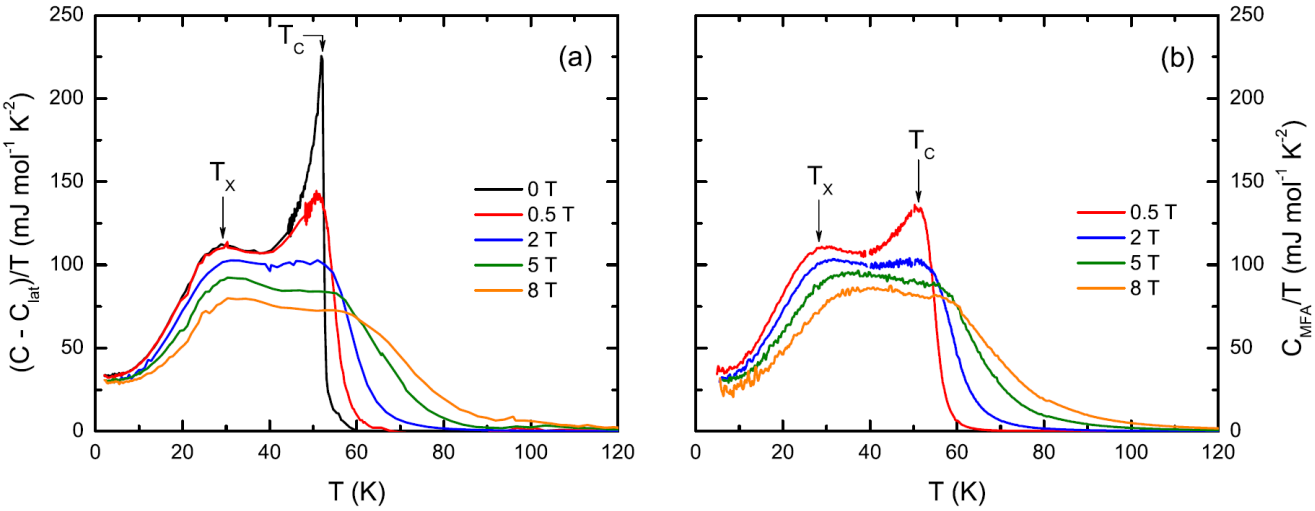

Figure 1.5 *Left: heat capacity of UGe_2 minus the lattice contribution, at various field values. Right: calculation of the magnetic heat capacity from measured magnetisation, using MFA. The similarities of the two prove the relevance of MFA [35].*

diagram [35], albeit with $T_{Curie} \sim 55$ K and at pressures of ∼10 kbar. In order to separate out the electronic and magnetic contributions, what was recognised was that in certain conditions, the magnetisation $M(T)$ can lead back to the pure magnetic heat capacity $C_M(T)$. Those certain conditions are akin to UGe_2, but not other itinerant ferromagnets like Co and Fe. This is due to the excitation spectrum being dominated by longitudinal fluctuations of the magnetisation, usually stemming from a strongly anisotropic magnetisation. These fluctuations can be re-interpreted as a positive exchange-interaction via some molecular field with a coupling constant λ_M, defining the relevant molecular field approach (MFA). Any external magnetic fields will add to this interaction field, causing possible Zeeman splitting. This model can be applied to both itinerant and localised moments, described by either the Stoner or Weiss model, respectively. The heat capacity predicted [35] is of the form

$$C_{MFA}(T) = -\mu_0 V_m \frac{\lambda_M}{2} \frac{\partial M^2}{\partial T} - \mu_0 V_m H \frac{\partial M}{\partial T} \tag{1.13}$$

where μ_0 is the magnetic permeability, and V_m is the molar volume. The first term corresponds to the molecular field heat capacity, and the second the Zeeman heat capacity. One can simply take the magnetisation data $M(T)$ and run it through this equation to find the heat capacity; for UGe_2 the results are positive in that the MFA is highly relevant as a basis for explaining the behaviour at the conditions stated. This is shown in Figure 1.5.

1.2.4 Heat Capacity of Superconductors

To determine what the heat capacity data suggests in terms of electron dynamics, one must know the theory behind it. Tinkham gives a good derivation [20] of what BCS theory predicts for the heat capacity, broken down into two contributions.

$$C = \beta k \sum_k -\frac{\partial f_k}{\partial E_k}\left(E_k^2(T) + \frac{\beta}{2}\frac{d\Delta^2(T)}{d\beta}\right) \tag{1.14}$$

where $\beta = 1/K_B T$, f_k is the Fermi-Dirac function, and E_K is the energy of the state k. The first term, E_k^2, is related to how the quasiparticles re-distribute themselves with temperature, settling into new energy states. Near the transition, this reduces to a linear temperature dependence, as is the case for normal-state heat capacity. This dependence is constant throughout the transition, defining a lower bound.

The second contribution is from a subtler origin: as the gap's magnitude changes, so too do the energy levels available, and thus the spacing between those levels changing leads to a new entropy state. As the gap function reflects the order parameter, then the discontinuous change in gradient at T_c leads to the same in heat capacity. The first term being continuous and the second not being so leads to a prediction that is possible to verify in experiments: the size of the jump in heat capacity at T_c should be of the order of 1.43 times the heat capacity above T_c; an easy check for if BCS is relevant.

Now a little more on $\Delta(T)$. For conventional superconductors, this gap function is generally close to symmetric in momentum states, and so there's no preferable direction in which some excitation occurs to remove some electrons from the condensate. For URhGe, UPt_3, and a variety of other heavy fermion compounds, the story is quite different. Their gap function can take on geometries that close the gap, creating channels for excitation and thermal conduction - UPt_3's thermal conductivity reflects the large Sommerfeld coefficient, where a residual value at $T = 0$ K from a power law rather than an exponential dependence is observed as temperature drops below T_c [36].

As stated before, the temperature-dependence of the heat capacity can infer what the geometry of the Fermi surface is. One can derive this temperature-dependence from knowing the density of states of the system, and this can in

turn be calculated from the order parameter. The types of order parameters that exist for triplet-spin superconductors tend to be vectors, rather than scalars. As shown in [29], the density of states calculated for two different types of pairing in p-wave superconductors[4] can be simplified in the limit of low energies.

$$\rho(\omega) = \begin{cases} \frac{N(0)\Delta_0}{2\omega}\left(\frac{\omega}{\Delta_0}+\frac{1}{2}\left(\left(\frac{\omega}{\Delta_0}\right)^2-1\right)\ln(\frac{\omega+|\Delta_0|}{|\omega-|\Delta_0||})\right)\to\omega^2, & \text{A state} \\ N(0)\frac{\omega}{\Delta_0}\begin{cases}\times\frac{\pi}{2}, & \omega<\Delta_0 \\ \times\sin^{-1}(\frac{\Delta_0}{\omega}), & \omega>\Delta_0\end{cases}\to\omega, & \text{B state}\end{cases} \tag{1.15}$$

$$\therefore C = \frac{2}{T}\int_0^\infty dE\rho(E)E^2\left(-\frac{df}{dE}\right) = \begin{cases}\frac{8}{T}\int_0^\infty f(E)E^3dE\to T^3, & \text{A state} \\ \frac{6}{T}\int_0^\infty f(E)E^2dE\to T^2, & \text{B state}\end{cases} \tag{1.16}$$

Here is given an alternative approach to deriving the temperature dependence of the heat capacity to that given in section 1.1. The distinction between the states A and B leads to a difference in the Fermi surface gap-closings, or more familiarly known as nodes. For the A-state, the nodes are points, where the gap collapses around it. For the B-state, the nodes are lines; an example is shown in Figure 1.3 for UPt_3.

[4] p-wave corresponds to triplet spin symmetry, referencing the naming of angular momentum states: $l = 0(s), 1(p), 2(d)$....

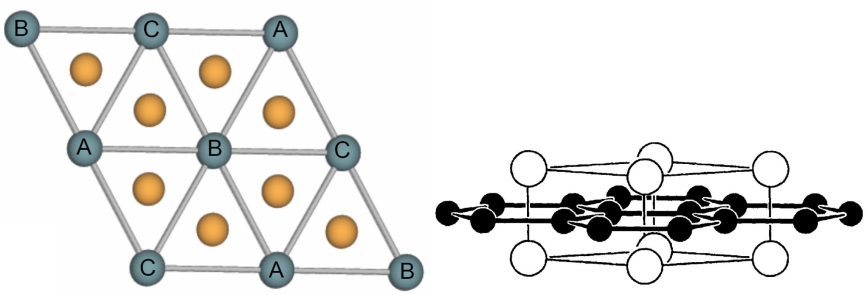

(a) (b)

Figure 1.6 *(a) The view normal to the planes within the structure of UAu_2; gold represents gold ions, and grey-blue uranium ions. (b) The side-on view of the same structure,displaying how close the planes are relative to the spacing between U in-plane.*

1.3 Uranium compounds

1.3.1 UAu_2

This material was initially chosen as a candidate for unconventional superconductivity, with Cooper pairs formed of spins that combine to give non-zero angular momentum. Even though no evidence to date supports this, the presence of an inversion centre, hexagonal structure and magnetic frustration all imply quantum-driven transitions are expected at sufficiently low temperatures, albeit not a superconducting one.

Crystal Structure

UAu_2 crystallises in the AlB_2-type structure, where the U atoms form a triangular lattice, and the Au atoms fit inside the triangles forming a hexagonal lattice, although the two structures are off-set in the axis perpendicular to the planes; this is shown in Figure 1.6.

The interatomic distances between the U atoms in the plane is greater than that between the planes, or put another way, the intra-plane atomic distance is greater than the inter-plane atomic distance. This leads to complex interactions, where if one were to apply a tight-binding model with electron hopping, then not only nearest neighbour but next-nearest neighbour interactions must be taken into consideration. This property is recognised in high-temperature superconductivity,

as Anderson stated in his work on La_2CuO_6, where magnetic frustration and antiferromagnetic exchange can result in a quantum-spin-liquid state [37].

There is more to this structure, when one considers what happens across the inter-plane axis, labelled the c-axis. When looking along the c-axis, the U atoms form triangles normal to that axis, and long chains along the axis, resulting in triangular prisms throughout the structure; this is shown in Figure 1.7. This allows one to easily consider modulations in the magnetic order along the c-axis, and especially so since incommensurate magnetism is found in UAu_2. The evidence for the incommensurability comes from the μSR data [38]; if the modulation vector is quantified as δ, then as there is some temperature dependence of δ, then there is thus some temperature dependence of the magnetic unit cell. If the magnetism was (a) ferromagnetic in nature, or (b) commensurate, then the size of the magnetic unit cell would be finite, taking up some number of layers of the hexagonal and triangular layers of atoms. Here, in the incommensurate phase, the unit cell is infinite along c, and its extent in the plane requires further explanation. First, a comparison with other materials.

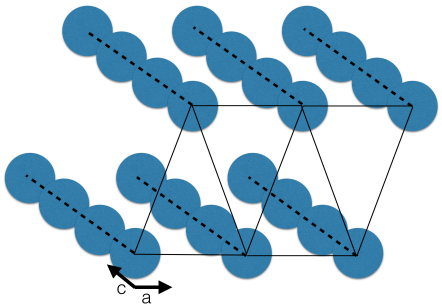

Figure 1.7 *With the gold atoms removed, shown are the long chains of U-atoms, in blue, forming along the c-axis.*

In Ca_3CoRhO_6, displaying a similar crystal structure, the dominant interaction is along the chains, fixing the moments to align into a ferromagnetic state within each chain [39]. Domain walls thus arise between the chains, impeding the transition to a fully ordered state at lower temperature. Alternatively, antiferromagnetic order can develop along the chains in $CsCoCl_3$ and $CsCoBr_3$, in which a transition to a fully ordered state does take place, manifesting as two spins up/down, one spin down/up ($\uparrow\uparrow\downarrow$ / $\downarrow\uparrow\uparrow$) [40, 41]. Additionally, some modulated magnetism manifests itself as spins modulating along the chains, resulting in a wave vector that can be measured with neutron scattering. This is the case for $CsCuCl_3$, but one key difference is that this system achieves this modulation through a spiral crystal structure, which approximates to a triangular structure [42]. UAu_2 shares the property of modulation of the magnetic unit cell, but without the spiral structure.

In fact, UAu_2 is different from all these examples, because they are all insulators. What is common between them is the change in local magnetic moment relative to some axis on changing some control parameter. The metallic behaviour of UAu_2 still provides some evidence of critical behaviour, however. The Neél temperature is defined from kinks in the resistivity along both the a- and c-axis, as shown in Figure 1.8b[5] - all experimental work as shown in these figures and referenced in the next few paragraphs on UAu_2 stems from yet-to-be-published work by J. Schmehr [5]. A transition into AFM is visible in the resistivity. This is inferred from a rise in resistivity along the c-axis - the crystal unit cell doubles in size for an AFM system, and the Fermi surface folds to accomodate this change, reducing the surface area available for conducting states. There is also a lack of hysteresis in the magnetisation data, which rules out FM. Also, like any second order phase transition, the presence of fluctuations (in this case, of the magnetic moment) is accentuated by their increase in both duration and amplitude. Thus, an increase of scattering of modes off these fluctuations can also lead to an increase in electrical resistivity. The anisotropy of the resistivity behaviour through the transition also suggests the fluctuations are fixed along the c axis.

Critical Behaviour below T_N

There are further transitions below T_{Ne}, at zero field, which add complexity to the situation. From around 20 K, the slope of $\rho(T)$ with T increases, indicating a change in the scattering behaviour. Additionally, moment fluctuations detected by μSR start to slow down, and a strengthening of the amplitude of a charge density wave (CDW) detected occurs. These observations are also found in non-ordered heavy fermion metals, and are explained as such originating from a Kondo-type overlap with magnetic order. To find a Kondo transition within a AFM phase is unique enough to warrant study, but add to that the non-Fermi liquid behaviour inferred from heat capacity studies done both in this thesis and beforehand, and one has quantum-critical behaviour within an already-ordered state.

For either annealed or non-annealed samples, when a magnetic field is applied

[5]To be both AFM and incommensurate is reasonable; treating each triangle of U atoms as a single spin, collectively those spins will add up to be anti-symmetric, but the spins rotating along the c-axis can still be over an irrational multiple spins, relative to the crystal dimensions.

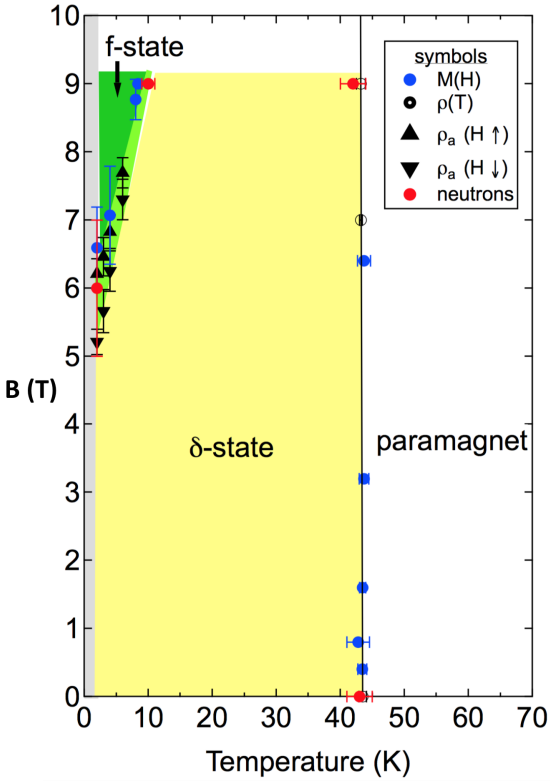

(a)

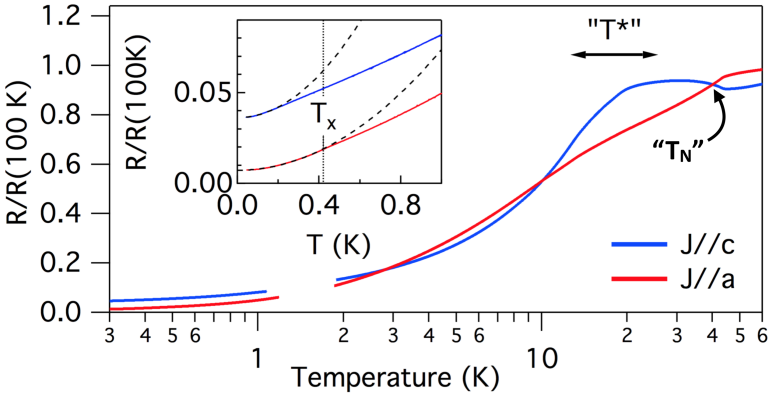

(b)

Figure 1.8 *The temperature-field magnetic phase diagram of UAu_2 determined by magnetisation, resistivity, and neutron scattering [5]. The ordered state (δ-state) that occupies most of the figure is incommensurately modulated along the c-direction. Sensitivity to external field is not shown in T_N, whereas it is shown in the transition to ferrimagnetism, from 6 T upwards. In (b) the resistivity is normalised to the value at 100 K; the ratio of current along the c ($J||c$) and a-axes ($J||a$) is close to 2 over this temperature range. The inset shows the low temperature behaviour. The dashed lines are Fermi-liquid T^2 dependences. At 0.42 K there is a change of slope for $J||a$ and a weaker change in $d^2\rho/dT^2$ for $J//c$. The transitions at T_N and T_x are marked and the cross-over in the region of T^*.*

along the c-axis, a transition occurs at around 6 T, resulting in the ordered ferrimagnetic ($\uparrow\uparrow\downarrow$) state. One could think of the field enforcing this order upon the spins, but whether this transition is possible without magnetic field could be linked to the annealing of the sample - this is discussed in Chapter 4. The presence of this magnetic order was studied by neutron scattering measurements, performed on a range of samples, namely powder and single crystals. As temperature and field were varied, the transition from the incommensurate AFM phase to the ferrimagnetic phase was not absolute, in that not the entire sample transitioned. For the powder sample, 28% of the sample was found to transition, whereas for the single crystals, a maximum of 3% changed into ferrimagnetism. This is thought to be linked to the strained regions of the sample where the perfect hexagonal symmetry is perturbed.

When a system is tuned through an antiferromagnetic quantum critical point, then if that system has a high density of f-electrons, then deviations from Landau Fermi-liquid behavior can be expected. This is true for compounds containing Yb, Ce, and U [49]. The AFM boundary is defined by T_N, and when T_N is driven to zero through the tuning of some parameter like magnetic field, or chemical doping, then there is an abundance of low-lying and extended spin-fluctuations which mediate the interactions between quasiparticles. One can imagine the masses of the QPs and their scattering cross sections increasing during this suppression of T_N. Thus, one asks how does this phenomena physically manifest itself?

Examples of compounds that follow this are $YbRh_2Si_2$[43], UBe_{13}[44], $U_{0.2}Y_{0.8}Pd_3$[45], and $CeCu_{5.9}Au_{0.1}$[46]. They are all united in their high density of f-electrons. In the temperature dependencies of their heat capacities, resitivities, and magnetic susceptibilities, they are found to deviate from Fermi liquid behaviour, where $C/T = \gamma$, a constant, $\rho = \rho_0 + AT^2$, and $\chi \neq \chi(T)$. Observed here is a logarithmic temperature dependence of the heat capacity, portraying an increase in entropy as temperature is lowered, an either linear or non-integer power of temperature for the resistivity, and the same for susceptibility. For example, in $CeCu_{5.9}Au_{0.1}$, $C/T \propto \ln(T_0/T)$ from 1 K to below 0.1 K. What is assumed is that, when this model is relevant, spin fluctuations dominate the spectrum of possible spin states, suggesting the battle between two phases. By utilising a free energy expression

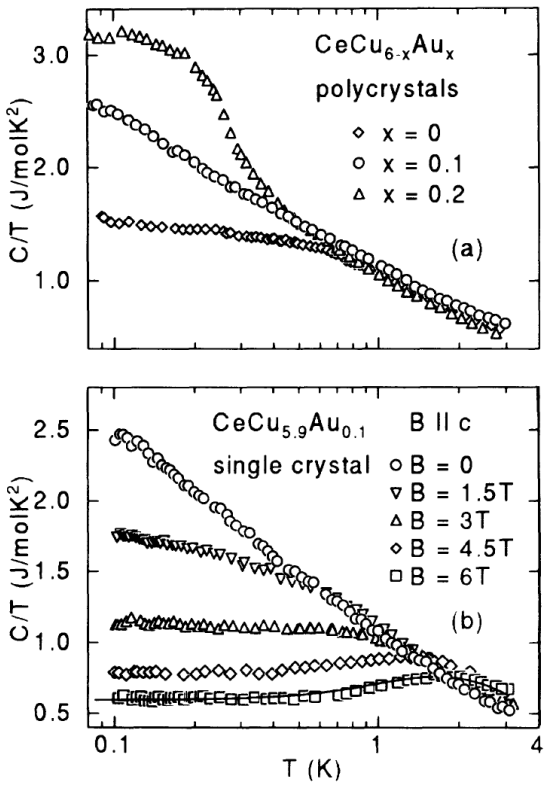

Figure 1.9 *Heat capacity measurements on $CeCu_{5.9}Au_{0.1}$, taken from [7]. Upper: variation in amount of Au doping, x, and its effect on heat capacity, where $x = 0.1$ leads to non-Fermi liquid behaviour, and $x = 0.2$ leads to a low temperature magnetic transition. Lower: applying magnetic field brings back $C/T = \gamma$, and moves the entropy upwards in temperature.*

for an AFM fluctuating system, the heat capacity can be formulated[47] as

$$C_{sf} = \sum_q \int_0^{\omega_c} d\omega c(\omega) \frac{3}{\pi} \frac{\Gamma_q}{\omega^2 + \Gamma_q^2} \tag{1.17}$$

$$c(\omega) = (\frac{\omega}{T})^2 \frac{e^{\omega/T}}{(e^{\omega/T} - 1)^2} \tag{1.18}$$

where ω is the frequency of the fluctuating spins, Γ_q represents the relaxation frequency of a spontaneous spin fluctuation of wavevector q, and $c(\omega)$ is the heat capacity of a harmonic oscillator of frequency ω, being implicitly dependent on T; thus the heat capacity is the sum over all q-states encompassed within the bulk, leading to a logarithmic dependence; this is dependent on the dimensionality of the system d being 3, and the critical exponent z being 3 [48]. If this dependence continues to low temperatures, as shown in Figure 1.9, and specifically does not seem to deviate from this trend right up to the experimental limit of measurements, then the possibility of a $T = 0$ K magnetic transition, or more likely a very low temperature transition, is present.

Either of these possibilities suggest long-range magnetic order breaking down Fermi liquid theory, leading to the temperature dependencies seen here. Alternatively, these measurements can be explained by the system becoming a "two-

channel" Kondo system [49], which can occur due to an increase in quadrupolar interactions; for U atoms in a $5f^2$ configuration, and Ce atoms in a hexagonal Ce^{3+} symmetry, by allowing local spins to interact with two separate seas of conduction spins, this achieves the level of interactions required. Thus, any evidence of similar trends seen in UAu_2 could be explained by the same phenomena, and as is shown in Chapter 4, the case for this being true is laid out.

1.3.2 URhGe

In orthorhombic uranium compounds, the ability to house ferromagnet exchange fields and superconducting coupling simultaneously leads one to think beyond current theories. As conventional superconductivity requires electrons of opposite spin to couple, the constraint on there being only common-spin electrons in these ferromagnetic materials means their properties are ripe for understanding unconventional superconductivity. URhGe was first discovered in the 1990s [51, 52] during a survey of UTX materials, where T represents transition elements, and X represents either Si or Ge. The orthorhombic crystal structure as shown in Figure 1.10 supports a magnetic moment of size $0.43\mu_B$ pointed along the c axis, being the easy magnetisation axis [50]; the b and a axes represent the hard and harder magnetisation axes, as shown by susceptibility measurements [53] in Figure 1.11. At zero field, superconductivity occurs at a temperature T_c of at the most 275 mK [1], well within the ferromagnetic phase which the system transitions into at a temperature well over ten times T_c, being 9.5 K. Although a magnetic field of $\sim$ 2 T along the b axis breaks down the superconductivity, ramping the field up to 8 T re-activates the condensate [54], presenting the first material of its kind to have re-entrant superconductivity; the phase diagram displaying this behaviour is shown in Figure 1.12.

It should be noted, however, that previous evidence of materials displaying both magnetism and superconductivity does exist. This is in the form of the Chevrel phase and borocarbide compounds [55–58], where the Curie temperature is below the superconducting temperature, indicating a weak form of ferromagnetism, and there is a lack of interaction between local moments and conduction electrons, indicating the separation of the phenomena. In fact, the order parameters for superconductivity and magnetism are thought to be modulated such that they oscillate out of phase with one another, minimising the spatial overlap.

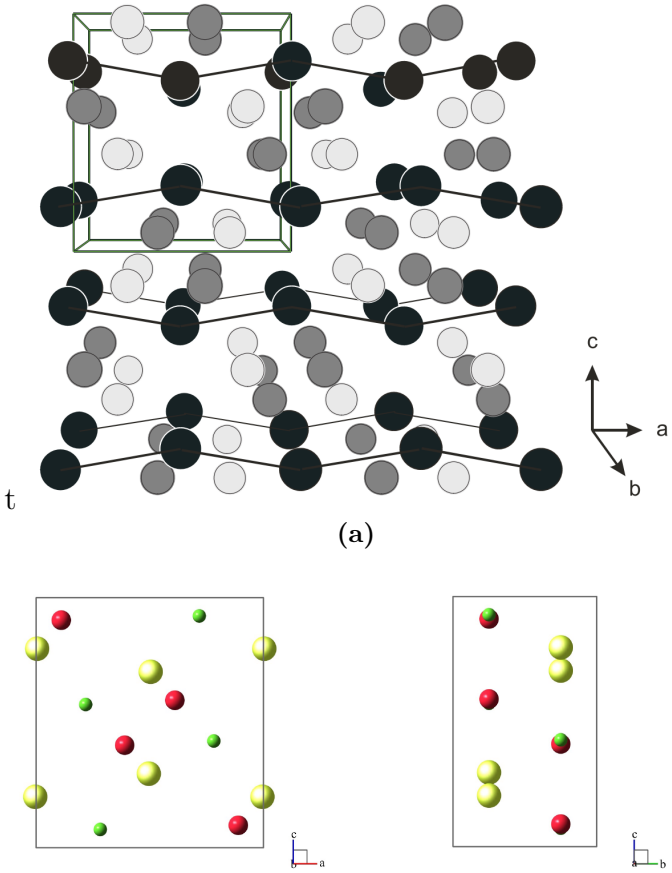

Figure 1.10 *The crystal structure of URhGe as viewed from various perspectives. (a) the ac plane is presented, with the dark-grey-white spheres representing U-Rh-Ge atoms. U atoms form a chain along a, and their moments point along c [50]. (b) The same plane is shown, but only a single layer of the atoms present, with gold-red-green representing U-Rh-Ge. Also in (b) is the bc plane, showing the slight displacement of U-atoms. The strong alignment shown leads to little structural anisotropy. In the ab plane, however, distorted hexagons are formed by the U-atoms.*

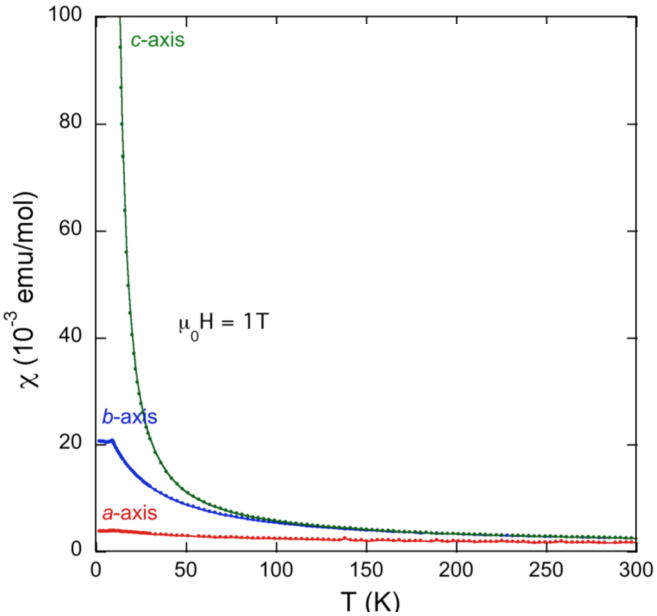

Figure 1.11 *The temperature dependence of the magnetic susceptibility of URhGe along each crystal axis, showing the anisotropy between different axes [53].*

In URhGe, a rotation of the magnetic moment from the *c*- to *b*-axis at similar fields to the re-entrant superconductivity [59] is observed. This is similar to the transition in UGe_2 from one ferromagnetic phase to another, in that there is no symmetry breaking in the moment rotation, and one can force the moment to rotate back through applying 1 T along the *c*-axis. Presented here are all previous attempts at measuring the heat capacity of URhGe, and the links between unconventional superconductivity and the coexistence of magnetism and superconductivity.

Ferromagnetic Superconductivity

There are four compounds to date that display this property, being URhGe, UGe_2, UCoGe, and UIr [1, 28, 61, 62]. What should be clear is that they display a full immersion of the two phenomena, or phrased another way, the bodies that carry the spin of the exchange field also conduct the current. Alternative scenarios include a simultaneous display of both by different aspects of the material, like ZrZn2 [63], or periodic domain-like magnetic structures characterising ternary rare earth compounds, allowing the Anderson-Suhl state [64]. Another simple explanation for how the coexistence is possible involves the upper critical field H_{c2}. If H_{c2} is above the field felt by the material, whether that's from an external or internal field, then the superconducting mixed state defined for type II superconductors is allowed. This is the case for the low-field superconductivity in URhGe, which due its large moment is effectively constantly under the influence

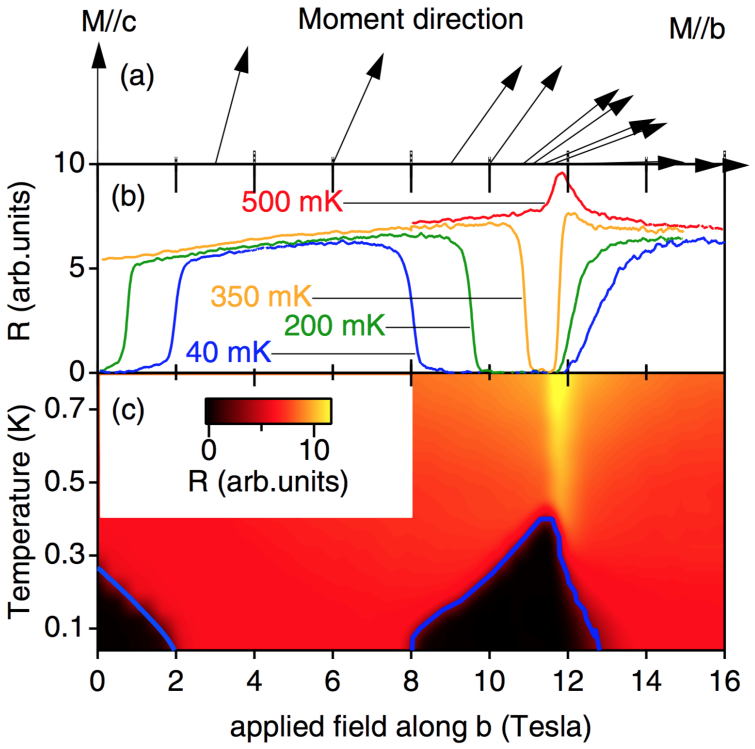

Figure 1.12 *The coincidence of a metamagnetic and superconducting transition in URhGe, for field applied along b [60]. (a) The moment rotation as determined by neutron diffraction, occurring at $B = 12$ T. (b) Resistivity measurements at different temperatures, revealing the two quantum regions between 40 mK and 350 mK, as well as a peak at the mid-point of moment rotation. (c) A contour map revealed from resistivity measurements, with legend indicating phase.*

of a field, placing it in a state above H_{c1} [65]. This also is the case for UGe_2 [66], which requires the application of pressure to achieve superconductivity; at a pressure of 12 kbar for which T_c is highest, a critical field of 7 T also exceeds the paramagnetic limit, thus falling into the triplet spin category. However, the high-field behaviour in URhGe cannot be explained by any of these possibilities, for any paramagnetism of the normal state is overruled, and any domains left in the structure are unified. In fact, for all the materials listed above, their H_{c2} is much larger than their paramagnetic limiting fields $H_p \sim 1.84 T_{sc}$. Thus, the only possible coupling that would allow this is triplet-spin Cooper pairs.

The scale of H_{c2} and its relation to the superconducting temperature is through the idea of an "orbital limit", which is defined as when the density of vortices that penetrate through the condensate grow to the point where their intra-distance (distance between the vortices) is comparable to the superconducting coherence

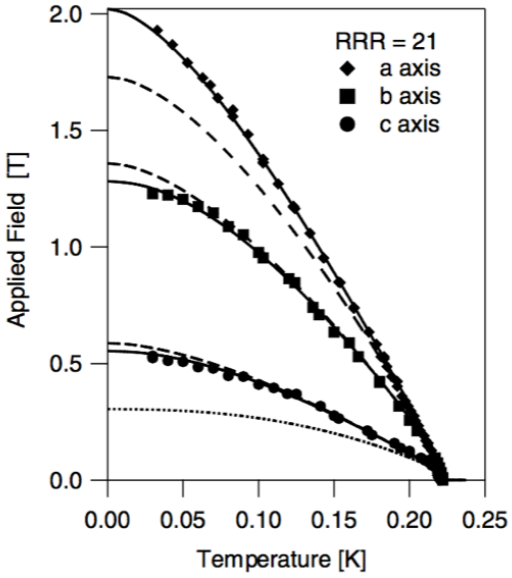

Figure 1.13 *The temperature dependence of the upper critical field is shown, calculated from resistivity measurements in [67]. The solid lines represent calculations done for an ESP gap with line nodes in the bc plane. The dashed lines are from BCS calculations, and the dotted line for BCS-with-paramagnetic-limiting calculations.*

length, ξ. The flux density through the condensate is equal to a flux quantum ϕ_0 divided by the area of the vortex core, being roughly $\pi\xi^2$. This leads to an upper critical field of [25]

$$H_{c2}^{orb.} = \frac{\phi_0}{2\pi\xi^2} \tag{1.19}$$

which in turn is proportional to T_{sc}^2, and this was experimentally verified [67] by measuring the resistance along all three axes; these are shown in Figure 1.13. Also shown are some theoretical predictions for H_{c2}, depending on certain models; for a BCS model with paramagnetic limitations, H_{c2} is severely reduced compared to what was measured, whereas a BCS model without the paramagnetic limitations predicts values just above those measured for the b and c axes, and below those for the a axis. Thus both BCS and paramagnetic limiting appear irrelevant for explaining the data. In order to find the right model, the anisotropy between the axes was found to reveal further insight. The ratio of the values for H_{c2} along the b and c axes was found to be temperature independent, whereas for that between a and either b or c, as temperature dropped from T_{sc} to zero, the ratios increase by 20 %. This turns out to be consistent with both an ESP gap, and line node in the bc plane, shown by the accurate fits to the data. Pauli paramagnetic limitation only applies to suppressing the component of the order parameter corresponding to the Cooper pairs that align/anti-align along the field direction, and so for a material whose spins are confined by the crystal field to be along an axis normal to the field, this limitation is irrelevant. Triplet pairing suggests that the pairing mechanism is of magnetic origin.

Additionally, the authors of [67] performed their measurements on a low-quality single crystal and a high-quality polycrystal, achieving the observation of superconductivity only in the latter. This mirrors what was achieved in this work, as shown in chapter 5. The fall of T_c with the RRR (residual resistance ratio, where the ratio of electrical resistance at ambient and low temperatures indicates the crystal quality) turns out to be a strong indicator of unconventional superconductivity [68]. This is due to the anisotropic nature of the gap; for BCS theory, the gap is isotropic, so scattering off non-magnetic impurities, which can be the culprits for the low RRR, will not destroy a Cooper pair. For unconventional superconductivity, any scattering event can potentially move an electron pair from the direction of positive to negative gap, breaking the pairing.

As for why a polycrystal has a better chance of displaying superconductivity than a single crystal, this is related to the difficulties in sample growth. In most methods of crystal growth, a molten mixture of the different elements is placed at a temperature which when cooled carefully, will result in the required compound. From the experience of the crystal growers, namely Prof. A. Huxley, what is found is that the window of opportunity in which the perfect composition of U, Rh, and Ge occurs is small. One has two options at this point, each resulting in either a polycrystal or a single crystal: either place the system at the perfect point in terms of composition and cool rapidly, or cool slowly and the equilibrium composition solidifies from the liquid. Any disorder in either is enough to induce pair-breaking scattering. This is why more successful experiments with URhGe are performed on polycrystals rather than single crystals. This difficulty is reinforced in [69].

Is the high-field superconductivity in some ways considered to be a different type of superconductivity to that observed at low fields? This is a question, due to the fact that H_{c2} is overcome at around 2 T [67], and to assume that H_{c2} remains constant could be presumptuous. By mapping out the orbital limiting field over the temperature-field landscape, as is shown in in Figure 1.14, one sees it smoothly rise up to H_{c2}, then maintain its position below the external field up to 8 T, and then rise above again. This evolution of the orbital field is unique; as stated in equation 1.19, it is dependent on the superconducting coherence length. The critical fields of both low- and high-field superconductivity conform to a description of $H_{c2} \propto 1/\xi^2$, peaking at the field value that causes the moment rotation. BCS provides a cause of this [6], in the equation for the coherence length

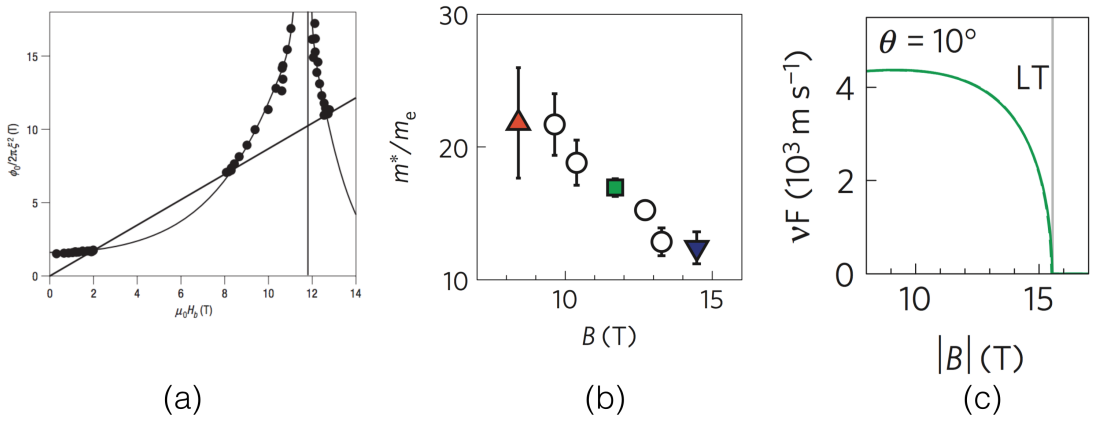

Figure 1.14 *The link between critical field and effective mass is made clearer. (a) A value for the geometric average of the critical field is calculated from resistivity measurements performed in [54], where the fit line is an interpolation, and the straight line is manually put in to pass through the limiting fields of the superconducting regions. (b) From [2], the change in normalised effective mass as a function of field drops by a factor of two. (c) The drop in Fermi velocity calculated from the dropping effective mass, and increasing Fermi momentum k_F; LT stands for Lifshitz transition, as is proposed in [2], and the angle θ corresponds to field direction from b axis in the bc plane.*

$$\xi = \hbar v_F/\pi\Delta, \text{ and } v_F = \hbar k_F/m^* \tag{1.20}$$

where either a collapsing k_F, diverging m^*, or both simultaneously changing as such leads to the correct behaviour for ξ to align with what is seen in Figure 1.14. Alternatively, as stated in [54], ξ is inversely proportional to T_{sc}, so a significant increase in that would also have the same effect. To achieve that increase, however, is possible through the transition temperature's exponential dependence on effective mass, so moderate changes to m^* could account for the superconductivity in URhGe. Later came some measurements of quantum oscillations in the low temperature resistivity in URhGe [2], and through the amplitude of those oscillations it is possible to gain a value for the effective mass. This value drops by a factor of two from 10 to 15 T, also shown in Figure 1.14. When combined with the values found for k_F, this does lead to a decrease in v_F, which can account for the necessary change in critical field to achieve both low- and high-field superconductivity.

[6]It is valid to use these BCS equations, as they are based on the assumption that there is pairing between electrons to create an effective boson, allowing the condensate to be multiply occupied. This is true for both conventional and unconventional superconductivity.

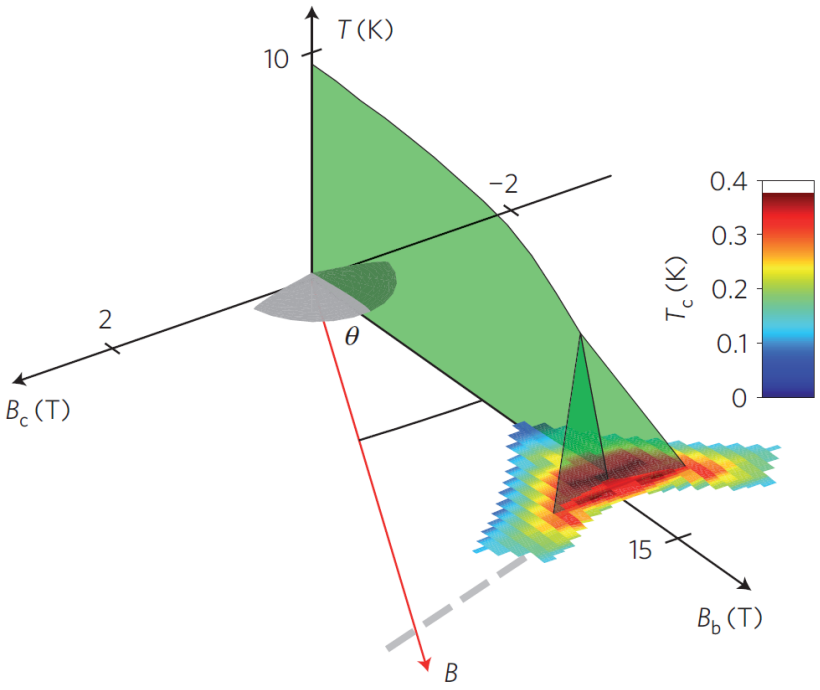

Figure 1.15 *The landscape in T-B_b-B_c space for the phases of URhGe [2]. The green planes indicate ferromagnetism, and as field is increased along b, a tri-critical point is encountered. This is the point at which the magnetic moment rotates from the c-to-b axis. Two first-order transition lines emerge, their temperatures suppressed to 0 K, defining two QCPs. The colour maps on the $B_b - B_c$ plane indicate the transition temperature into superconductivity.*

Thus, it is clear that these fundamental values of Fermi velocity and effective mass are strongly coupled to these quantum phenomena, and so the heat capacity gives another window into these. Now the history of attempts to measure the heat capacity of URhGe will be detailed, giving reason as for the need for high-field measurements.

Heat Capacity Attempts

The scale of the heat capacity in URhGe is relatively large. This stems from it belonging to the "Heavy Fermion" family of materials, displaying a large density of f-electrons. Below 1 K, as is expected for any material in such conditions, the heat capacity drops in magnitude along with entropy, as does the electrical resistivity. This is due to the range of energies available to the electrons becoming less, as described by a shortening Boltzmann distribution. So, URhGe becomes a better conductor of electricity, indicating an increase in the measure of order

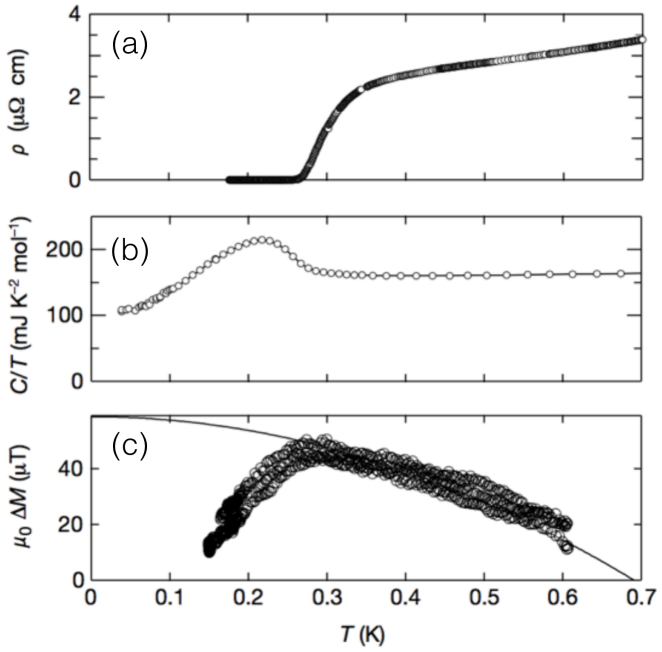

Figure 1.16 *The superconducting transition measured in a variety of polycrystals of URhGe [1]. (a) The electrical resistivity smoothly dropping to zero. (b) The specific heat capacity showing Fermi liquid behaviour above T_c, the characteristic peak and drop below, down to around 40 mK. (c) Change in static magnetisation with a constant applied field of 0.05 T.*

within, and for this to reflect in a drop in the heat capacity indicates nothing out of the ordinary is taking place.

The scale of the values can be indicative of electron behaviour; for example, if the system is in a Fermi liquid state, then the heat capacity divided by temperature should be independent of temperature, $C/T \propto \gamma$. This has been discussed in previous chapters, but as a reminder, the value γ is the Sommerfeld coefficient, being equal to $\frac{(\pi K_B)^2}{3} n(\epsilon_F)$. The density of states at the Fermi surface, $n(\epsilon_F)$, is related linearly to the Fermi velocity v_F, allowing insight into the dynamics of the electrons considered responsible for the high levels of correlation in itinerant electrons. Between 300 mK and a little above 700 mK, this is exactly the case, with a value for γ measured to be 160 mJ/mol.K^2. For the values of effective mass shown in Figure 1.14, this gives a Fermi velocity of around 2000 m/s, implying a large coherence length for the superconducting pairs.

Shown in Figure 1.16 is a variety of measurements reported in [1], performed on polycrystals of high quality. These cover the superconducting transition at a temperature of $T_c \sim 250$ mK. The authors were able to grow better

quality polycrystals than single crystals, and due to the effect of crystal quality being severely detrimental to unconventional superconductors criticality, lowering T_c significantly, a polycrystal has a much better chance of becoming superconducting; this was ensured by observing the residual normal-state electrical resistivity to be below 30 $\mu\Omega$cm.

The resistivity shown drops by just over 2 $\mu\Omega$cm to zero, over a temperature width of roughly 80 mK. A small tail is seen at the lower-temperature limit of the drop, which when combined with the temperature width being comparable to T_c itself, suggests the superconductivity is not uniform across the sample; domains can exists, especially so for a polycrystal, and thus any fields felt by the sample are inhomogeneous in their distribution. Nevertheless, this is still an example of a relatively clean transition into superconductivity.

The heat capacity experiences a jump at the same point as when the resistivity hits zero, and as the onset of diamagnetism begins. The resistivity and magnetisation measurements indicate that superconductivity plus the Meissner effect is being activated, and the heat capacity ensures that it is a bulk property rather than just some surface effect. Additionally, the size of the jump is comparable with the magnitude of C/T, meaning that the majority if not all the quasiparticles that make up the Fermi surface occupation are responsible for the superconductivity. After the jump, the heat capacity proceeds to steadily reduce towards a non-zero intercept with the axis. Complex interactions between spins can cause this, as proposed in [1] in the form of spin-orbit coupling. If the system is made up fully of spins up or down, such that the Cooper pairs are either $\uparrow\uparrow$ or $\downarrow\downarrow$[7], then by spin-splitting the Fermi surfaces, one could argue that a line node leads to $C \propto T^2$ from one of the surfaces. The opposite spin Fermi surface would continue to contribute a normal state $C \propto T$ relation. Thus, $C/T = a+bT$ being broadly consistent with the data suggests the applicability of this Fermi surface model.

In [70], the field-dependence of the effective mass was investigated through heat capacity measurements at a fixed temperature of 400 mK. An enhancement of the effective mass was found, increasing by 40% at the field of moment rotation. This can be explained by an increase in magnetic fluctuations. When the field along b

[7]The possibility of an electron occupying a state described by $|\uparrow\downarrow + \downarrow\uparrow>$ is thought to be suppressed by the spin-splitting of the Fermi surface.

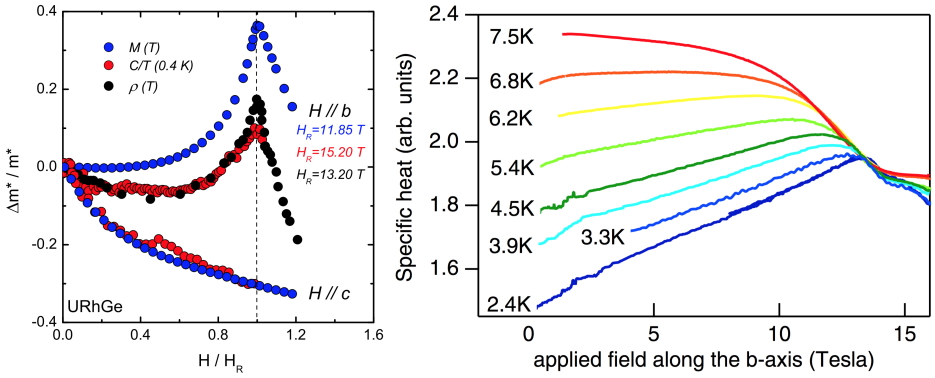

(a) (b)

Figure 1.17 *(a) Comparison of the field dependence of the effective mass m for H||b & H||c obtained from magnetization, specific-heat and transport measurements [70]. (b) The field dependence of the heat capacity measured by AC methods, in arbitrary units, for a variety of temperatures. These measurements were made at different constant temperatures. A single crystal of a few milligrams with a flat surface perpendicular to the b-axis was glued on to a tensioned chrome-constantan thermocouple. The AC heating was delivered via an optical fibre [60].*

reaches a value that balances out the anisotropy between the *b*- and *c*-axis, this allows the fluctuations to flourish. This is investigated further in the neutron studies shown in chapter 6.

The works referenced above are the only evidence of heat capacity measurements taken below 1 K. Above 1 K, it becomes easier to measure with an applied magnetic field, as the performance of the equipment involved is more stable. Thus, some more measurements exist [60]; these are shown in Figure 1.17b, being heat capacity data taken between 2.4 K and 7.5 K, for a field range of 0 T to 16 T. Here the effective mass changing with field is inferred from the scale of γ, and as the previously-explained orbital limit is the only applicable limit in a triplet-spin superconductor, then the effective mass can be an indicator of which field ranges are above or below the limiting fields. The data shown at 2.4 K follows a fairly linear increase from 0 T up to the field at which the moments fully rotate, being in the vicinity of 13 T. The magnitude grows by around 30%, which if the itinerant electrons are fully responsible for, indicates a 30% growth in the effective mass of the electrons. However, this is not large enough to account for the high-field superconductivity. Thus, the high temperature of this measurement can potentially distort the inference of the effective mass, giving a reading that underestimates the true growth during the field increase.

Additionally, the authors of [60] claim their values of C_e at 2.4 K & 0 T are 25% larger than those at 0.3 K from [1]. This isn't clear due to two reasons: the lack of units in Figure 1.17b, and the method used to measure heat capacity. The AC method gives an estimate of the absolute value, as explained in chapter 2. Thus, there is still an open question about the behaviour of heat capacity in critical parts of the phase diagram. Finally, the authors of [60] claim that the sample did rotate when under field, meaning that the true field felt along the b axis was smaller than what is reported, adding ambiguity to the location of the moment-rotation transition. This issue was also encountered, and the experimental details on how to prevent this are given in section 3.2.1.

In addition to these measurements on pure URhGe, studies have been done on doped compounds. $UIr_{1-x}Rh_xGe$ was studied [71] to understand the effects upon the magnetism present; an abrupt first-order transition was found for $x = 0.56$, transitioning from ferromagnetism to antiferromagnetism. The heat capacity curves measured reveal a similar value for entropy between UIrGe and URhGe, even though the scale of γ for the former is more than four times bigger than for the latter.

Recent work [53] found that applying uniaxial pressure opened up the superconducting phases, combining the two field-separated regions into one. Additionally, the superconducting transition temperature is seen to double, so this effect of pressure is seen to enhance the superconductivity. This is thought to occur due to the pressure reducing the distortion of the hexagons in the $a - c$ plane, lessening the level of anisotropy between the b and c axes. This may allow a combination of magnetic fluctuations along both the longitudinal and transverse directions. Measurements of the NMR [72] at high fields also revealed that although longitudinal fluctuations were enhanced, so too were transverse. The combination of these pressure and NMR measurements may well contradict the result found in the 1980s [26] that only longitudinal fluctuations can lead to superconductivity. More about this is discussed in section 1.4.

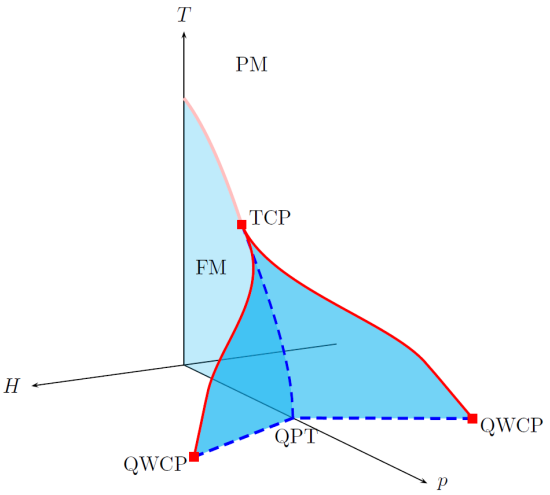

Figure 1.18 *Schematic of generic phase diagram for quantum ferromagnets, defined by T, H, p, showing the different magnetic phases, the tri-critical point, the quantum phase transition and the quantum wing critical points. Solid/dashed lines are second/first-order transitions, and the blue planes are first order.*

1.4 Quantum Ferromagnets - Wing Structure of Phase Diagram

The phase diagram for URhGe is a relatively common type of shape; a few other compounds also display a tri-critical point from which two symmetric 'wings' fall down to $T = 0$. Some of these are UGe_2 [73, 74], and $ZrZn_2$ [75], where the generic phase diagram for these compounds is shown in Figure 1.18. The wings trace out thermodynamic first-order transition lines, which define the boundary of a full second-order surface. The symmetry of the wings about an axis stems from the mirror plane in the crystal structure, which for URhGe is the *a*-*c* plane. For $T > T_{TCP}$, the PM-FM transition is second-order, as is expected [13, 76]. However, the application of an external parameter (like magnetic field for URhGe, and pressure for UGe_2) leads to the change of order; even further application drives the system past meta-magnetic or structural transitions.

Not only is the absolute position of the end-points of these lines important, but so too is their slope. As is shown theoretically [77] and experimentally [78] by recent work, the lines that fall away from the TCP are tangential to the second-order line, which contrasts with what is shown in [2] and Figure 1.15, where the change in gradient as the line begins is discontinuous. The Clausius-Clapeyron relation dictates that the slope of a transition line in a magnetic field - temperature phase diagram, as temperature tends towards zero, starts to diverge towards infinity [9]. Thus, at low enough temperatures, to cross the transition line will require smaller and smaller changes of the control parameter, as was verified experimentally for

the first time in [79][8].

The wing's shape is therefore very specific to the physics present; a quantum ferromagnet has the specific properties of the wings existing completely perpendicular to the $T = 0$ plane, but not so for the $H = 0$ plane. To be able to support these specific shapes with thermodynamic evidence would be ideal, as could be done with heat capacity. This is possible by measuring across the transition lines, comparing the shape of the C/T vs. T curves for a variety of field values. A prediction from Belitz and Kirkpatrick [80] is that the phase diagram follows a particular rule, quantified below.

$$\frac{dT}{dH}_p = -\frac{1}{T^n}\frac{\Delta m}{\Delta \gamma} \tag{1.21}$$

where n is 1 for Fermi liquids, Δm is the change in order parameter (being magnetisation for URhGe), and $\Delta\gamma$ is the change in Sommerfeld coefficient. This equation comes from applying the third law of thermodynamics to the Clausius-Clapeyron relation.

In URhGe, recent magnetisation measurements [81] in the high-field region of the phase diagram revealed further detail concerning the wing structure. Specifically, the location of the TCP and the Quantum Wing Critical Points (QWCP), which are the $T = 0$ ends of the first-order transition lines, are pinpointed to higher accuracy. High sensitivity to the angle θ between the magnetic field inflicted and the crystallographic b-axis (all taking place in the $b-c$ plane) of the magnetisation and magnetic torque imply the sharpness with which the wings turn away from being parallel to the b-axis to with the c-axis, and the level of the anisotropy present within this material; an angle θ of 0.8° is all that's needed for the field at which the moment rotates to change by around 1 Tesla.

There is also high sensitivity to the temperature; the pinching of the peaks in dM/dH towards the b-axis as temperature is raised from 1 K to 6 K displays this for the wings. This agrees with the ideas proposed by Tafour [77], where the peaks becoming more aligned with the b-axis corresponds to the wings falling tangentially away from the TCP. This, along with the torque, is shown in Figure 1.19.

[8]To probe the wing-structure phase diagram requires three separate control parameters to be varied. As magnetic field technology in the 1970s was not as it is today, then the electrical field acted as the third parameter, being critical for Dysprosium Aluminium.

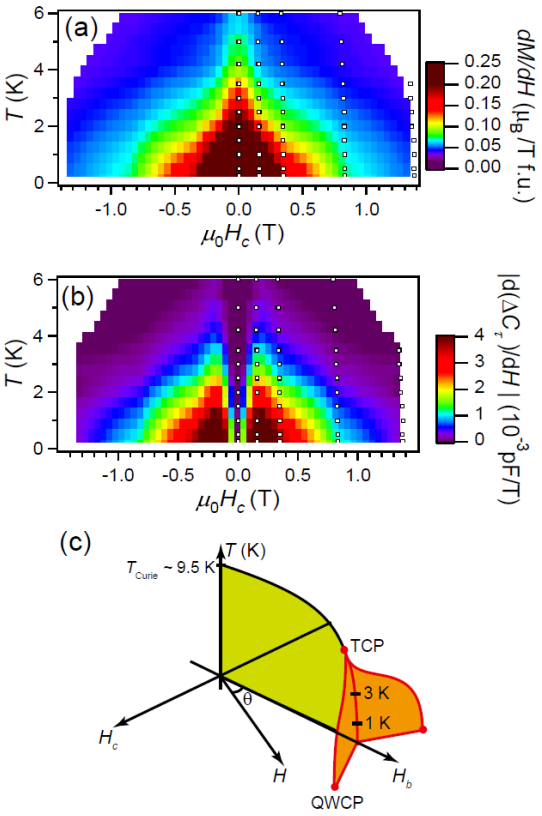

Figure 1.19 *The peak of (a)dM/dH and (b)$d(\Delta C_\tau)/dH$ are shown in a contour plot, referring to the susceptibility and torque of the sample, spanning the Temperature-Field(c-axis) plane, i.e. $\theta = 0$; (c) the phase diagram constructed from the measurements [81]. Details are in the text.*

One result that adds complexity is that the first-order transitions are determined to be relatively weak, inferred from the gradient of the torque decreasing as θ increases. However, the signature of the transition does remain up to 6 K, but only again for very small angles. Substantial quantum fluctuations can be found in a system with weak first-order transitions, because of the broadening of the transitions with temperature and the small scale of the hysteresis in critical field. These fluctuations can be visible with small angle neutron scattering, focussing on such small scattering vectors that weak magnetic fluctuations would be visible. This is one of the justifications for performing this exact experiment, with results given in chapter 6.

One final previous measurement that is worth mentioning are NMR measurements [72]. The high-field critical behaviour can be quantified not only in terms of a superconducting order parameter becoming non-zero, but also in terms of a fluctuating magnetic moment, due to the rotation of the moment for fields around 12 T. The authors were able to map out the intensity of the fluctuations by measuring their relaxation times, $1/T_2$, shown in Figure 1.20. The intensity is highest at $H_b = H_R$, the rotation field, where the values for $1/T_2$ become too

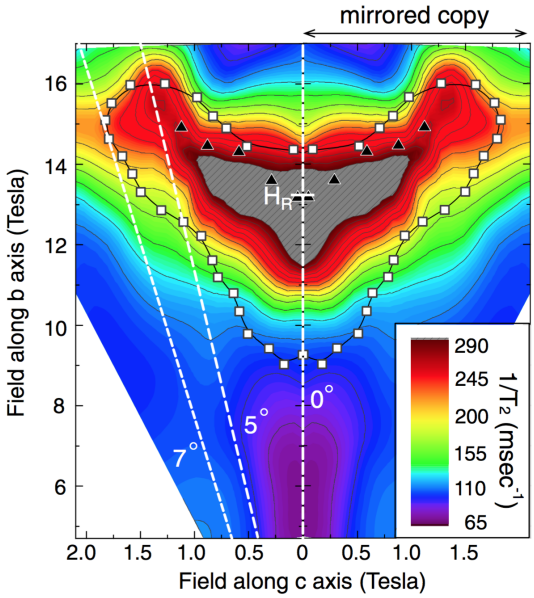

Figure 1.20 *The results for $1/T_2$, the rate of relaxation of a magnetic fluctuation, are shown across the H_b-H_c phase diagram, for $T = 1.6$ K. The white squares indicate the superconducting transition from resistivity, and black triangles indicate the metamagnetic transition [59].*

small to measure. There are other maxima at fields that include both b-and-c-axis components, and these indicate phase bifurcation points, previously introduced in this section. The coincidence of the bifurcation points, the resistivity-drop indicated by the white squares, and the metamagnetic transitions indicated by the black triangles, all point to the existence of a tri-critical point (TCP). These can induce divergent susceptibilities in both the order parameter, and the physical quantity that is conjugate to the tuning-parameter of the transition, being the average magnetisation along b. This leads to a divergence of the longitudinal component of magnetic fluctuations, whereas if a QCP was the pursued phenomena, then the transverse magnetic fluctuations would become enhanced. Thus, this presents an opportunity for neutrons to scatter off these enhanced fluctuations; more is said about these in the next chapter.

Chapter 2

Thermodynamic Measurements of Heat Capacity

In the first chapter, the various materials under study were described. The possible mechanism for superconductivity at high magnetic fields in URhGe, or the presence of antiferromagnetic fluctuations in UAu_2, both have an indicator of sorts within the thermodynamics of the system. In this chapter, that thermodynamic connection will be clarified.

The non-adiabatic principle of measuring the heat capacity, that is applying a known amount of heat to a system while measuring the temperature with time, stems from the early 19th century [82]. Thermal isolation is required, to maximise heat flow ΔQ purely to the sample, but during the 1960s [83] new methods were developed, allowing the sample to be thermally coupled to the bath with non-zero conductance. In this work, a non-adiabatic method was favoured, due to the small mass of samples. This, plus an adiabatic method, shall be described in due course. Although the methods used are not new, what differs from previous experiments are the components employed in the addenda, the method of thermometry, and the way thermal isolation was balanced with thermalisation with the cold temperatures reached by the dilution refrigerator. For more details on the differing methods, one can read a detailed review by G. R. Stewart, [84], or a more recent review by G. Ventura and M. Perfetti [85].

2.1 Heat Flow - Methods of Measurement

The fundamental thermodynamic relation, from which the methods used for measuring changes in entropy come from, is

$$dS = \frac{dQ}{T} \tag{2.1}$$

where dS is the change in entropy in a closed system through which an amount dQ of heat flux moves in or out, at a fixed temperature T. That summarises the experimental process; add heat, and track the temperature of the system as the heat is dissipated throughout.

Firstly, I will explain two experimental quantities that are frequently referenced throughout this chapter. They are the relaxation time, or time constant, and the thermal conductivity. It is the combination of these quantities that results in knowledge of the heat capacity, and so understanding the individual parts is required to understand the whole.

Relaxation Time / $\boldsymbol{\tau}$ / Time Constant This is the time taken for, on either applying or switching off a heater coupled to the sample, the relative change in temperature to be one exponential constant, being around 63%. In this setup, that time can be of the order of 5-20 s, depending on the value of the other important quantity, the thermal conductivity.
Thermal Conductivity / $\boldsymbol{K}$ This dictates how much of the heat present at one end of some thermal link can be transported along to the other end, in units of W/K. In the setup used here, this is represented by a gold wire connecting the sample platform to the cold fridge; a temperature difference ΔT will occur from some input of heat, and thus K will be equal to the power input divided by that temperature difference i.e. $K = \dot{Q}/\Delta T$. As K is generally determined by the geometry of the gold wire, then an increase in $\dot{Q}$ will result in a larger ΔT.
The way these two quantities lead into one another is representative of the underlying property of heat capacity, linking the two multiplicatively. How one accurately measures these two quantities is varied, explained below.

Three methods will be described, one in comparatively more detail due to it being used extensively. The first is known as the Adiabatic method [86], referring to the process with which heat is applied to the sample environment. The

thermal conductivity between sample and thermal bath, K_{S-TB}, is effectively forced to be zero by maintaining the temperature of the bath to match that of the sample, utilising high-speed PID functions to trigger a heater attached to the bath. The rate of change of the temperature with time gives the heat capacity; the problem with this method is the reliability of the electronics, and especially so for compounds that radiate heat naturally.

The second method is the AC method; pioneered by Sullivan & Seidel [83], the AC label refers to the heater that is connected to the sample, in that the heat supplied is delivered as a sine-wave. The frequency used is dependent on the relaxation times within the system. As the link between sample and thermal bath is via the platform onto which the sample is mounted, then K_{S-TB} is actually dictated by the link between platform and bath. How this is physically built is described in section 3.2.3. Thus, this opens the possibility that there is another relaxation time between sample and platform, introducing some lag of thermalisation. This is an effect quantified by the values τ_1 and τ_2, where the former describes the dominant platform-thermal bath link, and the latter the sample-platform link. Ideally, τ_2 is negligible, such that the temperature of the thermometer on the platform is exactly that of the sample, but this method was developed to account for those cases where τ_2 is unavoidably non-zero. Examples of this occur when measuring the thermal conductivity of samples that are large enough that in order to fully thermalise them with the bath, then they have to be physically in contact with them.

As mentioned, the limitations of this method rely on the requirement that the frequency ω falls within a certain range, being $\omega\tau_1 << 1 << \omega\tau_2$. Additionally, the method does not gain an absolute value for C, but rather an average value, due to the ambiguity in where the power from the heater flows to. Examples of the success of this method exist [87, 88], but the method is not utilised here due to the ability for the setup to bring the value of τ_2 to less than 0.05 s, and the values measured are not absolutes but rather averages of a small temperature range. The effects of τ_2 are shown in more detail in Figure 2.3.

2.1.1 Relaxation Time Method

In Figure 2.1 is shown a schematic of what the experiment environment consists of, simplified greatly. As mentioned in the caption, the described conditions are

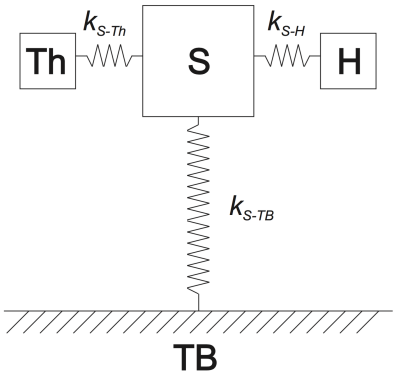

Figure 2.1 *A simplified version of the experimental set-up. Thermometer* ***Th*** *measures the temperature of itself, the sample, and the heater, while the heater* ***H*** *applies a known amount of heat. The thermal conductances between sample and thermometer/heater,* $\boldsymbol{k_{S\text{-}Th}/k_{S\text{-}H}}$*, are assumed to be infinite, whereas that between sample and bath,* $\boldsymbol{k_{S\text{-}TB}}$ *is measured.*

the ideal case for what is known as the *Relaxation Time method*, being the third method. Taking the effect of the heater as a flux of energy ΔQ, the definition of heat capacity of the system is

$$C_{system} = \lim_{\Delta T \to 0} \frac{\Delta Q}{\Delta T} \tag{2.2}$$

This is achieved by switching on the heater at time t_1, and off at t_2, causing a temperature rise from T_0 to T_1 in the system, where $\Delta T = T_1 - T_0$. Thus, by applying a small amount of heat and measuring both the temperature change and time constant, the heat capacity of the system can be calculated.

The method followed here was pioneered by Bachmann *et al.* [89], where a single period of the measurements cycle is shown in Figure 2.2. Initially, the cryogenic system is regulated to the point where the sample temperature T_0 is constant to within experimental resolution. At this point, the heater is activated, sending constant power to the system for a duration equal to $t_2 - t_1$. Once the sample is, to within the same experimental resolution as in phase I, at temperature T_1, the heater is switched off and the sample cools back to equilibrium with the thermal bath.

In order to fit to this temperature trace, one looks to literature: Bachmann *et al.* showed that by writing down a differential equation that describes heat flow throughout the system, equations for the heat capacity can be derived. These equations can be written down in two different ways, depending on how significant the value of τ_2 is. If $\tau_2 << \tau_1$, then one can use the 1-τ model, and otherwise,

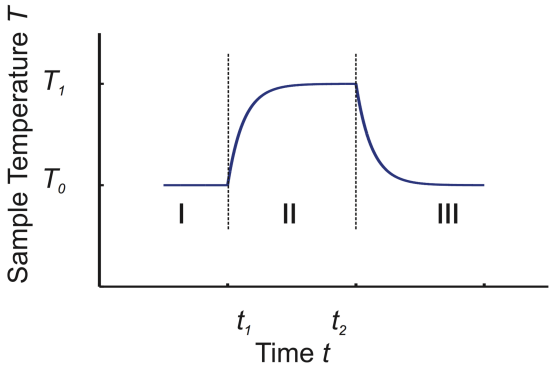

Figure 2.2 *How the temperature T changes with time t during a single period of the measurement cycle. Heat is delivered to the system only in phase II, whereas the sample thermalises to the thermal bath in phases I & III.*

the 2-τ model.

The experimental conditions necessary for use of the 2-τ model are achieved by having the sample not pressed firmly to the platform during the glueing process. The experimental achievement of this is shown in Figure 2.3. To be as accurate as possible, it is generally preferable to use a model that has the least number of fit variables, so efforts are made to minimise τ_2 enough that the 1τ model is sufficient. However, because the 1τ is a special case of the 2τ, and because the magnitude of τ_2 is seen to take significant values at the lowest temperatures, then by focussing on setting the fit parameter limits appropriately, consistent results are achievable. Here I will briefly describe both models, where their derivations can be found in the literature referenced.

2.1.2 1-τ model

Starting with the simpler model, if $\tau_2 << \tau_1$, then with reference to Figure 2.2, during phase II the temperature with time should follow

$$T(t) = T_0 + (T_1 - T_0)(1 - e^{-(t-t_1)/\tau_1}), \tag{2.3}$$

and during phase III

$$T(t) = T_0 + (T_0 - T_1)(1 - e^{-(t-t_2)/\tau_1}) \tag{2.4}$$

$$\text{where } C\dot{T} = K_{S-TB}(T - T_{bath}) + P \tag{2.5}$$

Thus by fitting to the above, one can find values of $T_1 - T_0 = P/K_{S-TB}$ and τ_1. Assuming the sample is thermally coupled to the platform, this model can accurately produce sensible values for the heat capacity, as shown in section 3.4.

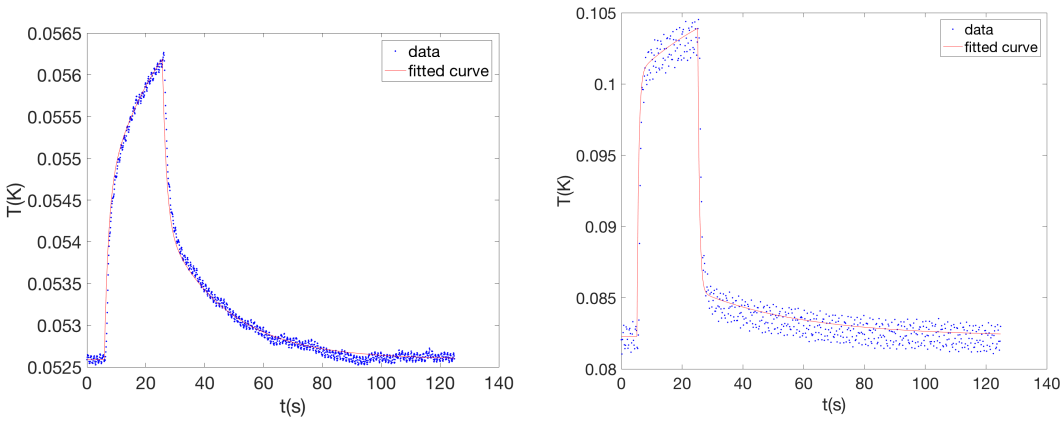

(a) **(b)**

Figure 2.3 *The effects of low conductivity between sample and thermometer are shown here by comparison between two separate experiments, both on URhGe but different samples. The sudden rise in temperature in (b) is characteristic of τ_2 being significant, as was expected in that badly-made sample platform. In (a), however, the steady rise is characteristic of the signal measured coming mostly from the crystal, and not the individual components of the addenda. The fit of the form shown in equation 2.3 is made.*

A balance must be met concerning the value of K_{S-TB}, as it determines the duration of τ_1. The longer τ_1 is, the more of an exponential curve there is to fit to, increasing the accuracy of the fit, assuming minimal instability at the base temperature. However, at the lowest temperatures, this value can approach tens of minutes for the samples used here, and this process must be repeated at least 5 times for each base temperature value, to gain reliable statistics. Thus, the other side of the balance is increasing K_{S-TB} to reduce τ_1, allowing the experiments to be completed in a reasonable amount of time; how this is physically achieved is shown in section 3.2.3.

2.1.3 2-τ model

In this case, the temperature of the system during phase II is given by

$$T(t) = T_0 + A(1 - e^{-\frac{t-t_1}{\tau_1}}) + B(1 - e^{-\frac{t-t_1}{\tau_2}}) \tag{2.6}$$

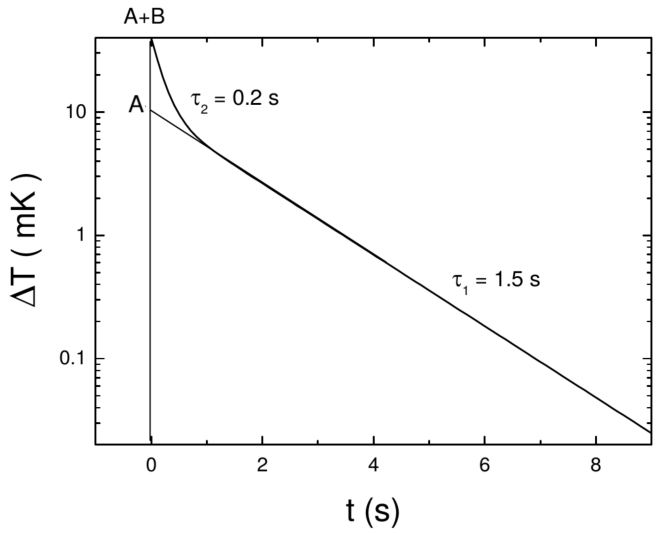

Figure 2.4 *Ideal plot of the logarithm of change in temperature of the sample plus platform, during cooling. Example τ_1 and τ_2 shown, as well as A and B, where the sum of the two give the total ΔT.*

and for phase III, the temperature follows

$$T(t) = T_0 - A(1 - e^{-\frac{t-t_2}{\tau_1}}) - B(1 - e^{-\frac{t-t_2}{\tau_2}}) \tag{2.7}$$

In order to draw appropriate values from these fits, some adjustments are made, following the work of M.Brando [90]. By analysing the logarithm of the change in temperature, one can separate out the two periods of time over which the two relaxation times dominate behaviour. For the region over which τ_1 is dominant, during phase III, the temperature with time simplifies to

$$T(t) = T_1 - Ae^{-\frac{t-t_1}{\tau_1}} \tag{2.8}$$

and thus, the logarithm of the change in temperature simplifies to

$$\ln(\Delta T) = -\frac{t}{\tau_1} + \ln(A) \tag{2.9}$$

The gradient of the straight line is therefore linked to τ_1, and the intercept to A. By fitting this equation to the temperature vs. time data after the τ_2-dominated cool-down, then one gains A, B, and τ_1. Finally, τ_2 (and thus the heat capacity) is calculated, using the following equations

$$\tau_2 = \frac{B\tau_1 C_p}{(A+B)\tau_1 K_{S-TB} - AC_p} \tag{2.10}$$

$$C = K_{S-TB}\tau_1(1 - \frac{K_{S-TB}\tau_2}{C_p}) + K_{S-TB}\tau_2 - C_p \tag{2.11}$$

where C_p is the heat capacity of the addenda, ideally measured previously. Ref. [90] gives derivations for these equations, opening up the heat capacity of the addenda as a separate variable. As τ_2 is also considered a separate variable to τ_1, then the heat capacities of all present components are now considered equally as separable[1]. The *specific* heat capacity is calculated afterwards, once the addenda and τ_2 effects have been accounted for, due to the different masses associated with the different constituents of the total system.

A critical part of the measurement process is allowing the heating to last long enough for the addenda and sample to saturate at some new higher temperature. If the heater isn't left on for long enough, as shown in Figure 2.3, then the size of the temperature change isn't indicative of the power delivered to the system; by taking the maximum temperature reached, this would correspond to a smaller amount of power relative to what was actually sent. In this work, setting the heater to remain on for $\sim 6\tau_1$ was enough to capture the necessary data, but there are cases where the heater times were short enough for extrapolations to become necessary, to see the full potential temperature increase. This is the case for the heat capacity measurements of URhGe, as shown in chapter 5.

Comparing to the AC method described beforehand, the relaxation time method does gain absolute values of the heat capacity; because the thermal bath regulates at a single temperature to within experimental resolution, then the data collected is for that temperature, and repeating the heat pulse adds samplings from the distribution of possible absolute values across the temperature variance.

2.2 Effects of heater location

One very important detail is the location of the sample heater. In order to maximise the amount of heat sent to the sample, the heater must be placed in such a way that the heat flow has no choice but to pass through the sample on the way to the bath. Unfortunately, due to the dimensions of the devices, it was initially chosen for this simple rule to be not followed. Figure 2.5 displays the possible

[1]In reality, as there are at least five separate components within the total setup, then each link between them presents a separate value of τ. Each τ may be of a similar order of magnitude, thus combining to create an effective relaxation time, but under certain conditions those differences may be amplified. However, to save on building a highly-complex model, τ_2 is treated as the average of all τ present

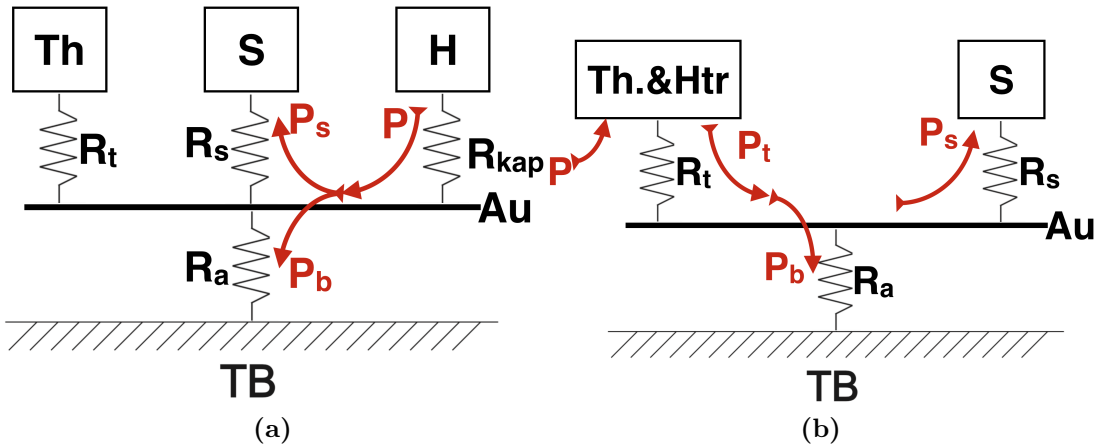

Figure 2.5 *The two experimental setups encountered within this study; R_t, R_a, R_s, R_{kap} and R_G are the thermal resistances (reciprocal of conductivity) of the links shown. The red lines indicate the flow of heat. (a) the heater delivers power to both sample and bath simultaneously, and the coupling between heater and sample, R_kap becomes critical. That between heater and bath can be simplified to $R_G = R_{kap} + R_a$. (b) The compromising setup used on UAu_2, where the thermometer additionally delivers power.*

setups, and the corresponding thermal couplings that arise. It is these differing thermal couplings that lead to different equations for the heat flow. Here, the thermal coupling measured is that between sample and bath, with no additional materials contributing at all, but in the other setups described, and thus the setups actually used, the thermal couplings between multiple components are picked up in the measurements, not all of which are representative of the sample relaxing. How this is separated out will be shown later.

It must be said that having the heater between sample and bath is what was used in all of the experiments ran. The reason for this was that building the heat capacity rig was found to be structurally more sound with the strain gauge used as the heater, otherwise between measurements the rig would fall apart. Due to this, the change in calculation of C involves starting from the two situations shown in Figure 2.5, from which differential equations analogous to equation 2.5 can be written down. Now, each of the situations encountered will be listed, along with their corresponding quantities.

Heater between Sample and Bath: Shown in Figure 2.6a, the ΔQ from the heater will be split. Quantifying what fraction of that power is sent to the

sample is desired. Starting with the split going two ways, one can say that in terms of the power sent from both heater to sample, P_s, and heater to bath, P_b,

$$P = P_s + P_b \tag{2.12}$$

$$\therefore C_s\dot{T}_s = P_s = P - P_b \tag{2.13}$$

One can represent P_b in terms of the thermal link to the bath, and a similar process applied to P_s finds the common term between the two is the thermal conductivity of the material between heater and sample, in this case being Kapton tape. Parameterising this as the thermal resistance, R_{kap}, instead of thermal conductivity, and that between heater and bath as the thermal resistance of gold, $R_G = R_{kap} + R_a$, one arrives at the differential equation

$$C_s\dot{T}_s = P\left(1 - \frac{1}{1+\frac{R_G}{R_{kap}}}\right) + \frac{T_s/R_{kap}}{1+\frac{R_G}{R_{kap}}} \tag{2.14}$$

$$\therefore \dot{T}_s - \frac{T_s}{C_s(R_{kap}+R_G)} = \frac{P}{C_s\left(1+\frac{R_{kap}}{R_G}\right)} \tag{2.15}$$

which is in the same form as the 1-τ model dynamic equation 2.5; the proof of this is given in the Appendix. The denominator of the second term, $C_s(R_{kap} + R_G)$, is equal to the relaxation time τ. If the resistance between heater and sample is finite, which would result in a non-zero $\frac{R_{kap}}{R_G}$, then τ is prolonged. Thus, this is not the absolute relaxation time of the sample, but a perturbed value that can only be fixed to resemble the true τ once the thermal links are accounted for. This can be done with the thermal conductivity K. During cooling, K should be dependent purely on R_G. The results of this method are shown in chapter 4.

Sample between Heater and Bath: Shown in Figure 2.6b, the thermometer is utilised as a heater. To do this involves applying a DC offset for a period of time while an AC current provides the thermometer excitation. Over the temperatures spanned, the heat capacity of the RuO_2 thermometer is relatively small. This means that when heated, the RuO_2 will saturate in temperature fast, having a small τ. This effect will be separable from the heating of the sample, but the mere presence of this additional τ gives reason to use more complex analysis methods. Starting with the two differential equations describing heat flow through the sample and thermometer separately, and quantifying the different thermal resistances in the system as R_t, R_s & R_a (thermometer-platform, sample-

platform, platform-bath), one can gain

$$C_t\dot{T}_t = P + P_t = P + \frac{T_p - T_t}{R_t} \tag{2.16}$$

$$C_s\dot{T}_s = P_s = \frac{T_p - T_s}{R_s} \tag{2.17}$$

By solving these as shown in the appendix, the relaxation time τ of the sample is found to be $\tau = C_s(R_a + \frac{R_s}{R_t}(R_a + R_t))$. By using the simple model proposed above, one would over-estimate the true heat capacity. How to actually gain τ and $R_{s/a}$ is as follows.

One measures the temperature difference caused by the heater, and as was the case in the method proposed by Brando [90], the rise of the thermometer is separable from the rise in the sample and addenda, as is shown in Figure 2.6. The following can be drawn from those measurements:

$$\text{Measured } \Delta T_1 = PR_t \tag{2.18}$$

$$\text{Measured } \Delta T_2 = P(R_s + R_a) \tag{2.19}$$

$$\therefore C_{Sample} = P/\Delta T_2 \times \tau_1 \tag{2.20}$$

where P & τ_1 are the power supplied by the heater, and the relaxation time of the sample respectively. Thus, by measuring ΔT_2 and τ_1, one can find more accurate values of the heat capacity of the sample. Although not implemented in this study, this provides an approach to calculating the individual thermal resistances present when one can separate out τ_1 and τ_2 clearly.

2.3 Effects of Magnetic Field

The effect of a magnetic field upon the method of measuring heat capacity is simple and accountable. The procedure reduces down to measuring the response of the sample to heat input, and if a magnetic field applied is constant to some degree of accuracy, then the system is no different to that of zero field applied, for the exception that the magnetoresistance present in the RuO_2 thermometer will cause an increase in the induced voltage. This amount of increase has been accounted for, as detailed in section 3.3.3.

The main source of noise expected is from the vibration of wires inducing an

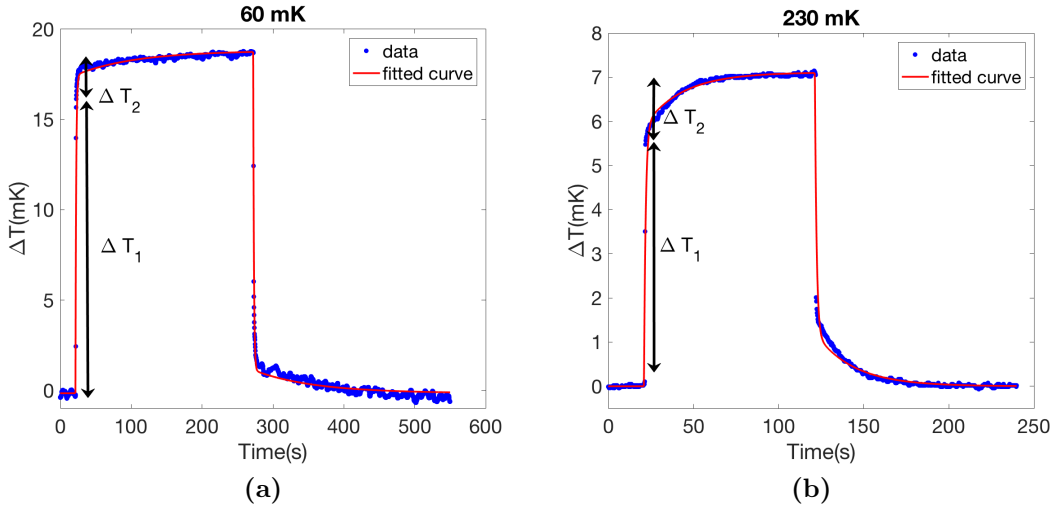

Figure 2.6 *A comparison of data taken at (a) 60 mK, and (b) 230 mK, with the RuO_2 as thermometer and heater. ΔT_1 and ΔT_2 change with temperature, indicating the change in thermal conductivity, and thus heat capacity, present over this range.*

EMF as they cross the flux lines of even a stable magnetic field.

Inhomogeneities of the field applied can clearly cause problems. As found by Stewart [84], a Germanium chip used as a thermometer was found to vibrate at a rate of 0.5 Hz, being an example of magnetoresistive materials vibrating in a non-uniform field, manifesting in the readings as low-frequency noise. The amount of inhomogeneity in the magnet used in this work is minimal, given that as the full addenda aligns axially over a distance of 0.2 cm, radially 0.5 cm, then over a distance of 1 cm, the field changes by 0.38 % axially and 0.1 % radially.

2.4 Radioactive Samples

The obstacle involved with measuring the heat capacity of radioactive samples is that the flat temperature upon which heating causes a rise is not necessarily flat - the absorption of alpha particles from the decaying uranium within the sample can cause heating. Being an adiabatic approach, a method named “rate of rise” was discovered by Trainor *et al.* [91], where the source of the heat input for calorimetry is the sample itself, and the thermal conductance to the bath is small enough for that heat to not escape. By calibrating the thermometer

separately, rather than during the heat capacity experiment, then any heating can be measured as a subtractable background, or systematic error. Thus, the heat capacity can be re-expressed from equation 2.2 as

$$C_\alpha = \frac{\dot{Q}}{\dot{T}} \tag{2.21}$$

where the radioactive heating due to the sample is quantified as $\dot{Q}$. For large samples with a $\dot{Q} \approx 10$ mW/g, this method can work at higher temperatures where the heat rise can be more than 10 % of the bath temperature, but herein lies the fault; for low temperatures, the heating is excessive. Thus, the small $\dot{Q}$ of uranium (of the order of 10 nW/g) could be more appropriate for this method, but the temperature rise caused by this heating is small enough to be unnoticeable above the thermal noise across all temperatures down to 30 mK. A calculation is shown in the Appendix, leading to a radioactive heating for 22 mg of URhGe of around 70 pW, and similar for 20 mg of UAu_2, being the weights of some of the samples measured. The power output of the heaters used, however, are of the order of 200 pW. The radioactive heating is thus contributing an additional maximum 30%. Although not negligible, the effects of this are not taken into consideration when calculating the heat capacity. Section 3.2.3 and Figure 2.3a show the calculations behind the addenda to compensate for the potential heating, and the time-dependence of the temperature at the lowest temperatures, proving the negligibility of the radioactive heating.

Chapter 3

Design & Characterisation of a Novel Experimental Setup

In the process of investigating the phase diagram of uranium compounds in the vicinity of a Quantum Critical Point (QCP), one can find oneself implementing and measuring electrical signals under conditions that are considered, in the condensed matter physics world, extreme. For example, the high magnetic fields needed to probe the re-entrant superconductivity in URhGe samples justify the use of certain materials and bespoke designs. The moment rotation seen in neutron studies on URhGe [60] from the easy c-axis to the hard b-axis leads to a torque inflicted upon the system, which must be counteracted in order for the sample not to become mis-aligned with the magnetic field applied. A new design was made, along with some prototypes, to optimise the characteristics needed to counteract all of the experimental issues, being designed, built, and tested by the author.

In this chapter, firstly an overview of the various components and equipment used will be given. Secondly, the all-important careful calibration of the thermometer at low temperature and high magnetic field will be detailed. Finally, characterisation measurements with UPt_3 will be shown.

3.1 Cryogenic environment

In section 2.1, the importance of high temperature stability of the sample environment was emphasised, being due to the basic physics of the experiment: a first-order transition leads to a discontinuous change in entropy, the consequences of which are observed in the way energy is absorbed and dispersed. If the entropy changes are small, being on a scale of μJ/K, then the energy inserted into the system must be appropriately small. The physical manifestation of this energy is heat, and so in order to have a good signal-to-noise ratio, the standard deviation of the stable temperature is desired to be of the order of 1% maximum of the temperature change due to the insertion of heat. Thus, one can see what an appropriate magnitude of ΔT is by checking the variance of temperature σ_T and scaling from there. In the set-up described here, achieving $\sigma_T \approx 0.1$ mK leads to a ΔT of 10 mK.

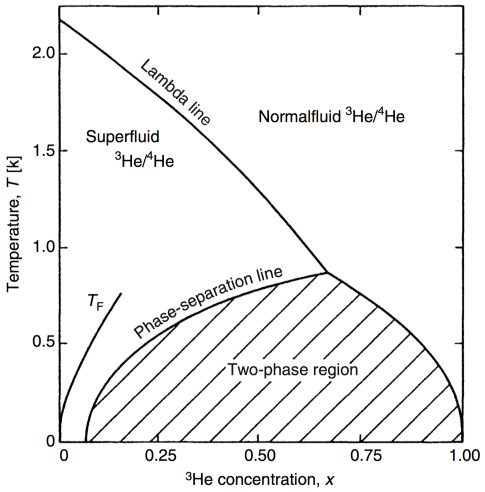

Figure 3.1 *Phase diagram of ^{3}He-^{4}He mixture [92].*

A dilution fridge was used to cool the sample down to temperatures lower than that of a Physical Property Measurement System (PPMS) device. All caloric measurements reported in this thesis have been carried out in a Cryogenics dry ^{3}He-^{4}He system, capable of reaching temperatures of 20 mK. Also installed in the fridge is a 17 T superconducting magnet, also manufactured by Cryogenics. The working principles of a dilution refrigerator are well documented [92], having been first conceived by Heinz London in the early 1950s, and then experimentally verified in various stages in Manchester and Oxford [93]. When a mixture of ^{3}He and ^{4}He is made at low temperatures, a particular phenomenon is induced. Due to the boiling point of ^{3}He being lower than that of ^{4}He, then if a pump is attached to the mixture, then the fraction of ^{3}He present will reduce first, or faster than that of ^{4}He. This is due to the lighter mass presenting a smaller energy of vaporisation. One would expect long pumping times to reduce this fraction to zero, but in fact it saturates at

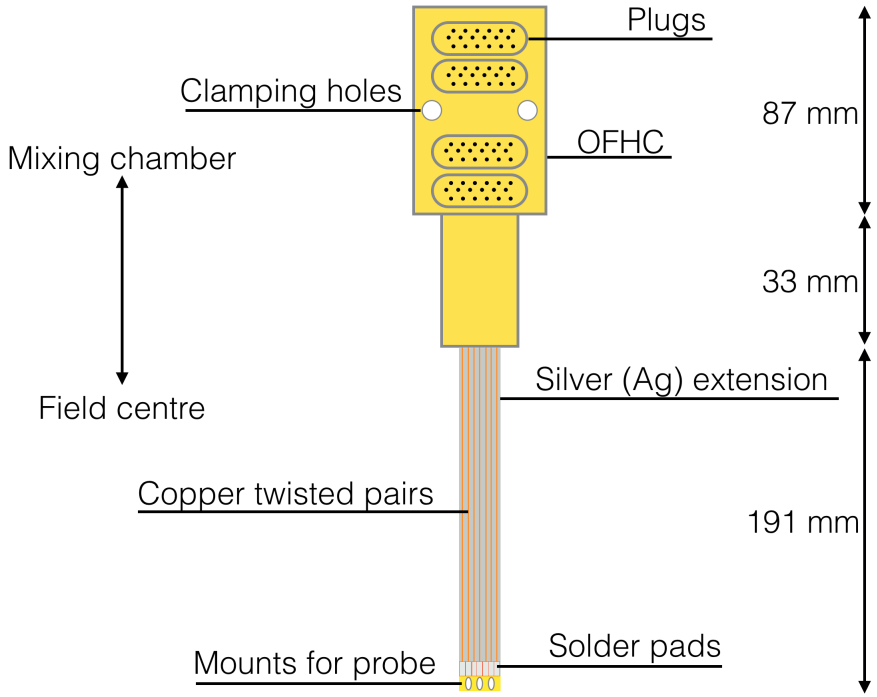

Figure 3.2 *Overview of the cold finger, coupling the mixing chamber to the sample probe. Details are given in the text.*

around 6%. This is shown in Figure 3.1, where the phase separation line falls downwards with temperature until it hits the concentration axis at $x = 0.06$. The reason for this non-zero fraction can be explained by the following: at small enough temperatures, being at the most 500 mK, the zero-point motion of the helium atoms becomes essentially coordinated - Van der Waals forces between the different isotopes favours some ^{3}He moving quickly between the slower-moving ^{4}He, justifying the continued presence of some ^{3}He. If a volume of pure ^{3}He is placed at a point such that the dilute mixture is between it and the pump, then by pumping to the point where $x \to 6\%$, the pure volume will start losing ^{3}He atoms to replenish the mixture. The ^{3}He expands, leading to the absorbtion of heat, defining the core cooling power. The name for this part of the fridge is the mixing chamber, and by coupling some system to this, one can achieve temperatures of the order of 20 mK. The mixing chamber is located 367.6 mm upwards from the field-centre of the magnet, being too large to fit in the space, and thus a "cold finger" is used to extend that cooling power down into the vicinity of the field; this is shown in Figure 3.2. The maximum field experienced by the mixing chamber is of the order of 100-200 Gauss, being less than 1% of the field inflicted upon the field-centre for greater than 1 T.

It is important to explain the material composition of the cold finger, as when temperature calibrations are done at finite values of magnetic field, the reference thermometer in this case is placed outside of the field centre at the top of the cold finger - thermal conductivity in this context must be significantly high. Thus, the main material present is silver, assumed high quality as supplied by the manufacturer, Cryogenics. The Additionally, oxygen free high conductivity (OFHC) copper makes up the two ends that couple to both the probe and the mixing chamber. The "top" end, as indicated in Figure 3.2, has four plugs, associated with four sockets, which are connected together manually while the fridge regulates at around 4 K. This is the main advantage of this design of fridge: one can decouple the sample probe from the mixing chamber, and extract without having to bring the fridge up to room temperature. The plugs act to both complete the circuitry with the outside, and press the cold finger to the mixing chamber with such pressure that thermally they can be considered one, or at least satisfy the zeroth law of thermodynamics. At the "bottom" end, OFHC probes used extensively in the lab for calibration and heat capacity measurements couple well to the cold finger with the use of three M3 screws with washers. All the copper twisted pair wiring up the cold finger is heat sunk on top of the silver - this minimises temperature gradients. Temperature gradients in wiring can lead to a lack of impedance matching, adding electrical resistance.

The magnet installed in the dilution fridge consists of an outer coil of Nb_3Sn, and an inner coil of NbTi, with a persistent switch capable of maintaining a persistent current high enough to create a field of 14 T. The mixture of the two Nb-based compounds helps increase the critical field of the whole magnet to above 12 T.

3.2 Design of Experimental Setup

As mentioned previously, the measurement of the specific heat of URhGe under high magnetic fields imposes a series of considerable requirements upon the design of the sample environment. On one hand, the importance of the perturbation in temperature applied purely to the sample leads to efforts being made to thermally separate the sample from the rest of the system. Kevlar wire, whose particularly useful properties are to be elaborated upon, becomes useful in this respect. On the other hand, the magnetic moment of the sample can couple with an external

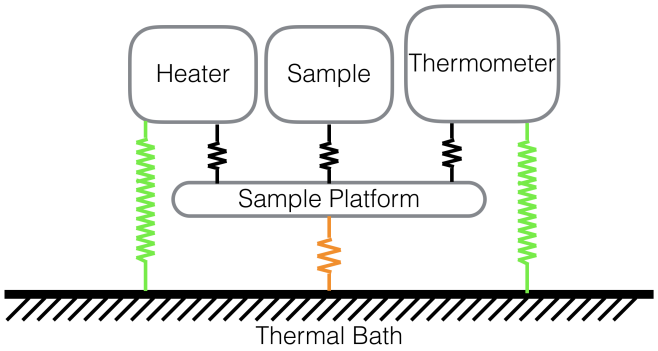

Figure 3.3 *A schematic of the thermodynamics relevant for heat flow throughout the sample, thermometer, heater, and thermal bath. The different coloured thermal resistances are explained in text.*

field, and if the orientation is right, can lead to the sample being ripped off the sample environment. In the following sections, these competing issues plus their attributed corollaries will be discussed, giving the motivation for the choice of particular design. This will be followed with a section displaying work done to estimate and test the effectiveness of the chosen design.

3.2.1 Probe & Addenda Overview

In chapter 2, the idealised situation for measuring the specific heat capacity of single crystals was elaborated upon. What was not described was the reality of what components are thermally coupled to what other components, directly and indirectly. The importance here is in the direct/indirect nature of those linkages, as they can be determined by a whole host of different materials with complex thermal behaviour, ultimately complicating any estimates one would want to do of the thermodynamics present.

In Figure 3.3 is shown a diagram depicting the relevant experimental situation. Firstly, the thermal links between the various components are shown: the green links between the heater and thermal bath, and thermometer and thermal bath, are realised with NbTi coils, supplied by Californian Fine Wire. Below $\sim$ 9 K, these coils are superconducting, and are thus very good thermal insulators below $T_c/10 \sim 0.9$ K - the electrical thermal transport is exponentially suppressed, but phonons still carry heat - rendering the green resistive links shown as thermally redundant. This is experimentally ideal, as any heat dissipated away from the heater to the sample will lead to inaccuracies in the measurements. The green links are thus thought of as being parasitic. The links between the sample

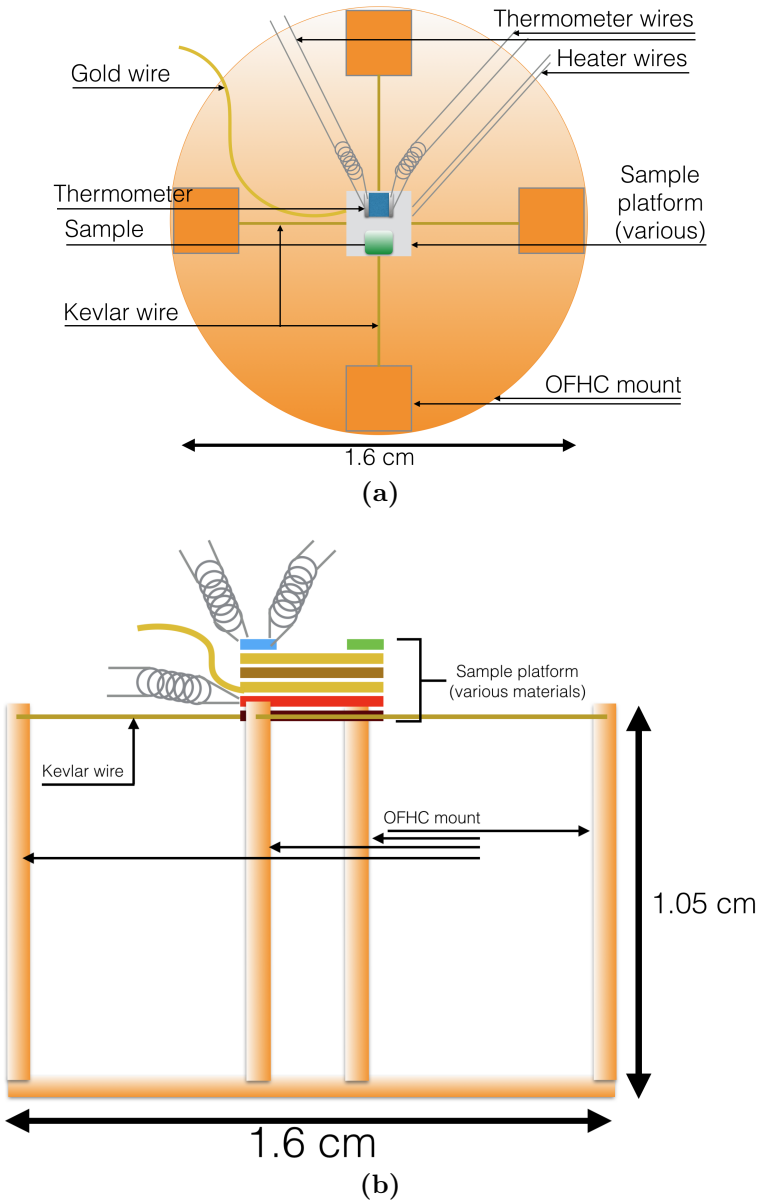

Figure 3.4 *Overview of the experimental setup. (a) and (b) a view from above and the side of the sample environment, showing both thermal and electrical links to the bath and beyond.*

platform and all other components (apart from the thermal bath), represented here with black links, are all realised with the use of silver (Ag) 6838 epoxy, supplied by DuPont. This being a composite of mostly silver brings a high level of thermal conductivity into the system, necessary to minimise systematic errors due to temperature instability. Finally, the gold-coloured link between sample platform and thermal bath is realised with a 25 μm diameter gold wire of length 15 mm. This is connected up in two different ways at either end, and those connections require some explanation; this is done in section 3.2.3. The tunable

nature of this link is important for setting the relaxation time to be of the right order of magnitude.

Figure 3.4a shows a diagram of how the probe looks when viewed from above, with the sample platform sat upon a crossed pair of Kevlar threads. These threads are glued with black stycast to OFHC copper rods, which stem from an OFHC base. When coupled strongly to the probe, the base and rods act as the thermal bath of the system. The dimensions of the rods are shown in better detail in Figure 3.4b. The heater is a thin-film strain gauge coupled to the bottom of the platform, and the thermometer a RuO_2 resistor coupled to the top. The whole stack of components are coupled to the Kevlar threads with GE varnish. Now, details on each of these components plus the methods chosen.

3.2.2 Sample Platform

The sample platform's design is based upon satisfying a few constraints. Firstly, it must have high thermal conductivity and low specific heat capacity. This allows thermal equilibrium, following a sudden temperature change from the switching on or off of a heater, to be reached on a time scale that is ideally an order of magnitude faster than the time scale of thermalisation between platform and bath, and for the heat capacity measurements to be from the sample more than any other components present. Secondly, the mechanical stability of the platform should be high enough for the device to be removed from the probe and replaced repeatedly, as is necessary for removing and attaching samples, and for continuous re-calibration. The reason for this comment is because in this study, a temperature calibration was performed for the thermometers before a full temperature-magnetic field calibration. Ideally one does the whole calibration in a single run, but due to the nature of this work, it was sensible to check the device in zero-field first, to see if the design satisfied the first few constraints. The final constraint involved mechanically stabilising the platform strongly enough to minimise rotation due to the torque between the magnetic moment and external field, but weak enough such that the thermal conductivity was low.

This last condition rules out standard methods of coupling the sample directly to a copper block, or to rest the sample upon superconducting wires. The design detailed here therefore involves suspending the platform upon a pair of Kevlar threads, each one consisting of between 20 and 30 filaments of diameter 17 μm.

(a) (b) (c)

Figure 3.5 *A view into the process of tensioning the Kevlar threads across a copper (Cu) device. Details are in the text.*

The manufacturers supply the wire in bundles of up to 150 filaments, so by reducing this by a factor of 10, there would be an equal effect upon the thermal conductivity. This is done under the microscope meticulously, separating out filaments to the point where between 20 and 30 remain; the difficulty in this lies in separating out wire 17 μm thick without intertwining them further. This comes at a price, in terms of the tensile strength of the total thread of filaments. Although the twisting of those filaments about one another can increase their strength, estimating the performance of this is near-impossible. Instead, a lower-bound for the tensile strength is found by assuming the filaments have no effect upon one another.

One final aspect to consider when using Kevlar wire is their negative thermal expansion coefficient [94]. When temperature is lowered, the Kevlar threads will grow in length by around 0.04%. As it has already been said, the tension of these wires must be high enough to resist motion due to the magnetic sample coupling with the external magnetic field. Thus, in order to combat this, the probe itself has been designed in such a way that the tension is maintained. In Figure 3.5a, the first step is shown in threading the Kevlar bundles through 0.5 mm holes in copper rods that protrude from a base of width 16 mm. These are manipulated easily by tying them around paper clips, requiring a bowline knot. Next, the copper base is placed into a device that allows the protruding rods to be bent inwards, by turning the four screws shown in Figure 3.5b. Finally, leaving the rods bent inwards, the Kevlar threads are glued in place using stycast, and finally

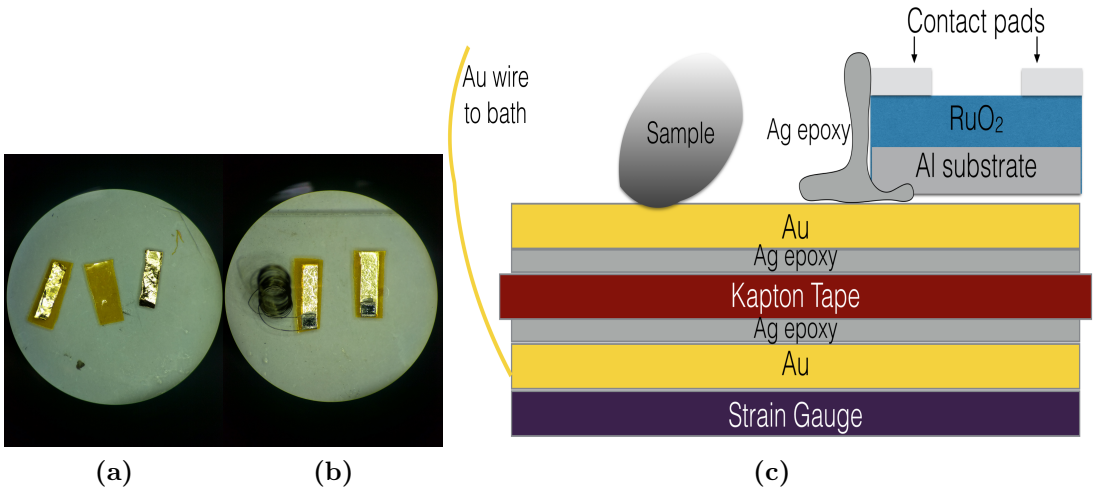

Figure 3.6 *(a) Two of the sample platforms in various stages of build; a deconstructed view, with Kapton tape and gold foil placed adjacent for size comparison. (b) The left-hand thermometer is almost complete, missing the second NbTi coil to be glued with silver epoxy to the contact pads on the RuO_2 thermometer. (c) A schematic of the sample platform, with all materials and configurations pointed out. The thickness of each layer is not to scale.*

released after 2 hours on a furnace at 180℃; this is shown in Figure 3.5c. The dimensions of the rods have been chosen such that no plastic limits of the copper are reached, and that the Kevlar threads are not pulled to the point of breaking. Details of a supporting calculation are shown in the appendix.

In Figure 3.6 the components present in the addenda: first, a layer of gold pure to 99.9% of dimensions 100 μm × 3 mm × 5 mm, and weight 1.84 mg. On top of this is a larger piece of kapton tape, thickness 30 μm and weight 0.51 mg. This insulates a second gold foil layer from the first. These three layers are all coupled through a process of applying a thin layer of silver epoxy 6838, compressing the stack flat with a glass microscope slide, and baking in that state for 2 hours at 180°C. This is done once per layer of epoxy added, totalling twice so far. The RuO_2 thermometer is then added, being carefully glued with the same epoxy in a way that one of the two contact pads are in both thermal and electrical contact to the top gold layer. The point of this is simple; by gluing one of the two contact pads to the foil, the thermal link between sample and thermometer is enhanced, rather than solely through the thermometer substrate. Finally, the contacts for the thermometer are glued in the same way to the contact pads, and a thin gold wire is spot-welded to the bottom layer of gold foil. This wire will lead to the

probe, and thus the kapton tape isolates the thermometer and sample from the thermal bath.

3.2.3 Tunable Thermal Link

The main drivers for the choice of heat link are to set the time constant for the heat capacity measurement. The longer it is the better the temperature at each point can be measured, but on the other hand, this slows down the measurements. A longer time constant also limits the minimum temperature that can be obtained owing to the parasitic heating from the environment.

In order to gain the right order of magnitude of τ, the relaxation time, the sample should be heated above the base temperature by an amount ΔT that is a significant number of multiples of the standard deviation, σ_T, of the base temperature. This produces an exponential rise / fall of temperature, which to fit an exponential to is more successful. In the dilution refrigerator used, σ_T does change with temperature, but as a rough estimate, between 30 mK and 600 mK one can acheive a σ_T as small as 0.1 mK. Thus, this proposes an appropriate ΔT of at least 1 mK. The source of the noise at such teperatures can be attributable to a number of physical origins; one is Johnson-Nyquist noise [95], where the power generated by this noise is of the form $P = k_B T \Delta f$, where k_B is the Boltzmann constant, and Δf is the bandwidth of the lock-in amplifier. For a bandwidth of between 2 and 5 Hz, this produces around 10^{-24} Watts of power. For a resistor of tens of $k\Omega$, this corresponds to 0.1 nV, and the voltage induced during thermometery at temperatures below say 200 mK are of the order of tens of μV, proving the negligibiility of the Johnson-Nyquist noise. Thus, the source of this random error, σ_T, will be in the thermal instability of the mixing chamber itself, and temperature variations due to the probe heater abiding by the PID function[1].

Upon this reliance of ΔT are the dimensions of the thermal link decided. A gold wire of a diameter thin and length long enough is used; the maximum length of wire is calculated below for dispersing the irradiation heat only. At that point, the upper bound on this length will be known.

[1]This stands for Proportional Integral Differential, defining a thermostat. With a given target of temperature (setpoint), the amount of current supplied to the heater is varied over time. A Lakeshore 370 resistance bridge is utilised for this purpose.

In order to find this length, a model is proposed that utilises the relevant low-temperature properties of gold [96]. Initially the power transferred due to thermal flow is modelled as

$$\dot{Q} = \Delta T \times \frac{1}{R_{th}} \tag{3.1}$$

One problem here is that the thermal resistivity, R_{th}, is not known to high enough accuracy at temperatures below 1 K. The electrical resistivity R_{el}, however, is, following a linear temperature dependence from $\rho = 2.44 \times 10^{-8}$ Ωm at 20°C to of the order of one hundredth of that at 1 K. In order to link the latter to the former, the Wiedemann-Franz law is utilised. This observable trend sees a strong relationship between the electrical and thermal resistivity of a large host of materials and elements, the ratio of the two tending towards a constant as $T \to 0$. Formulated, it states

$$L_0 = \frac{K}{\sigma T} = \frac{R_{el}}{R_{th}} \frac{1}{T} \tag{3.2}$$

$$\therefore \dot{Q} = \Delta T \times \frac{T L_0}{R_{el}} \tag{3.3}$$

where L_0 is the Lorenz number, a constant. Now, the resistance encountered by any heat flowing between sample platform and the thermal bath will come from both the wire, and additionally the connections made between wire and the two systems: a spot-weld to the sample platform, and a mechanical clamping to the bath. The spot-weld is considered the only connection that has some finite electrical resistance, estimated from experience to be of the order of 1 mΩ.

$$\therefore R_{el} = R_{sp-W} + \frac{\rho L}{A} \tag{3.4}$$

$$\therefore \dot{Q} = \frac{T \Delta T L_0}{R_{sp-W} + \frac{\rho L}{A}} \tag{3.5}$$

To see if this system is appropriate for the heating necessary to measure heat capacity effectively, some values are tested. The square wave sent to the strain gauge is chosen to be of size 200 nA - this was seen to produce a ΔT of 3-5 mK - diameter of gold wire 25 μm, and $T\Delta T = 0.2 \times 0.003$ K^2. This gives a required length of 2.905 m, but this is specifically an *upper bound* - anything longer than this will struggle to conduct the same amount of heat energy away. Here, a length of wire 15 mm long is used, sufficiently dispersing the heat from the addenda. This was chosen due to the physical restraints of the system dimensions, where anything longer than 15 mm would be practically difficult to implement. Every sharp bend and slight deformation will reduce the RRR, and these are inevitable

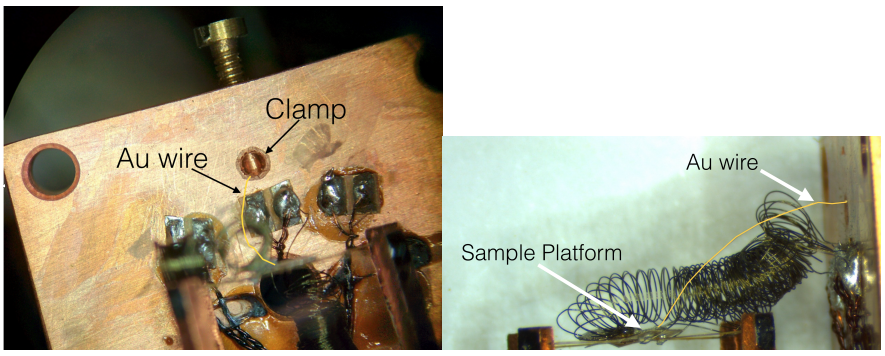

(a) (b)

Figure 3.7 *The gold wire thermally coupling the sample platform to the bath is shown - highlighted with a gold coloured line for clarity. (a) and (b) show the situation from two different angles, capturing the full length of the wire from mechanical clamp to spot-weld.*

in the manipulation of said wire during setup of the experimental situation.

Alternative sources of heating

In addition to the the above, heating can come from the radioactivity of the uranium. The amount this produces is calculated to be small, being around 70 pW for 22.08 mg of URhGe. This is easily conducted away with the gold wire indicated previously. The cooling power of the fridge and the heating power of the sample heater also contribute to masking the effects of radioactive heating. Although there are no figures to support the following, the performance of the 15 mm wire was found to be proficient, thermalising the addenda with a relaxation time of $\sim$ 10 s. Changes could be made to the length if more heating power had to be applied to the sample, as was found at higher temperatures.

3.2.4 Thermometer

Absolutely essential to this work is the knowledge of what the temperature of the sample is. Due to the extreme requirements of the type of measurement - thermal exclusion, mechanical stability - this requests that the thermometer used must be small in shape and mass, and functioning over a large range of temperatures and magnetic fields.

The experimental setup used here includes the use of Lakeshore RuO_2 resistance

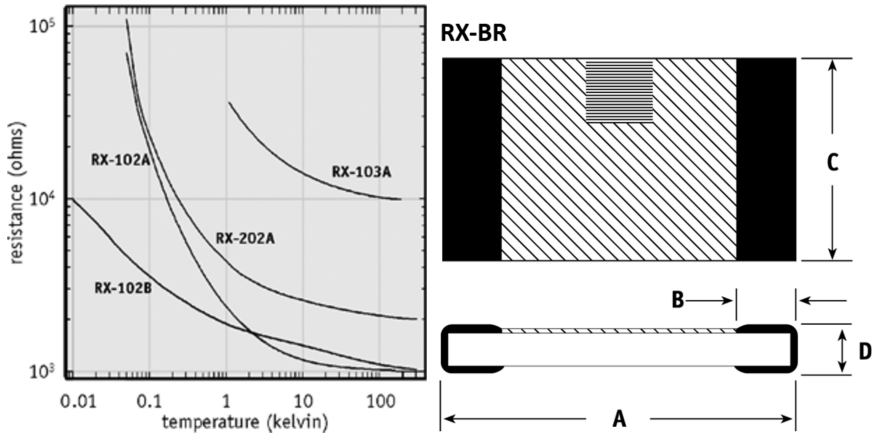

Figure 3.8 *(a) The typical temperature dependence of the electrical resistance for the whole host of chip thermometers provided by Lakeshore. The chosen RX102A chip was to balance cost with effective sensitivity at low temperatures. (b) A schematic of the RuO_2 chip thermometers, with A = 1.45 mm, B = 0.3 mm, C = 1.27 mm, and D ≈0.08 mm, polished down from the original height of 0.67 mm.*

chips, model RX-102A. They can be described as a metal-ceramic composite, being a mixture of conductive RuO_2 and Bi_2RuO_2 embedded in a lead silicate glass matrix. This is all deposited on an aluminium substrate and heated above its glass point, to bond the composite together. The physics behind the sharp rise in sensitivity between electrical resistance and temperature lies in conduction electrons hopping across the RuO_2-glass matrix. This hopping is thermally activated, thus reducing conduction as temperature is lowered.

In terms of the way the chip is connected, Figure 3.6c shows a schematic of how, where silver epoxy 6838 glues the chip to the top layer of gold foil. Two NbTi coils of length 40 cm are also glued with the same epoxy to the contact pads, being made of palladium silver; solder is another option for a secure connection, but the heat involved can destroy the RuO_2 calibration. This connection is mechanically secure, requiring no extra substance like stycast or otherwise. Details on the calibration of these thermometers can be found in section 3.3.2. Additionally, the aluminium oxide substrate that the thickness of the thermometer is mostly taken up by was polished down from 0.67 mm to 0.08 mm, to both minimise the contribution it can give in heat capacity, and the thermal insulation it provides.

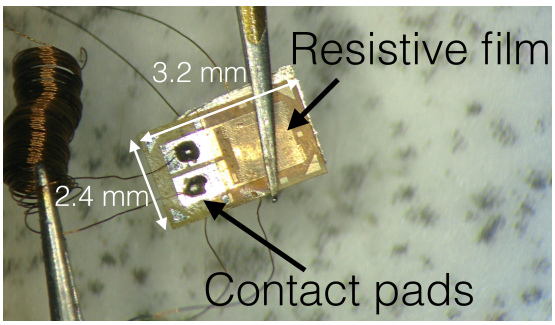

(a)

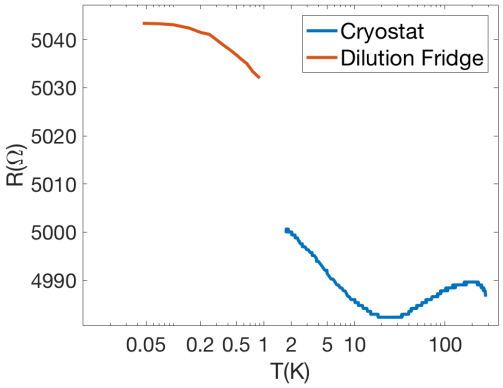

(b)

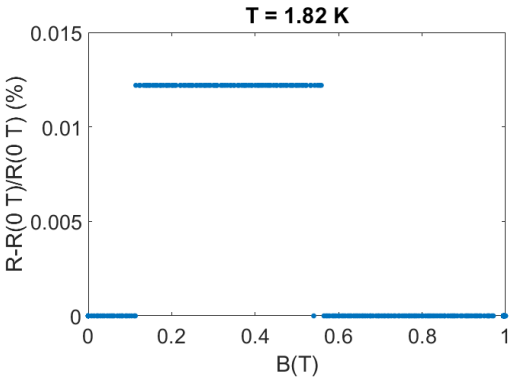

(c)

Figure 3.9 *(a) The size of a strain gauge being soldered onto is shown, with specific components pointed out; details in the text. The change in resistance of the strain gauge as (b) temperature is varied between 50 mK to 300 K, and (c) magnetic field is varied between 0 T and 1 T, $T = 1.82$ K. The flat reading is due to the signal being at the limit of the sensitivity of the lock-in amplifier.*

3.2.5 Heater

The component responsible for providing the heat, prompting a response and therefore information, is the heater. This is realised by a sensor device called a Strain Gauge, being a thin film polyimide backing hosting a resistive element NiCr alloy film of 5 KΩ electrical resistance. An epoxy film covers the resistive element for protection. These are cheap, reusable, and highly malleable, making them ideal for such an experiment with the potential for high levels of mechanical strain. The device must align to the same restrictions as the thermometer, being small in mass and size, and having a known behaviour across the relevant temperature and magnetic field scale.

A benefit of strain gauges is their insensitivity of electrical resistance over a

large range of temperature and magnetic field. The latter is shown in Figure 3.9b, where the resistance of the same strain gauge was measured as temperature varied from the base temperature of the dilution fridge up to room temperature, with a gap between corresponding to the zone where there's no overlap between the dilution fridge and conventional ^{4}He cryostat used. As for its performance under field, as shown in Figure 3.9c, the relative change in resistance for a field of 1 T applied parallel to the device was no more than 0.02%, proving its versatility in such extremes.

The electrical connections to the solder pads are, in this case, gold. A single NbTi twisted pair coil is connected up this way, ensuring a superconducting channel blocks heat flow to the thermal bath. In the way using solder on the RuO_2 has the potential to do chemical damage, this is not the case for the strain gauge, as the only part vulnerable to heat damage is the resin base, and this contributes minimally to heat flow. Thus, the solder will contribute to the addenda's heat capacity. The solder used is 60/40 Sn/Pb, which goes superconducting below 7.8 K, but once an external magnetic field of greater than 0.2 T is applied, the substance can be brought into its normal phase and have a more significant contribution.

3.2.6 Estimates of Thermal Performance

What follows is a series of results for estimations of the heat capacity and thermal conductivity of the addenda. Due to gaps in the literature, what is presented is not absolute quantitative data on every single component used, but rather guides for the rough order of magnitudes plus their variations with temperature and magnetic field. In the appendix is Table D.1, listing the specific values found for the various measurable quantities.

Addenda Heat Capacity

Previous measurements of the heat capacity of the majority of materials used have been made, referenced accordingly. This is shown in Figure 3.10. The data shows C/T, rather than C, such that it is easily comparable with sample data shown in later sections, where any data that was given either per mole or per gram has been scaled relative to the amount of material present within the setup here. However, some leniency is required, especially when it comes to those materials made up of an unknown mixture of elements; the 2.4 mg RuO2 thermometer

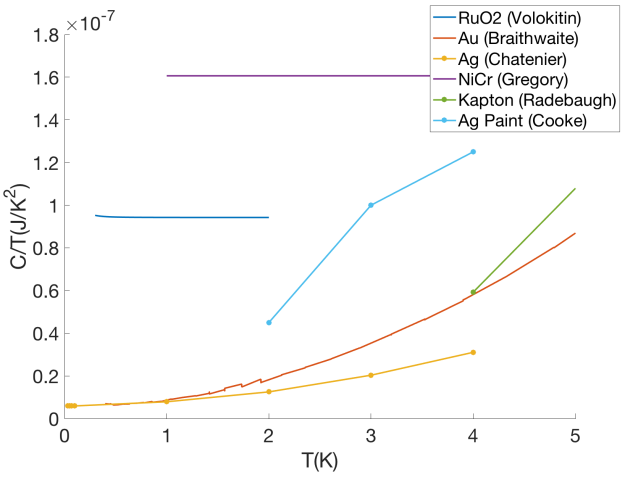

Figure 3.10 *Literature values of specific heat capacity for each of the components of the addenda, converted into the units J/K^2 to help with comparison with data taken.*

used in the setup here consists, as previously mentioned, of a thin film of RuO_2, a reduced thickness of Al_2O_3, and solder pads of PdAg. In this case, because the literature for RuO_2 was measured per mole, the mass of PdAg relative to RuO_2 is small, and also the molar mass of Al_2O_3 as compared to RuO_2 is small, then the estimation for the heat capacity of the device uses just the molar mass present for 2.4 mg of RuO_2. Similar estimates are done for the strain gauge, using the molar mass of 2.54 mg of NiCr and ignoring the polyimide base in which it sits.

The component that gives the largest contribution is the NiCr element in the strain gauge. References [97] and [98] show heat capacity measurements on strain gauges, albeit of different resistive elements. For the former, NiCr is measured from 2 K to 30 K, showing a trend of $C/T = a + bT^2$. The latter measures the alloy constantan between 50 mK and 1 K. Although a temperature dependence of $C/T \propto 1/T^3$ is found, no specifics of the coefficients are given. Whether NiCr shares this temperature dependence at low temperatures is shown in section 3.4.2.

The next largest is the RuO_2 thermometer. This has been shown to display a broad peak around 0.3 - 0.4 K [99], where heat capacity measurements were made on a range of thermometer types. The origin of this peak is thought to be due to some magnetic impurities found in the aluminium substrate. This would be proportional to mass, so polishing down the substrate is akin to cutting down the size of this peak.

Next, for an estimate of the gold signature, unpublished data by D. Braithwaite of the ILL, Grenoble, for calibrating a PPMS device was kindly lent for this work;

the heat capacity of a 14.7 mg sample of gold was measured from 30 K down to 0.4 K, and thus the heat capacity data is known in both J/K as well as J/mol.K.

For silver epoxy, the heat capacity was measured [100] between 3 & 30 K. As compared to pure silver, as measured by Chatenier and de Nobel [101], the paint gives a larger reading, assuming to be due to the additional bonding agent used, here being Hexyl Acetate, and Thylene Glycol Monoethyl Ether Acetate in the literature. To find the mass of epoxy present, one can take the mass of all the components individually, then find the difference between the sum of those values, and the weight of the completed addenda. This measurement has not been made, so an estimate of the order of 1 mg is carried forward.

The weights measured for each component, and thus the total addenda, are as follows:

$$\begin{aligned} \text{Sample Platform Weight} &= \text{Au foil} + \text{Kapton tape} + \text{RuO}_2 \\ &+ \text{Strain gauge} + \text{Ag epoxy} \\ &\approx (1.84 \times 2) + 0.51 + 2.45 + 2.54 + (1 \pm 0.05)\ \text{mg} \\ &\approx 10.18 \pm 0.05\ \text{mg} \end{aligned} \tag{3.6}$$

Thermal Conductivity

Estimates on the thermal link between addenda and bath are extremely useful in knowing if the heat capacity measurements will be possible within a given experimental parameter range. There are three types of material acting as a thermal bridge between the two systems, and each will be detailed.

First of all, there are 2 lengths of Kevlar wire, each of which consists of 25 (averaged) individual fibres, that couple the addenda to the bath. Each fibre is 17 μm in diameter, and 15 mm in length. The thermal conductivity of Kevlar has been measured before by G. Ventura *et al.* [94] to follow, for the temperature range 0.1-2.5 K:

$$\kappa_{Kevlar}(T) = 3.9 \times 10^{-5} T^{1.17}\ \text{W/cm.K} \tag{3.7}$$

Second, the already-referred to gold wire in section 3.2.3 has been measured before to find the thermal conductivity; one can use the Widemann-Franz law, resulting

in the following:

$$\kappa_{Au}(T) = \frac{L_0}{\rho}T \tag{3.8}$$
$$= 1.1091 \times T \text{ W/cm.K} \tag{3.9}$$

Even if the conductivity is reduced by a factor of 10^5 through wire deformation, this is still significantly higher than that for Kevlar, and also for kapton. The thermal conductivity of kapton tape was measured by Barucci *et al.* [102] from 5 K down to 200 mK. The thermal conductivity here was measured to follow a fit of the form

$$\kappa_{kapton}(T) = 6.5 \times 10^{-5} T^{1\pm0.02} \text{ W/cm.K} \tag{3.10}$$

The thermal conductivity expected for the electrical connections to the thermometer and heater is of the order of zero, or at the most, negligible, due to them being NbTi superconducting wire with an insulating heavy polyimide coating, composition 48% Nb, 52% Ti, and diameter 5 μm. Their conductivity being zero is carried forward.

Finally, the electrical contacts should be considered, being of the order of 1-10 mΩ. One can utilise the Wiedemann-Franz law to estimate the thermal conductivity, taking forward the assumption of the geometric factor being $A/L = 0.1 \text{ mm}^2/0.1 \text{ mm} = 0.1 \text{ mm}$:

$$\kappa_c(T) = \frac{L_0}{\rho}T$$
$$= 10^{-2}\frac{2.44 \times 10^{-8}}{5 \text{ m}\Omega \times 0.1 \text{ mm}}T \text{ W/cm.K}$$
$$= 4.88 \times 10^{-4} T \text{ W/cm.K} \tag{3.11}$$

This is appropriately larger than the conductivity for the non-metallic substances.

For the silver epoxy that links most of the layers together, as well as the NbTi coils to the thermometer, an estimate of mass present is difficult due to the lack of a mass measurement. Additionally, how silver epoxy 4929 acquires its adhesive property is by mixing with a solution of Hexyl Acetate, in proportions 10:1 respectively. The mixing procedure, which takes place on a glass slide and with a cocktail stick as the stirrer, will never be perfect in producing a completely homogenous epoxy. Additionally, the epoxy type that requires baking, silver epoxy 6838, will achieve an equally unpredictable level of homogeneity due to

the heat from the hot plate not necessarily being uniformly spread. A form of this type of silver epoxy was measured [103], giving a thermal conductivity of 0.03 W/m.K just above 3 K. This is comparable with the values for the electrical contacts, but still a few orders of magnitude smaller than that for gold.

Thus, the total thermal conductance of the link to the thermal bath, which due to the parallel-like nature of the components is a simple sum, is found to be:

$$\begin{aligned}
\kappa &= \sum_{components,i} \kappa_i \frac{A_i}{L_i} \\
&= \left(2 \times 25 \times \kappa_{Kevlar} \frac{\pi(17 \times 10^{-6})^2}{15 \times 10^{-3}}\right) + \left(\kappa_{Au} \frac{\pi(25 \times 10^{-6})^2}{15 \times 10^{-3}}\right) \\
&+ (\kappa_{kapton} A_{kapton}/L_{kapton}) + \left(\kappa_c \times 1 \times 10^{-4}\right) \qquad (3.12) \\
&= 1.1802(9) \times 10^{-12} + 1.4518(1) \times 10^{-5} \text{ W/K} \\
&= 1.4518(1) \times 10^{-5} \text{ W/K at 1 K} \qquad (3.13)
\end{aligned}$$

The gold wire is the most contributive factor, by a factor of 10^7, so care must be taken with the treatment of the wire in the experimental setup. It is likely that a 25 μm diameter wire can become slightly misshapen through manipulation, especially when inserting the free-end of the wire into the hole into which it is mechanically clamped to the probe. Each bend can decrease the mean-free path of the conductive electrons, thus leading to a drop in the thermal conductivity. Thus, this estimated value is treated as an upper-bound, especially so due to the temperature assumed. This conductance is expected to follow $\kappa \propto T$, and as shown in section 3.4.2 this is a reasonable assumption.

Relaxation Time Finally, the time taken for the addenda to cool back down to the bath from some given heat input can be estimated by combining the heat capacity and thermal conductance.

$$\tau = \frac{C_{addenda} + C_{sample}}{\kappa} \qquad (3.14)$$

With an estimated $C_{addenda}$ of $2{\times}10^{-4}$ mJ/K^2, and the Fermi liquid value of the heat capacity C_{URhGe} of $1{\times}10^{-3}$ mJ/K^2, then the relaxation time will be significantly different enough for the signal-noise ratio to be at least 5. Thus far, the estimated theoretical values of this setup have been discussed. Now the experimental realisation of these quantities will be shown, starting with how thermometry is executed.

3.3 Thermometry

Key to the goal of exploring the novel phases of unconventional superconductors is knowing what the temperature is accurately. Here the use of a RuO_2 based film resistance chip for thermometry is chosen, their properties having been discussed in the previous section. Now, firstly the known electrical properties will be discussed, and then the calibrations completed will be shown. Many of the methods used in experimental techniques stem from what is advised in [95].

3.3.1 Resistance Thermometers

The type of thermometers used here are considered to be *secondary thermometers*. *Primary thermometers* are those whose physical properties are guaranteed to correspond to a temperature with minimal uncertainty, without the need for a calibration; for example, gas thermometers that use the ideal gas laws relating temperature, pressure, and volume. However, their sensitivity is generally lower than what can be achieved with *secondary thermometers*. These do require calibration, as their composition can change from one to another, but their sensitivity is generally higher than their primary counterparts at the temperatures relevant for the studies reported here [92].

RuO_2 chips have been in use in this field for over 20 years. Their main advantage is the huge rise in resistance as temperature is lowered, increasing the sensitivity. This is shown in Figure 3.11a for two of the thermometers used in this work, labelled thermometers F and G. Additionally, the log-log plot of resistance verses temperature shows the sensitivity of the thermometer, formulated as $d(lnR)/d(lnT)$; a constant gradient implies that the sensitivity is consistent throughout the temperature range. This is seen, in Figure 3.11b, and the deviation at low temperature between the two thermometers shows just how important it is to calibrate for an individual device.

The calibration was performed over a temperature range defined by the reference thermometers used, being of the order of 50 mK to 1 K[2]. This range was split into three ranges, each of which was fit to Chebyshev polynomials of degree 7.

[2]The thermometers were not calibrated to 40 K, the highest temperature in the ref. thermometers calibration, due to temperatures above 1 K being irrelevant for the this study.

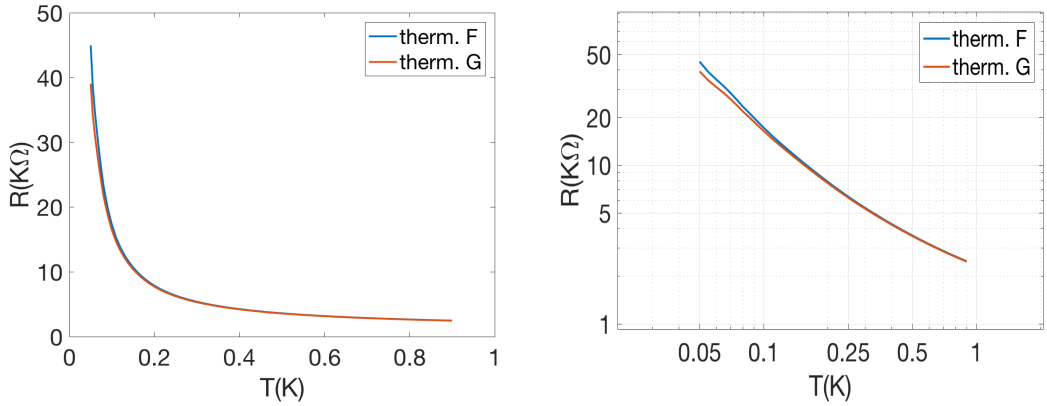

Figure 3.11 *The electrical resistance of two of the thermometers used, as a function of temperature, from 50 mK to 900 mK, plus the log-log plot of the same data.*

These have the form:

$$T = \sum_{i=0}^{i=7} A_i \cos(i \arccos(X)) \tag{3.15}$$

$$\text{where } X = \frac{(\log_{10}(R) - \log_{10}(R_{low})) - (\log_{10}(R_{high}) - \log_{10}(R))}{\log_{10}(R_{high}) - \log_{10}(R_{low})} \tag{3.16}$$

and R is the resistance measured ($R_{low/high}$ is the minimum/maximum of that span of measurements), and A_i are the coefficients. A set of these are provided by Lakeshore, acting as a rough guide for determining the temperature, but the calibration process' main goal is to determine those coefficients to high enough accuracy such that one can consider the thermometer characterised.

In zero field, a Chebyshev polynomial of order 7 was fit to the temperature vs. resistance data. The advantages with this come from the presence of a cosine in equation 3.15, which requires that the each term making up this series will not be greater than the coefficient of that term, allowing truncation easily.

3.3.2 Calibration

Having now described the resistive properties of RuO_2 thermometer chips, the process of calibration is now detailed. Two chips were characterised in total, both acquired from Lakeshore.

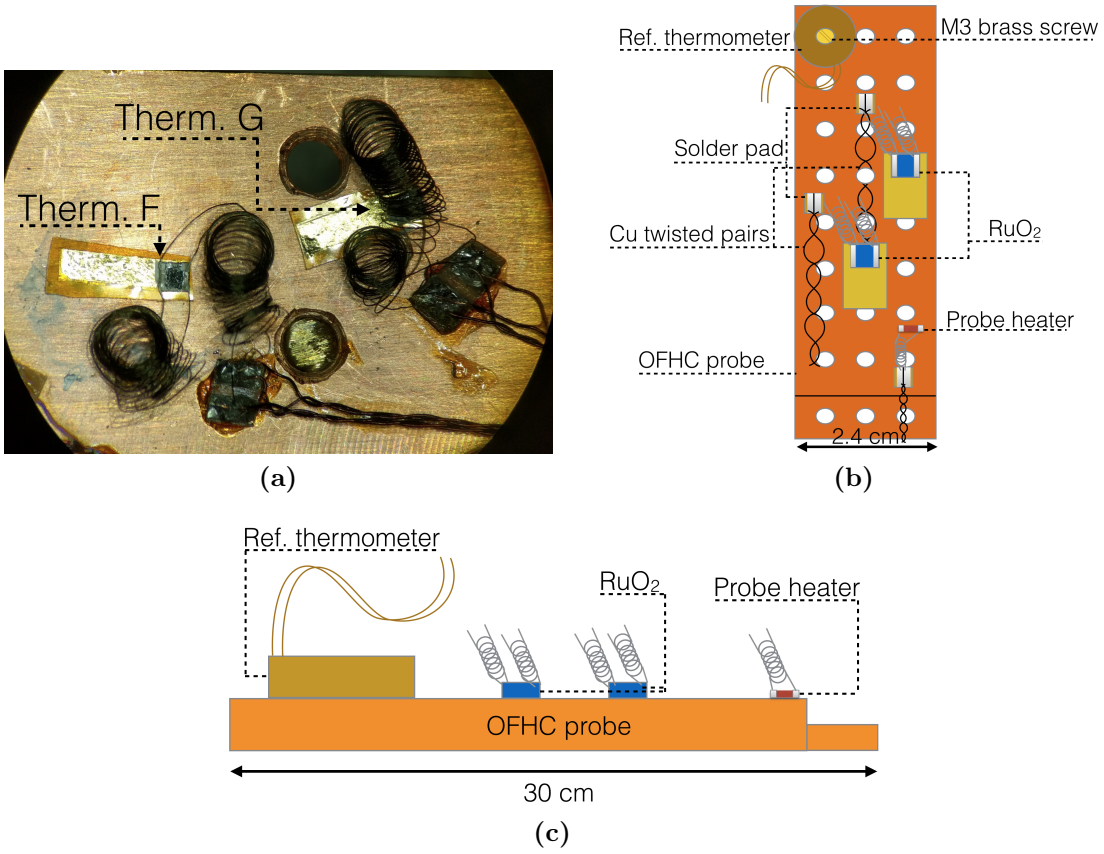

Figure 3.12 *The thermometers' arrangement on the calibration probe are shown, together with a schematic from (b) above and (c) the side. The reference thermometer is a Lakeshore RX-102A-CB, useful from 45 mK to 40 K. The heater is a 10 KΩ film resistor, powered by a Lakeshore 370 resistance bridge.*

Low Temperature Calibration Probe - Zero Field

In order to effectively calibrate multiple thermometers, a custom probe was made. This is a simple 30 cm × 2.4 cm × 0.5 cm block of OFHC, with multiple 3 mm threaded holes such that many devices can be attached and calibrated simultaneously. This is shown in Figure 3.12.

The two uncalibrated thermometers are coupled strongly to the base, and electrical connections are made via heat-sunk copper twisted pairs that lead from the probe to the cold finger. These meet the thermometers in a equally-well-coupled solder pad, into which the NbTi coils from the RuO_2 also go. The coupling is done with silver epoxy 4929, which requires 30 minutes of pressure until it is set; this is done using a vice with significant amounts of cushioning

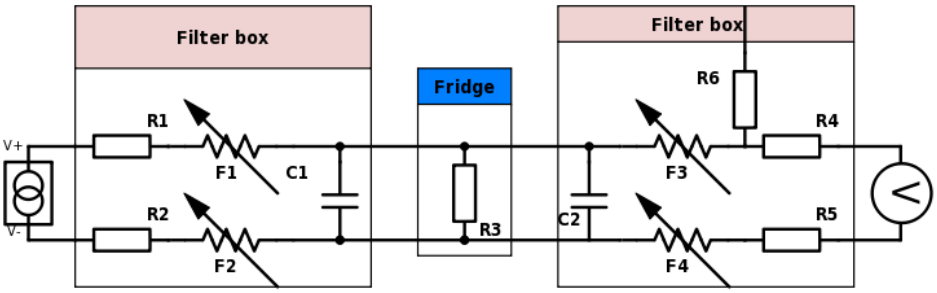

Figure 3.13 *The electric circuit used for both heat capacity measurements and thermometer calibration. The values of R1 to R6 are INSERT respectively, and C1 and C2 are both 1 pF. The radio-frequency inductors have an inductance of INSERT, creating an LC circuit that filters out MHz electrical signals. The current source, both filter boxes, and lock-in amp. are outside the cryostat at room temperature.*

via the use of teflon tape. Effort must be given to establishing this coupling, due to the possibility of a small internal thermal relaxation leading to significant systematic errors.

The circuitry involved is shown in Figure 3.13. Here, a current source that is outside of the fridge passes an AC current through an in-house-built high-frequency noise filter, onwards to the breakout box that leads the signal to the thermometer inside the fridge. More details on the need for the filter are given in section 3.3.2. Here, a four-probe setup (done so with two NbTi coils) allows the voltage induced across the thermometer to be measured, excluding the connections that lead to and from it [95]. The voltage is measured via one of the NbTi coil that connects back up to the outside of the fridge, through a second high-frequency filter box, and into a lock-in amplifier. The current source is a Keithley 6221, and the lock-in amp. is a Stanford Research 7265; these are used throughout the whole series of experiments detailed in this thesis. The current source triggers the lock-in amp. via the TTL input, allowing signal comparison between the two.

High Frequency Noise

High-frequency noise is an issue that can be a significant obstacle in measuring electrical resistance with AC circuitry. With an excitation current driven by

a frequency too high, Joule heating can occur, rendering the measured signals untrustworthy. To understand this, thermometer design prototypes will be briefly discussed. In total, 5 previous designs for the thermometer and addenda were built over the course of the PhD. The measurements from those devices showed significant errors in their accuracy; as the lock-in amplifier measures both the X (in-phase) and Y (out-of-phase) signals relative to the input from the current source, then observing the Y signal to be more than 10-20% of the X signal is generally a sign of bad circuitry.

The problem with those devices is that the location of the four-probe connections are not directly onto the thermometer - the voltage across both the RuO_2 and the two NbTi coils is being measured. Given high-temperature stability, especially below the critical temperature of NbTi, their coil-like state may lead to some inductance, manifesting in this case as extra electrical resistance.

The electrical resistance calculated from X- and Y-signals picked up by the lock-in amplifier is ideally insensitive to amplitude and frequency respectively, for fixed temperature. Thus, for all thermometers built, a test upon their sensitivity to such parameters is made. This is shown in Figure 3.14 for the thermometer labelled Thermometer F. A 3-axis plot shows the voltage signal's temperature and parameter dependence (parameter is either amplitude or frequency of excitation current). These readings were taken at 3 K, 400 mK, 50 mK, and 30 mK, over the amplitude range 5 nA - 16 nA in 1 nA steps, and a frequency sweep from 37.5 Hz up to 237.5 Hz in 10 Hz steps, making sure to not match the UK mains frequency of 50 Hz. Both plots show the full sweep of both parameters, where in Figure 3.14a, there is a spread of readings along the voltage axis; each different coloured line is a different value of frequency. For Figure 3.14b, the case is the same but for amplitude.

What is expected is, for the amplitude dependence, Ohm's law. This describes a linear dependence of voltage upon amplitude. The voltage units are dB, and so this linear dependence is transformed into a logarithmic trend. For the frequency dependence, the voltage is expected to be flat, assuming there is no impedance, in the form of capacitance or inductance present. Whether these two expectations are fulfilled or not are detailed below. It should be noted that -3 dB is considered to be an appropriate cut-off point, corresponding to half the power output.

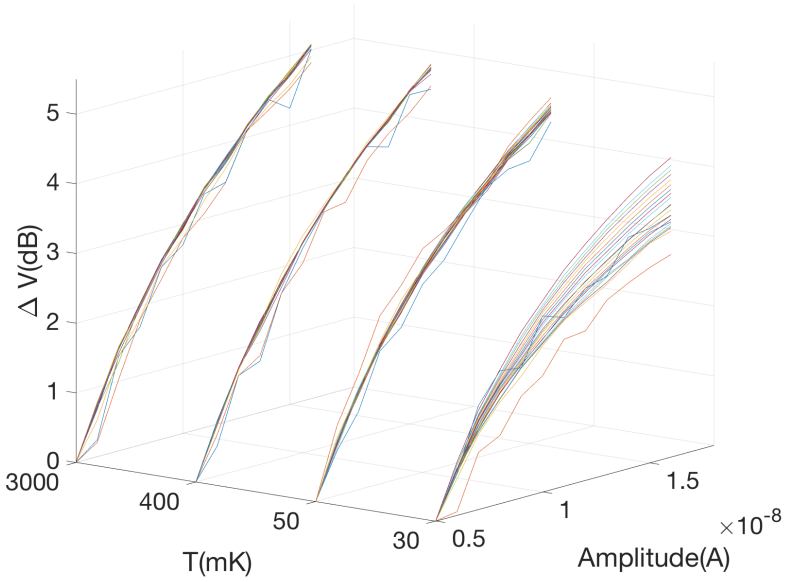

(a)

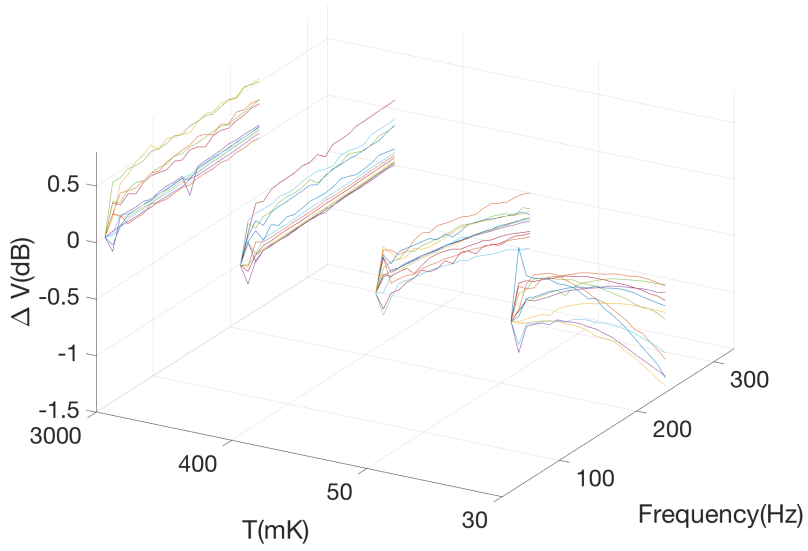

(b)

Figure 3.14 *Two plots show the amplitude (top) and frequency (bottom) dependence, as well as the temperature dependence of the voltage read by the lock-in amplifier. Different colours within the plots indicate different values of the non-labelled parameter i.e. the frequency spread in the top plot, and amplitude in the bottom. Degradation of the signal begins below 50 mK.*

First, there is little difference between the readings at 3 K and 400 mK, both in amplitude and frequency dependence. A continuation of insensitivity to these

parameters is in line with Lakeshore documentation on RuO_2 chips, and is supportive of the lack of contribution from the addenda.

Between 400 mK and 50 mK, the frequency dependence starts to take effect around 150-200 Hz, especially for the lower values of amplitude. In the amplitude dependence, the spread increases somewhat, but not enough for the dB values of voltage to indicate a serious change of behaviour. Thus, for this temperature range, amplitudes between 5 nA and 16 nA and frequencies between 77 and 137 Hz are chosen as being appropriate.

Finally, for 50 mK to 30 mK, changes start to occur. The frequency dependence is strong enough to suppress the voltage signal by up to -1.5 dB for the lowest amplitudes, whereas the higher amplitudes induce a voltage that is suppressed by just over -0.5 dB. Ohm's Law is still obeyed by the majority of the frequency readings, but this frequency dependence opens up a weakness in the design. One possible weakness is the thermal coupling between thermometer and addenda, bringing in an internal oscillation that can appear as low-frequency noise in the voltage signal, coupling to the range of frequencies applied. Another more likely cause is the effect of capacitance at such high resistances: the thermometers' resistance at such temperatures is in the region of 50 KΩ. Thus, some effective impedance due to said capacitance, which has an inversely proportional relationship to frequency, will become visible. The resultant systematic error evident in these frequency and amplitude plots is left as a minor effect, observable only at the very limits of temperatures measured here. An appropriate amplitude and frequency for the whole temperature range was chosen to be 8 nA[3] and 113.3 Hz or 137.7 Hz, one for each of the two thermometers being calibrated.

Calibration Procedure

Thus far, the obstacles with AC circuitry have been discussed, focussing on the importance of knowing what the effect of current source parameters is upon the voltage induced across the thermometers. This leads to an understanding of what temperatures can be probed accurately, and more importantly, which temperatures cannot. Now, the process of relating the resistance of the thermometer to temperature is discussed, and in due course the effects upon those resistance values from applying an external magnetic field.

[3]This is 8 nA peak, such that the actual applied current is the RMS value of $8/\sqrt{2}$ nA.

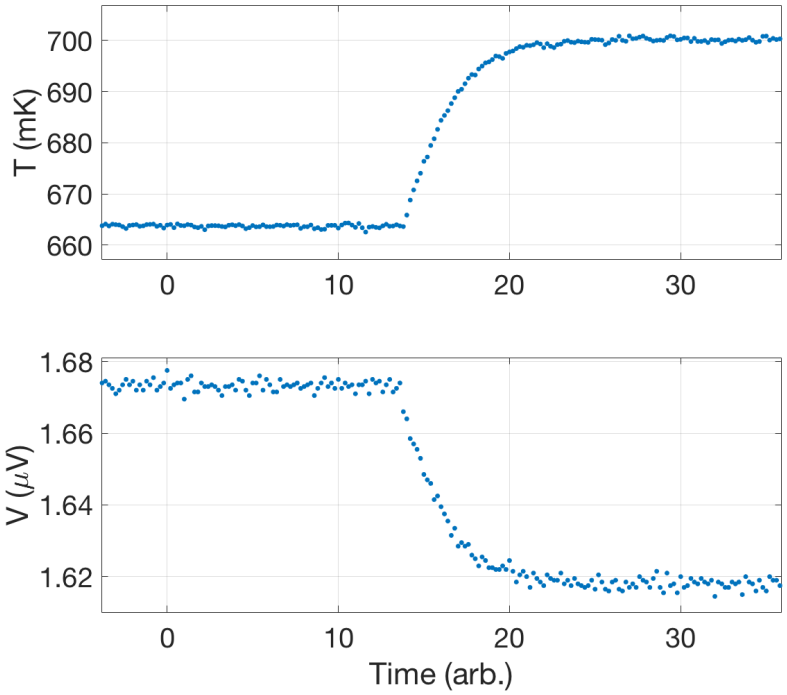

Figure 3.15 *The reaction of an uncalibrated thermometer, excited with current 8 nA, to a change in set point of the calibrated reference thermometer. The matching time scale of thermalisation indicates that there is no systematic thermal insulation between the two.*

Shown in Figure 3.15 is one of the temperature steps, that of which is repeated over the whole temperature range. A probe heater - a 10 $k\Omega$ resistor - is given a set point at time $t = 0$. This is 700 mK in this example, being in the higher range of temperatures probed in this thesis. The amount of time taken for the reference thermometer to reach the set point matches that of the uncalibrated thermometer, represented here by the X-signal voltage reading. This indicates the thermal coupling between the two is high, ruling out any significant thermal resistance at this temperature. Once both devices have stabilised relative to the changes due to the set point, the range of stability is averaged over, the mean and standard deviation of which is chosen as a single data point and error bar in the resistance versus temperature plot shown in Figure 3.11a. The points are spaced out non-linearly, with temperature steps being 4 mK between 50 mK and 100 mK, 10 mK between 100 mK and 300 mK, 20 mK between 300 mK and 500 mK, and 40 mK between 500 mK and 900 mK, resulting in 52 data points[4]. Over

[4]Lakeshore provide a calibration over roughly half the number of data points.

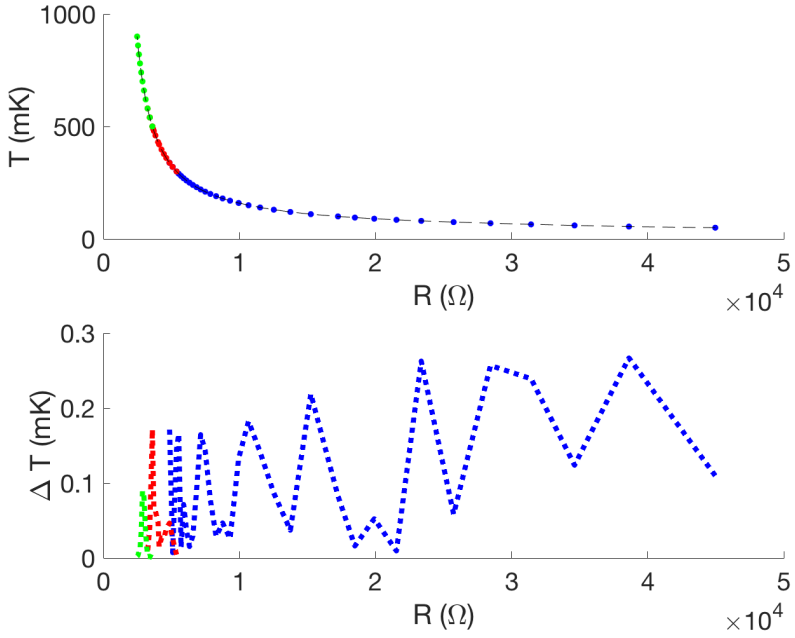

Figure 3.16 *The fits over the three temperature ranges are shown, with the residuals given in mK. Given that all temperatures are at least 50 mK, this gives a maximum error smaller than 0.1%.*

the whole temperature region, the current source sent 8 nA to both thermometer F at 113.7 Hz, and thermometer G at 137.7 Hz. The results of fitting Chebyshev polynomials to the data are shown in Figure 3.16, where overlap in the regions over which different calibrations are done help keep the continuity in the values of resistance that are converted to temperature.

3.3.3 Magnetoresistance

The performance of these thermometers under a range of temperatures allows probing of one part of the phase diagram of the investigated materials, and so in order to probe the other axis, the effects of external magnetic field must be found. Previous work [104] showed a field-dependence of the form $R \propto B^{0.5}$ for fields above 2 T, and at lower fields a negative relative change of electrical resistance. Here, similar results were observed, allowing measurements to continue without significant design changes.

Compared to the experimental set-up for temperature-calibration, there were

no major differences for this setup, other than making sure the thermometers are placed as close to the field centre as possible. The more certainty there is of the field inflicted upon the thermometers, the more accurate one can be in position on the phase diagram. In practice, the deviations from the real field felt by the thermometers can be a systematic error, potentially adjustable from comparing to previous data. The thermometers were thus placed at the following positions, given as coordinates relative to the field centre: thermometer F (6,-2), thermometer G (4,-3), units are mm, and the coordinate system is (radial,axial), and positive/negative refers to vertically upwards/downwards. These two positions give a relative difference from 14 T of 99.87% and 99.99% respectively, and so these fractions of the true field are applied throughout.

The magnetic field was swept from 0 T to 14 T in 0.5 T steps, with thermalisation time given for each field value due to the heating from induced eddy currents in the circuitry. Three of these steps, while the system is regulated at 285 mK, are shown in Figure 3.17; the blue line is the response signal from one of the thermometers, and the orange line is the value of the magnetic field. The eventual range of values that the thermometer saturates to are taken as the voltages characteristic of those external conditions, with a data point defined here as the mean-average of that range of the data.

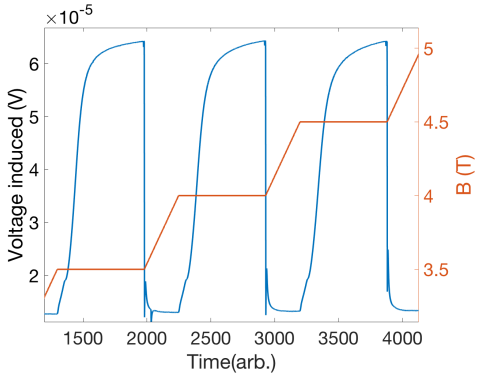

Figure 3.17 *An example of three steps in the calibration procedure; the voltage (blue) of the RuO_2 thermometer changes with field (orange).*

In Figure 3.18 is the full collection of data taken, interpolated over a finer set of temperature and magnetic field values, for one of the two thermometers calibrated. Also shown is the relative errors in fitting to $B^{1/2}$, with a maximum of around 3%. The largest deviations occur at the highest temperatures, where the initial dip expected at low temperatures is non-existent (as shown in Figure 3.19), and so the square-root trend of magnetic field has strong origins in the significant rise of resistance above $B = 1$ T.

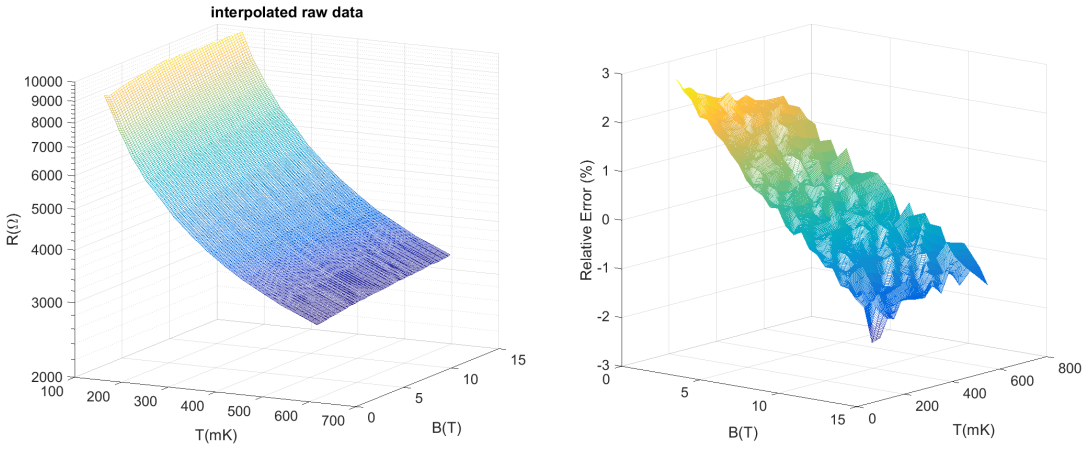

(a) (b)

Figure 3.18 *(a) A surface is interpolated between the data points taken, over a grid of temperature steps 2 mK and field steps of 1.25 T. (b) The relative error in fitting $R = R_0 + R_1 B^{1/2}$ to the interpolated data.*

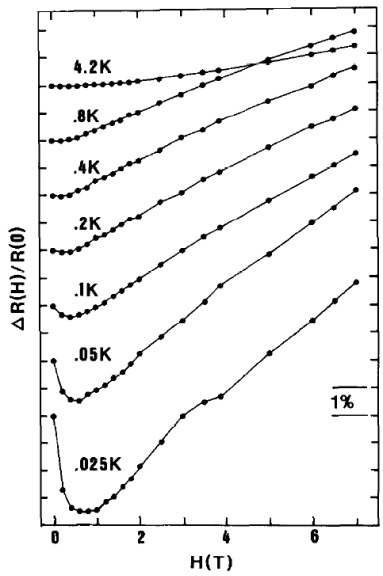

Figure 3.19 *Literature data of the resistance across a RuO_2 chip changes with temperature and field, with the curves offset for clarity [105].*

3.4 Characterisation Run

3.4.1 Heat Capacity of UPt_3

In Figure 3.21, the heat capacity measured for UPt_3 is shown. The sample used is of high quality, originating from a batch of high quality crystals grown

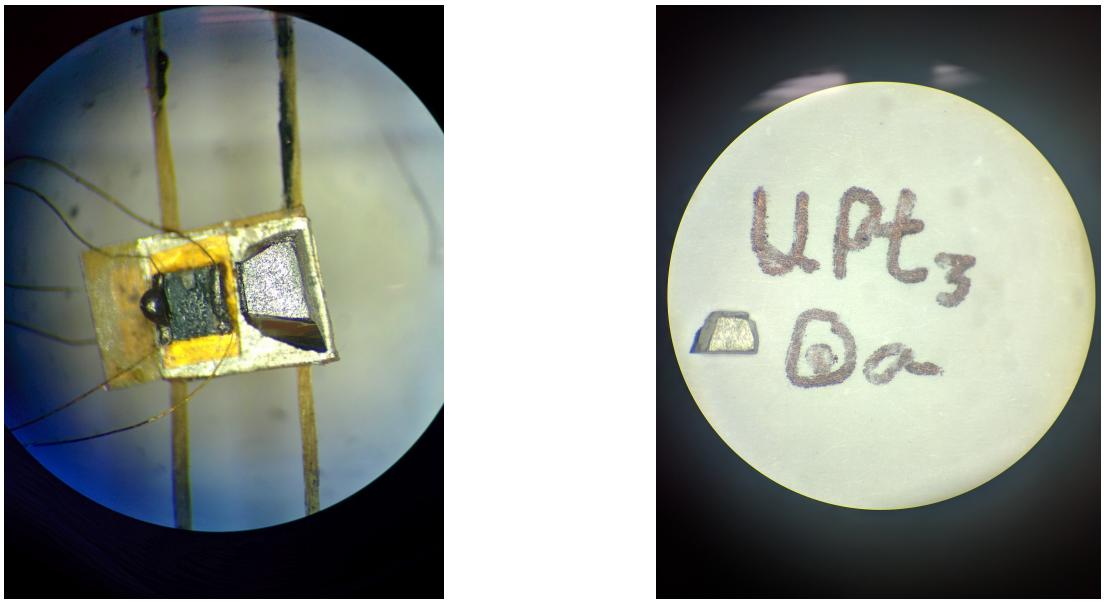

(a) (b)

Figure 3.20 *(a) The sample of UPt_3 used is attached to the addenda, mounted upon a pair of Kevlar wires. The RuO_2 used is to the left of the sample. (b) The sample is shown, where the hexagonal planes defined as being normal to the table top.*

previously by A. Huxley; the sample is shown in Figure 3.20. This material shows two distinct discontinuous changes in C/T, corresponding to the presence of a modulated phase which can be suppressed with external field. Previous work done [106, 107] on this material shows the two temperatures, T_c^- and T_c^+, to be 480 mK and 550 mK. Above T_c^+, the Sommerfeld coefficient γ is 440 mJ/mol.K^2, one of the largest in the heavy fermion family. Below T_c^-, a temperature dependence of $C/T \propto T$ is measured, corresponding to line nodes [36]. The size of the jump, $\Delta C/T$, in this case equal to 80 mJ/mol.K^2 and 160 mJ/mol.K^2 for T_c^- and T_c^+ respectively, is also indicative of the fact that the heavy quasiparticles present at these conditions are responsible for these transitions. Additionally, the sharpness of the transitions indicates that it is not a smeared-out transition, which could be true for a inhomogenous sample split into superconducting and non-superconducting parts.

The critical temperatures measured were $T_c^- = 465$ mK and $T_c^+ = 530$ mK, being roughly 4% lower than the literature values [107], also shown in Figure 3.21. The value of the Sommerfeld coefficient above T_c^+ is closer to 400 mJ/mol.K^2, and the jumps ΔC are approximately 160 mJ/mol.K^2 and 80 mJ/mol.K^2, and the same Schottky anomaly is seen at the lowest temperatures. Each of these are discussed

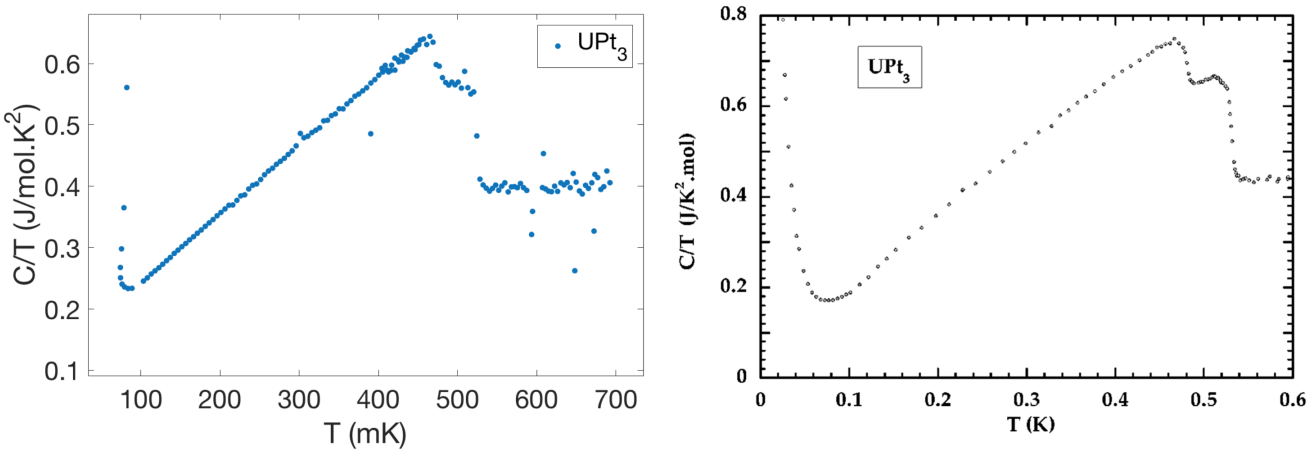

Figure 3.21 *Heat capacity divided by temperature as a function of temperature for both measurements performed by the author, and performed by [107], displaying both the separate phases, and the $C/T \propto T$ below ~480 mK.*

below.

For the temperature measured at the jumps in heat capacity to be lower in magnitude, this would mean the resistance across the thermometer is higher. This is found to be true in another property: $T_c^+ - T_c^-$ is invariably fixed across multiple samples and measurements [36]. For an ideal value of 70 mK, here the difference is 65 mK. Additionally, the transition width is generally sharp, being of the order of $T_c/100$; here, widths of 10 mK and 8 mK are found, being double the tolerance stated. A culprit for this can be found in the current source used. In these measurements, an Agilent B2962A was found, below 10 nA, to be delivering a noisy current across the thermometery. This resulted in an increase in resistance measured across the thermometer, accounting for part of the mismatching critical temperatures.

For the lower γ, this can be attributed to the duration of heating - if the heater is switched off before the thermometer has fully thermalised, then the value of thermal conductivity calculated is lower than ideal, being proportional to the temperature difference caused by the heater. This would cause the whole dataset to be shifted down, the amount being dependent on the time the heater is on.
The jumps in heat capacity are equal to those from literature, indicating the relative contribution from heavy quasiparticles being constant. Finally, the presence of the Schottky anomaly is across both measurements, establishing the continued presence of a low-degeneracy multi-level system.

As previously mentioned, the set-up used here has not been used again due to disintegration. This is a common occurrence, due to the sensitivity of the components to extremes in heat, and mechanical pressure. Thus, what was taken forward was the design of the thermometer, and the specifics of the methods i.e how much power the sample heater delivered, but what was to be added were design aspects that make the device less destructible. What these are are detailed in the corresponding results chapters that follow.

3.4.2 Heat Capacity of the Addenda

Here the measurements done upon the addenda with no sample, focussing on the magnitude of heat capacity in units of J/K, rather than per mole or kilogram, are detailed. A temperature sweep from 50 mK up to 900 mK was implemented, allowing the amount of heat supplied by the heater to change accordingly with the size of the noise in the addenda thermometer. As it was for the thermometer calibrations, the excitation current sent to the thermometer was 8 nA. However, for the higher temperatures, that amplitude was increased up to 20 nA. The prospect of added noise due to heating from the applied current is only relevant below 100 mK; one can be more liberal with amplitude above.

In Figure 3.22, the values found for the heat capacity and thermal conductivity are shown as a function of temperature. The noteworthy features are as follows. First, the low temperature heat capacity diverges while cooling, which was expected due to magnetic impurities present in the aluminium substrate of the RuO_2 thermometers, as well as both the NiCr and the anomolous film in the strain gauge. Second, the heat capacity becomes insensitive to temperature as it increases. Third, in the thermal conductivity data, a general linear dependence on temperature is followed, as expected from the gold wire linking the addenda to the bath, obeying the Wiedemann-Franz law. The intercept is found to be positive, reinforcing the dominance of the gold present in the thermal path.

For a direct comparison with separate material components, Figure 3.22a shows the contribution of gold, emphasising the dominance of that component. The data for gold came from PPMS calibration measurements performed by D. Braithwaite. Concerning the rest of the addenda present, it is thought that the RuO_2, Kapton tape, and NiCr of strain gauge fill the gap in heat capacity magnitude, especially

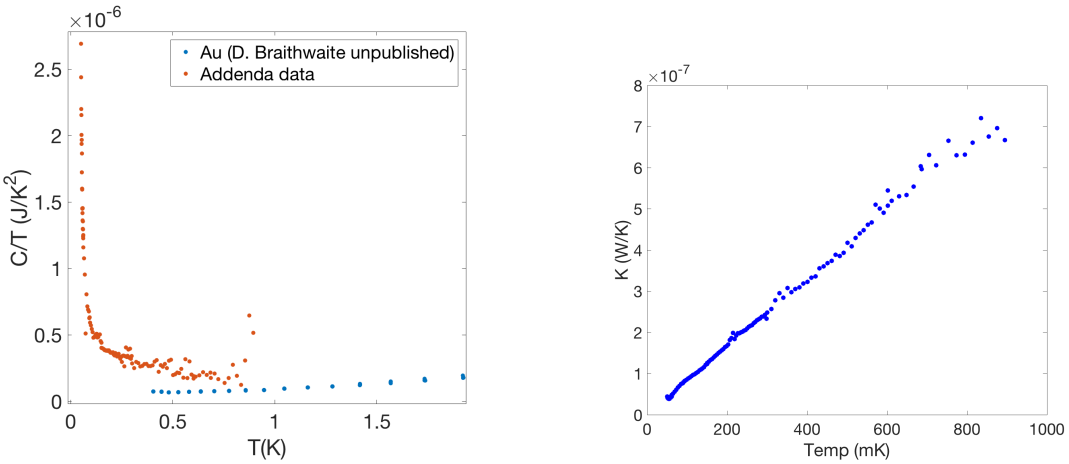

Figure 3.22 *(a) The heat capacity divided by temperature of the addenda with no sample, as a function of temperature. Also shown is the heat capacity of gold, measured by D. Braithwaite of the ILL, Grenoble. (b) From the same measurement, the thermal conductivity of the addenda-bath link as a function of temperature.*

the low temperature rise; magnetic impurities in the substrate of the RuO_2, the unmapped heat capacity of NiCr at low temperatures, and anomolous epoxies present are assigned responsible for this.

To account for the behaviour shown, a fit is made. In section 3.2.6 it is made clear that the NiCr present in the strain gauge should give the largest contribution, obeying a temperature dependence of the following [97]: a fit of $C/T = a + bT^2$ to the data without the low-temperature peak results in $a = 2.96 \times 10^{-7}$ J/K^2 and $b = -7.82 \times 10^{-8}$ J/K^4. If, however, a fit to the whole dataset is made of the form $C/T = a + bT^{-3}$, then $a = 2.86 \times 10^{-7}$ J/K^{-2}, and $b = 2.44 \times 10^{-10}$ J. These are both shown in Figure 3.23, in green and red respectively. The latter, adhering more to the low temperature data, is expected for a strain gauge made of constantan [98]. Thus, assuming the strain gauge is the largest contributor to the heat capacity, then NiCr is thought to follow constantan in temperature dependence.

Whether or not this addenda is small can be clarified by comparing the magnitude of the heat capacity with that taken for UPt_3. In units of J/K, the heat capacity from 50 mK to 600 mK spans 2→4 μJ/K^2, whereas for the addenda one can see the values are between 0.5→2 μJ/K^2, atleast half the magnitude over the same temperature range. This establishes a small but subtractable background to be

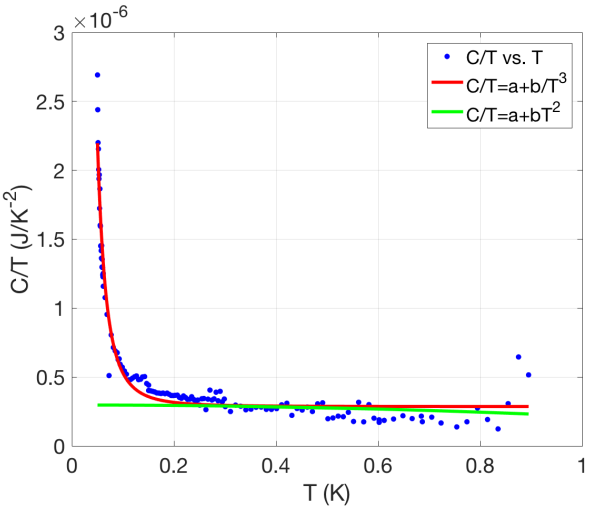

Figure 3.23 *Two fits applied are shown for the temperature dependence of the heat capacity divided by temperature. The dependence shown in red is that expected for constantan, and that in green for silicon and gold. More details are in the text.*

taken off the following heat capacity measurements.

Chapter 4

Results: Heat Capacity of UAu_2

In this chapter, results are shown for heat capacity and resistivity measurements performed upon a single crystal of UAu_2. This is to determine whether there are any low-temperature phase transitions, and to see the full extent of the already-measured non-Fermi-liquid phase. The reason for both types of measurement was to provide more conclusivity on phenomena occurring at a particular temperature, and for comparison with previous samples measured by colleagues. First the heat capacity measurements are described, followed by resistivity.

There are already some data on the heat capacity of UAu_2, over the temperature range of around 350 mK - 50 K [5]. The lack of heat capacity data below 350 mK was due to the limitations of the device used, being a Physical Properties Measurement Device (PPMS), built by Quantum Design, and so the puck built here is considered ideal to cover the temperature range accessible by the dilution fridge.

Inferred from both measurements are a few different phases of matter, all occurring below the Neél temperature, 43.5 K. The heat capacity is sensitive to all changes of the free energy of a system, and so magnetic phase transitions, cross-over periods between different phases, and a Fermi-liquid transition should all be visible. The Neél transition is already established to be visible in the heat capacity, as shown in Figure 4.1, as is a magnetic transition at a much lower temperature of 420 mK. However, as opposed to that described here, the sample used in the measurements reported in this thesis was annealed, reducing crystallographic disorder to allow the emergent magnetic structure to stand out.

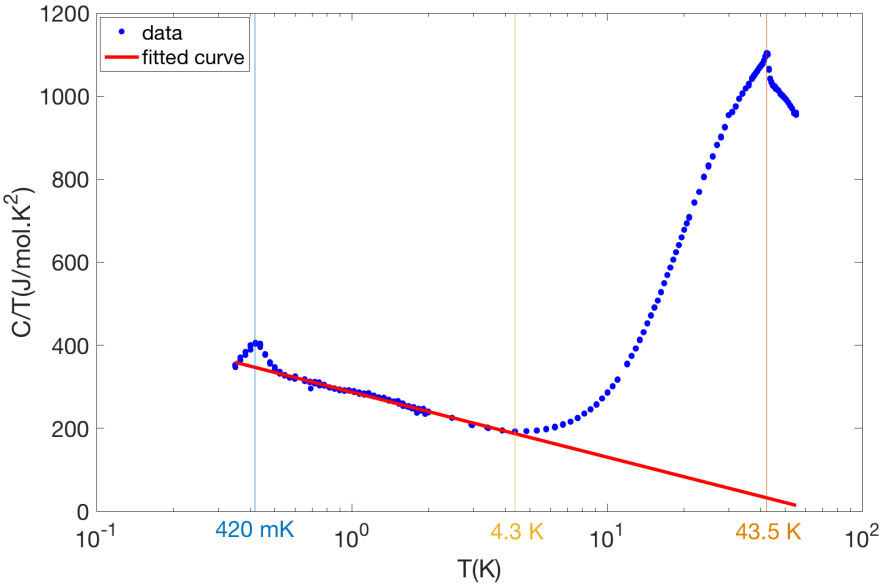

Figure 4.1 *Temperature dependence of the heat capacity divided by temperature of an annealed sample of UAu_2, displaying the key transitions, cross-over periods, and a fit related to quantum oscillations, on a logarithmic scale in temperature.*

Also shown in Figure 4.1 is a fit of the form $C/T = \gamma' \ln(T^*/T)$. This, as explained in section 1.3.1, is a form for the heat capacity in a non Fermi liquid phase. The modified Sommerfeld coefficient, γ', is present, as is the temperature indicative of spin fluctuations, T^*. For this fit, those values are $\gamma' = 66.28$ mJ/mol.K^2, and $T^* = 75.31$ K. The implications of these values will be more relevant when the full data set is shown.

4.1 Heat Capacity Results

Shown in Figure 4.2 in the left-hand plot is the heat capacity measured in the dilution fridge in blue, as well as that taken beforehand in the PPMS. The measured values of relaxation time and thermal conductivity are shown in the right-hand plots. There are a few important details to raise with reference to these two separately measured quantities.

First, the thermal conductivity was measured from 80 mK to 600 mK, by the method detailed in section 2.1. It is noticeably unstable at the extremes of those

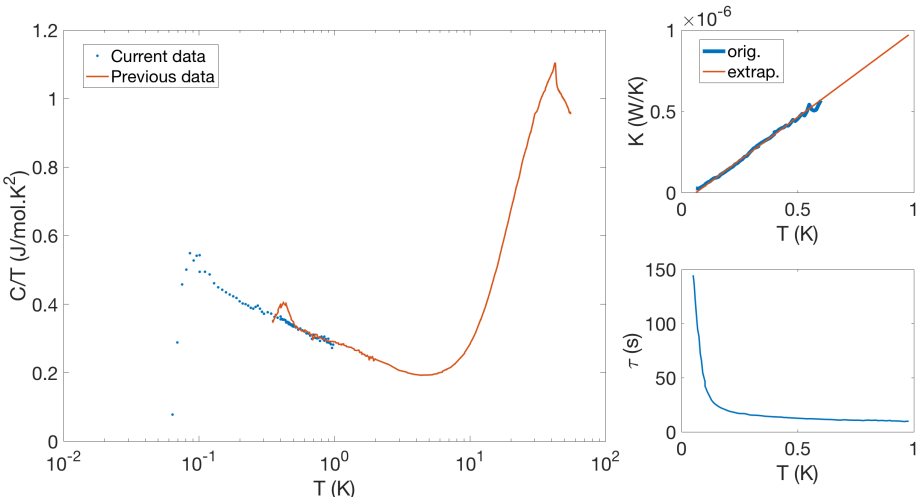

Figure 4.2 *Left: Both the previous data taken by the PPMS, and the data taken presently, plotted over a logarithmic temperature scale. The downturn of C/T is explained in the text. Right: the thermal conductivity and relaxation time measured, with fit details given in the text.*

temperature ranges, because the effect of the heater at those extremes was weak. The ΔT inflicted was too small to see an effective cooling from which K can be calculated. The heater in this case was the RuO_2 thermometer, rather than the strain gauge, to maximise the amount of power passing through the sample; problems with using the thermometer as a heater simultaneously are detailed below in section 2.2.

The relaxation time was measured over the full range of 46 mK to 1 K, using the strain gauge as a heater. Generally, because K is a property of the total coupling between sample and bath, then τ is much more reflective of the sample properties, and thus any expected jumps or discontinuities would be visible in τ too. Here, a steady increase of τ with lowering temperature is maintained from 1 K to just below 110 mK, at which point an upturn occurs. What this reflects is an increase in the heat capacity, which for a material displaying quantum oscillations, can be suggestive of a magnetic transition approaching. Whether that transition is seen here or not is dependent on the extrapolation performed on K. The reason for the extrapolation is because of the different temperature ranges measured across for τ and K. To combine the two sets of data, they must be taken at the same temperatures. To extrapolate, a linear function $K = \alpha T + \beta$ was fitted to a section of the K data, not including the low-and-high ends due to temperature instability. This fit is shown in Figure 4.2, and clearly has a negative intercept

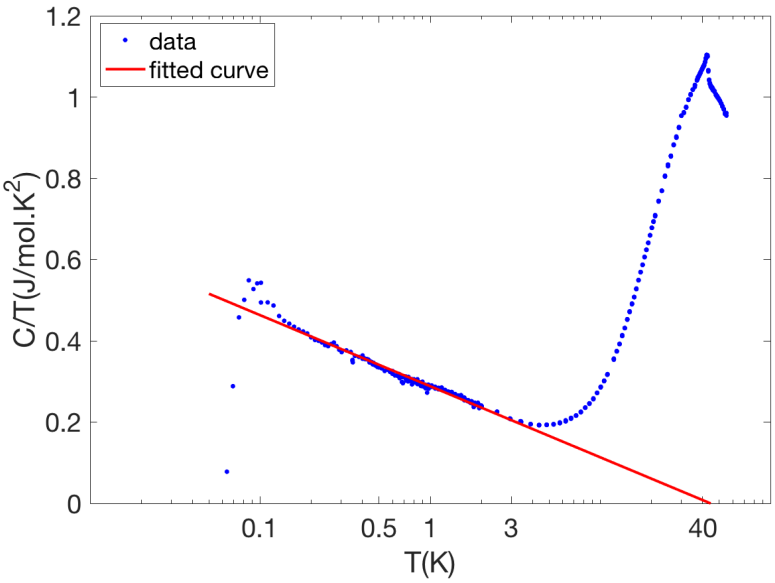

Figure 4.3 *The temperature dependence of the heat capacity with the non Fermi-liquid fit shown, fit to the range 100 mK to 3 K. Results of this fit, plus a fit to different temperature ranges, are explained in the text. Note that the transition around 420 mK has been removed, to allow the possibility of the novel behaviour continuing beyond the transition.*

value, $\beta \sim -6.5 \times 10^{-8} W/K$, and so is taken as not physical below 100 mK. Some aspects of the data below 100 mK are discussed in the analysis section, for completeness, but generally the data is not treated as representative of the sample.

4.1.1 Non Fermi-liquid fit

Temp. range	γ' **(mJ/mol.K^2)**	**T* (K)**
∼129 mK - 3 K	73.50	50.37
∼500 mK - 3 K	66.28	75.31

Table 4.1 *Results of fitting to two different temperature ranges, where γ' is the modified Sommerfeld coef., and T^* is the temperature at which spin fluctuations begin.*

Shown in Figure 4.3 is a fit to the data of the form $C/T = \gamma' \ln(T^*/T)$. As described in section 1.3.1, the origin of the fit is from an AFM system with quantum fluctuations, contributing to the entropy of the system. The full range of temperature over which the heat capacity seems to follow a logarithmic change

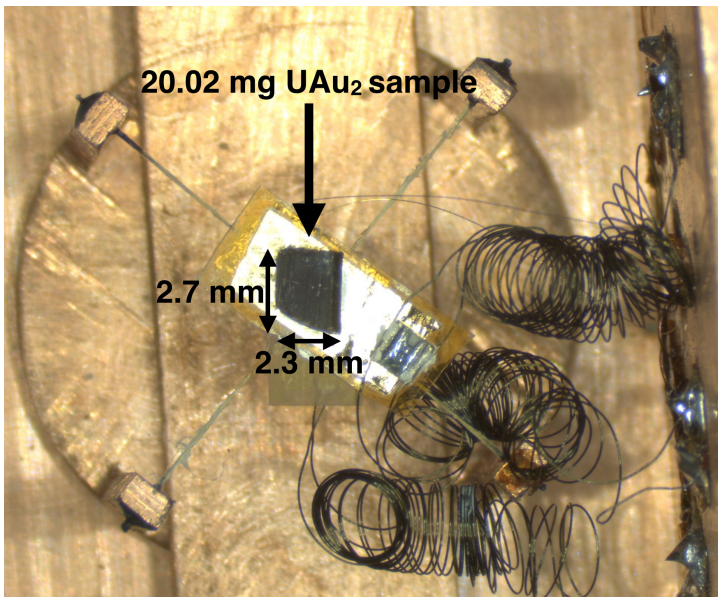

Figure 4.4 *The sample of UAu_2 is shown within the heat capacity probe, with weight and dimensions shown. The dark colour is indicative of the fast rate of oxidation.*

is from 129 mK to 3 K.

As shown below, the resistance measurements suggest that a T^2-dependence is achieved at a temperature of around 300 mK. This is supported by those measurements done for the annealed sample, and so the heat capacity of the un-annealed sample doesn't retain the corresponding behaviour expected for that phase. Thus, there is the possibility that the un-annealed sample doesn't become a Fermi liquid until below around 100 mK.

The peak at 420 mK in the PPMS heat capacity data is removed for further analysis. Although potentially indicative of a low-temperature ordering, errors in the calibration of thermometers installed within the PPMS machine can lead to such effects. This is possible due to recent repairs performed upon the PPMS, leading to new thermometers, and the calibration process is subject to the same errors that the process described here in section 3.3.2 is subject to, namely the reliability of already-calibrated thermometers, and ensuring thermalisation across all components. However, the matching gradient and magnitude between the two measurements of heat capacity contributes to the idea that the logarithmic increase is independent of crystal quality, and that the separately-calibrated thermometers inside both the PPMS and dilution fridge are giving equal readings.

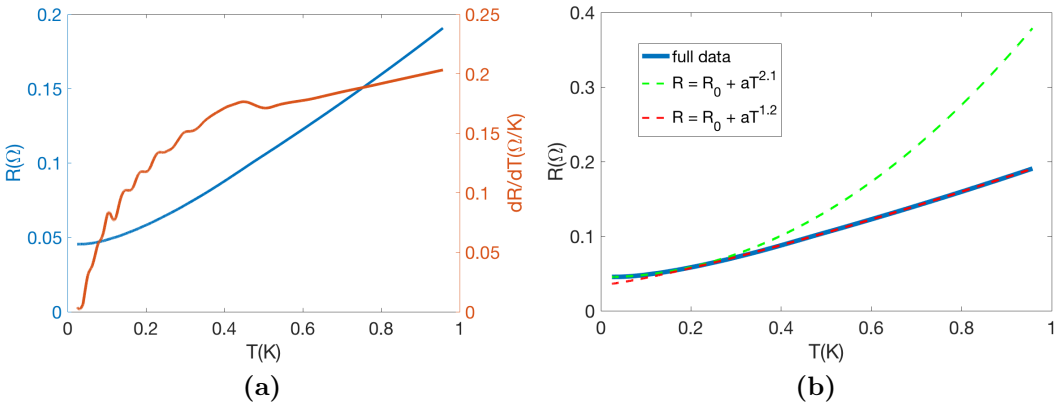

(a) (b)

Figure 4.5 *(a) The electrical resistance and first derivative with respect to temperature. A feature in dR/dT at 490 mK is visible, as are a series of similar features at lower temperatures. (b) A fit is made to specific ranges of the resistance vs temperature data, allowing the power of temperature to vary; below and above near 300 mK, the power changes from 2.1 to 1.2, indicating a smooth transition out of almost Fermi liquid behaviour.*

4.2 Electrical resistance measurements

To accompany these heat capacity measurements, the resistance of the unannealed sample was also measured between 20 mK and 950 mK, with the current applied parallel to the c-axis. To know the resistivity would have been ideal, but due to three dimensions of the sample differing on whether you measured from one side or another, there was therefore no useful geometric factor to measure. However, since the point of the measurements is to see at what temperature the resistance retains a T^2-type trend, and to see if there are any features around 420 mK, then the absolute values are not important.

Shown in Figure 4.5a is the temperature dependence of both the electrical resistance and first derivative of resistance with respect to temperature, the data shown in blue and orange respectively. This was measured by sending 100 μA through the sample with the output oscillator of a lock-in amplifier. While measuring the voltage induced via the four-probe method, the temperature of the dilution fridge was ramped. Although, due to the set point and ramp-rate of the mixing chamber PID, temperature oscillations were unavoidable, it is still possible to filter the data and smooth it into the line shown without losing any significant behaviour or features.

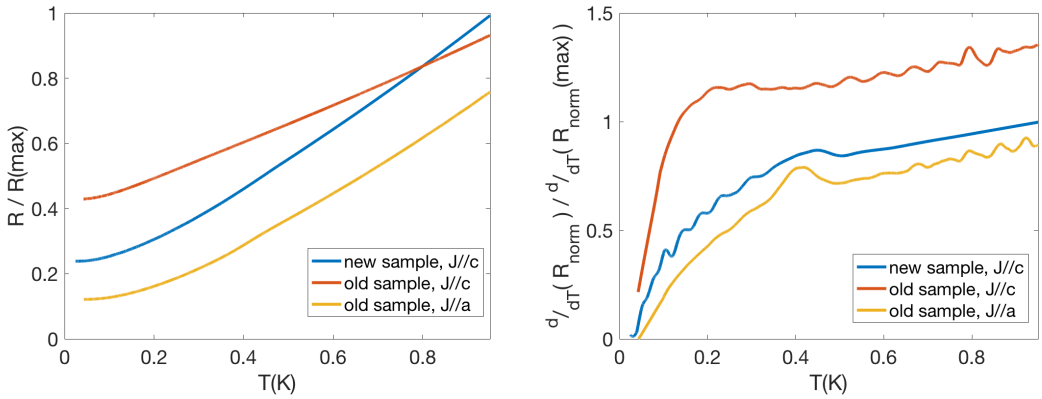

Figure 4.6 *(a) The temperature dependence of the electrical resistance of two samples; "old" refers to the annealed sample, and "new" for the unannealed sample. A normalisation process has been applied to both sets of data, where R_{max} is the resistance at 1 K. (b) The same type of plot as (a), but for the first derivative of resistance with respect to temperature. The similarities between behaviour along different crystal axis is discussed in the text.*

At a temperature of 490 mK, a kink in the first derivative is seen. On cooling further, a series of further kinks occur, while the general trend of the derivative is to drop towards zero, following the flattening out of the resistance. The kinks are attributed to the effect of taking the derivative of already-smoothed data - the range of a kink defines the data averaged over. The feature at 490 mK has been witnessed in another sample of UAu_2, although at a different temperature, as shown in Figure 4.6b [5]. What this transition may point to is a magnetic phase that is currently labelled as the f-phase, representing the possibility of ferrimagnetism. A larger fraction of the sample becomes ferrimagnetic when the crystal structure is strained, like when in powder form. This was seen in neutron scattering measurements [5]. The hexagonal structure that is perturbed by the process of powdering a crystal could be considered similar to an unannealed sample like that measured here. A higher temperature at which the transition is witnessed is a signal of the sample's low quality compared to previously measured samples. This could well be the reason for the lack of a hump in the heat capacity data.

A strange occurrence from comparing with the annealed sample is the similarity between the resistance along different crystal directions: shown in Figure 4.6a, the

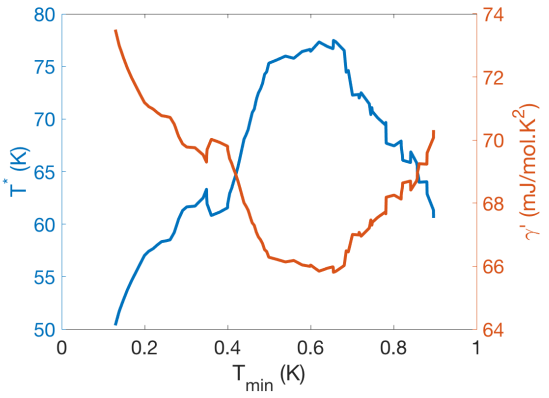

Figure 4.7 *By varying the lowest temperature that is fit to in the heat capacity data, the values of T^* and γ' change accordingly. As temperature is lowered, the value of T^* approaches T_N, but the switch in the gradient of both parameters around 600 mK indicates a possible limit to the applicability of the model.*

resistance along the a-axis in the old sample has a similar temperature dependence to that along c in the new; additionally, in Figure 4.6b, dR/dT for current along the a-axis is visibly most similar to the resistance measured here, both in relative magnitude, and in the presence of a smooth peak around 400-500 mK. The implications of these results are discussed below.

4.3 Results Analysis

First, the results of the fit to the heat capacity are discussed. As the temperature range over which the fit is applied is extended to lower temperatures, the value of T^* decreases significantly. This can be seen in the intercept of the fit with the temperature axis. By making the lower temperature that is fit to variable, the plot shown in Figure 4.7 is found.

One simple implication of these results is that T^* approaches the Neél temperature, opening the possibility that this temperature represents not only the edge of the anti-ferromagnetic phase, but also a further phase dominated by spin-fluctuations. This would make the possibility of a transition below the Neél temperature more reasonable, as it loses its exclusivity as an anti-ferromagnetic transition temperature. The entropy calculated from the heat capacity measured here, being the integral of C/T over the temperature range measured, is shown in Figure 4.8a.

The physics implied by these measurements and the fit comes under the heading of a "two-channel Kondo model" [49]. This represents a system of quasiparticles that would normally constitute a Fermi liquid, but with the addition of a single

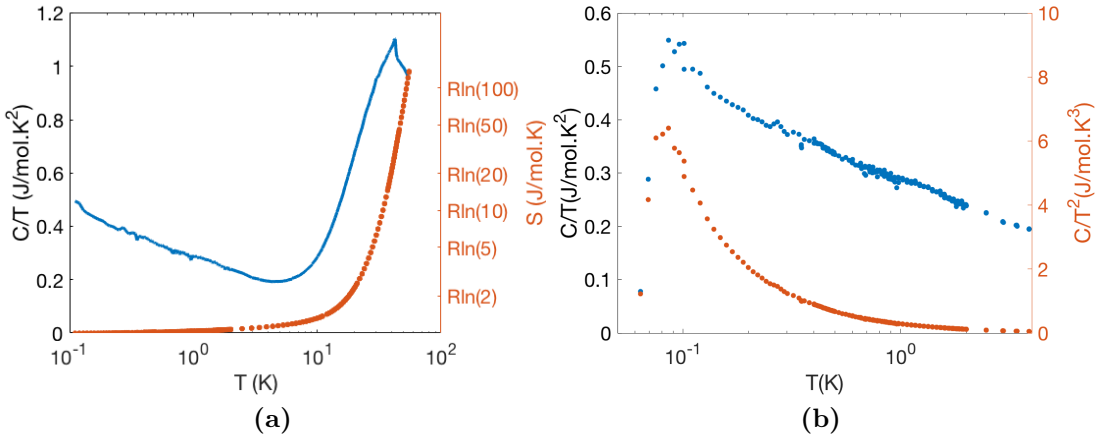

Figure 4.8 *(a) The entropy calculated from the full heat capacity data is shown with said data. The expected value of $S = R\ln(10)$ for UAu_2, with total angular momentum $j = 9/2$, is reached at 30 K. (b) Temperature dependence of both C/T and C/T^2, displaying no discontinuities above 101 mK. Additionally, the non-linearity of the latter data proves the irrelevance of a $C/T \propto T\ln(T^*/T)$-fit.*

impurity interacting antiferromagnetically with two separate conduction seas of electrons. The entropy is predicted to saturate to a value of $\frac{R}{2}\ln 2$ at zero temperature, implying the presence of another degree of freedom. Simply put, each coupling between a local impurity and the seas' constituents leaves a residual spin, which is free to do the exact same. If Kondo screening is represented by the initial coupling, then long-range order is represented by the residual/spare spin.

An alternative to this model is a "one-channel Kondo model" [108], where the modulation of spins along the c axis allows the existence of interstitial spins that are free to be made into a singlet with another spin from the conduction band. This results in a spread of Kondo temperatures across the system, and a logarithmic heat capacity. However, this theory predicts an inverse relationship between electrical resistivity and temperature, which is not witnessed across the temperature range measured both here and in [5]. The fit applied to the heat capacity is of logarithmic form, and the fit parameters are left undefined as to their corresponding meaning. Lonzarich argues [48] that for a non-Fermi liquid, the heat capacity follows a $T^2\ln(T^*/T)$-form; Figure 4.8b disproves this fit. The relevant trend is for $C/T \propto \ln(T^*/T)$, only holding true if the critical exponent z as well as the dimensionality of the system d is equal to 3 [48].

Additionally, for this system, a total spin of $j = 9/2$ implies the number of

microstates available is $2j + 1 = 10$, and thus a value for entropy of $R\ln(10)$ is expected as some low-energy limit. This is reached at $T \sim 17K$, but the Debye contribution has not been removed, so this is actually a lower bound for the actual temperature at which $R\ln(10)$ is reached.

For the resistivity measurements, the issue of how the resistance along one axis in one sample can resemble the resistance along a different axis in a different sample could be explained as follows: due to the small size of the sample, cutting a single crystal from the larger grown crystal can be inaccurate in whether the cuts are parallel to the crystallographic axis or not. To add to this, as the samples oxidise in a matter of hours, the sense of urgency can lead to further errors. Thus, there is the possibility that a cut thought to be parallel to the c-axis is not so, leading to contributions from the other axes. Given that the resistance along c in the old sample gives no sign of a transition at 420 mK, then the visibility of a peak in the resistance along c in the new sample means that a contribution from a is entirely possible.

Chapter 5

Results: Heat Capacity Measurements of URhGe

In this chapter, the results of measurements upon a few samples of URhGe are displayed and discussed. These measurements are of the heat capacity of both single-and-poly crystals, casting light on the fragility of superconductivity within these particular structures. The intention of these measurements was to find the temperature dependence of the heat capacity below the superconducting transition temperature. This can indicate what the arrangement of nodes upon the gap is, whether being lines, points, a combination of the two, or other. This anisotropy of the Fermi surface is an expected property of an unconventional superconductor. The measurements of both single- and poly-crystals will clarify whether their differences lead to a difference in thermodynamic properties.

Previous measurements [1] of single crystals have been shown to follow a $C/T \propto \gamma + aT^2$ form, implying the presence of not only a line node but also some sort of Fermi liquid state in superposition. This line node has been also suggested in thermal conductivity measurements [67], thought to manifest in the b-c plane due to the apparant anisotropy between b-c, a-c, and a-b, compared to the harder magnetic a axis. This is explored in more detail in section 1.3.2. Whether the same result is observed here for these particular crystals is discussed.

Although the previous chapter also detailed the results of heat capacity measurements, the methods used here were different. This is due to these measurements taking place before those of UAu_2, and so developments of the technique and

(a) (b)

Figure 5.1 *(a) A polycrystal of URhGe is shown with the batch and selection number, and in (b) this sample is loaded onto the heat capacity probe. The size of the sample is large compared to the sample platform, and the coils that make the electrical connections are seen to be bending around the sample.*

equipment used came after the measurements detailed in this chapter. However, the results show key aspects that are indistinguishable from previous data taken (namely that by Aoki *et al* [1]), proving some validity of the approach used. In terms of components used, the sample heater is a strain gauge of room temperature resistance 5 KΩ, the thermometer a RuO_2 resistance chip, and sample platform a 100 μm thick plate of gold. All of this makes up the addenda, and to thermalise this with the bath, a pair of 25 μm diameter, 15 mm long gold wires spot welded to the gold foil are clamped to the copper probe onto which the kevlar wires are mounted. The heater was placed between sample and bath, and so the problems encountered with that setup detailed in the previous chapter most likely occurred here too, although unnoticed.

5.1 Results

5.1.1 Polycrystal

First, the results found for a polycrystal of URhGe. This crystal is from a batch from which the results in [1] also originate. This sample is shown in Figure 5.1a, being of size 3×2 mm, and 1 mm deep (in the axes perpendicular to the camera).

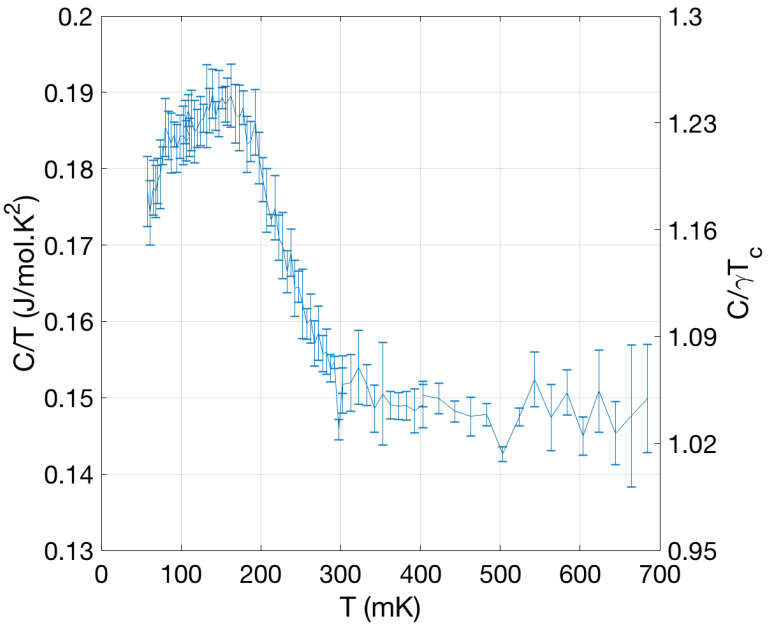

Figure 5.2 *The temperature dependence of the specific heat capacity of a polycrystal of URhGe is shown for 70 mK to 700 mK. The units are in J/mol.K^2 on the left-hand axis, and de-dimensionalised by dividing by the Fermi liquid value γT_c for the right-hand axis. Details are in the text.*

Due to its origins, it is expected to display a superconducting transition at a temperature close to 275 mK. This would indicate the high level of accuracy in growing the crystal in equal proportions of U, Rh, and Ge. By performing the relaxation method, the heat capacity data was acquired, shown in Figure **??**.

The temperature was ramped from a base temperature of 70 mK to just under 700 mK, over 86 data points. The spacing between points was chosen to be generally proportional to the temperature itself, reducing to around 3 mK for close to the transition and growing to 10 mK at the higher temperatures. Above 300 mK, the sample is supposedly in a Fermi liquid state. This would indicate a constant value of $C/T = 0.16$ J/mol.K^2. As can be seen, the value of C/T measured is approximately the same to within 10%, albeit with a random scatter about that value. Skepticism can be treated with respect to the accuracy, due to the value on which the heat capacity settles to after dropping from the peak at the lower temperature; a steady drop to 0.15 J/mol.K^2 can be inferred from the data shown. Usually, the addenda or sample-disorder can add a contribution, rather than take away. However, as

shown in section 2.2, the presence of thermal resistance between heater and sample can lead to a reduction in the heat capacity magnitude. A difference of 0.01 J/mol.K^2, referring to the difference between the measured and expected Sommerfeld value of 0.16 J/mol.K^2, corresponds to values for the thermal resistance that are indicative of the power from the heater becoming split. Concentrating on the range of temperatures defining the Fermi liquid phase, the calculated ratio of the thermal resistance of gold to Kapton is shown in Figure 5.3. How this calculation is performed is shown in Appendix B. These values do not take into consideration the difference in geometric factor between the two components involved, being kapton tape and gold wire[1]. The effect of the geometric ratio would be to severely reduce the resistance of kapton, and increase that for gold, bringing coherence with literature values listed in section 3.2.6. This reinforces the more intuivive result of gold maintaining a lower thermal resistivity than the non-metallic kapton tape. Thus, it is possible to account for a splitting of the power sent by the heater. Ideally, this issue is made redundant by reducing the thermal resistance between heater and sample to zero.

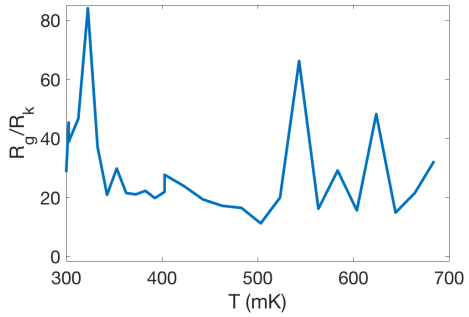

Figure 5.3 *The thermal resistance of kapton, quantified here as a fraction of that of gold, over the Fermi liquid temperature region is found to be significant.*

A large peak is seen, reaching a maximum at a temperature of 158 mK. The corresponding T_c, however, is taken as the midpoint of the rise in C/T, equating to 232 mK. Compared to the literature value of 275 mK, this is a 16% difference. Whether this can be accounted for through sample properties like mosaicity or the disproportionate combination of U, Rh, and Ge is difficult to narrow down. The size of the peak is also an indicator of whether the material is a conventional or unconventional superconductor; as shown in section 1.2.4. Thus, because the size of the peak relative to the Fermi liquid value, as shown in Figure **??**, is less than the BCS value of 1.43, then less ambiguity exists in saying the sample displays unconventional superconductivity.

[1]For the sheet of kapton, area/length = $6mm^2/30\mu$m = 0.2 m. For the gold wire, area/length = $\pi(12.5)^2/15$ mm = 32.7 nm.

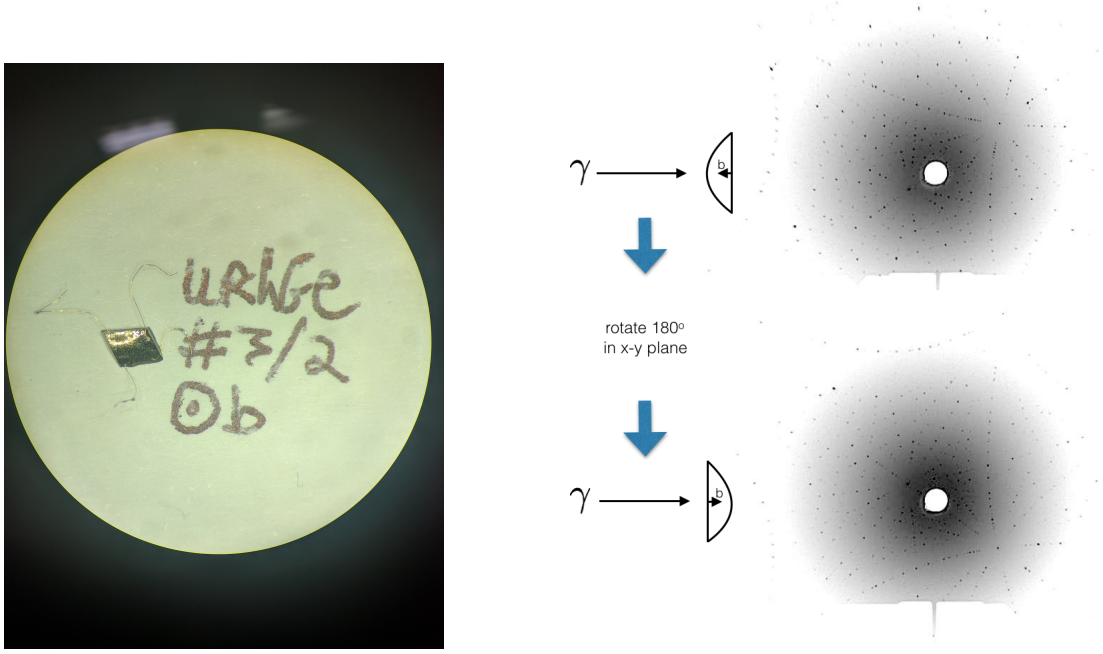

(a) (b)

Figure 5.4 *(a) A single crystal of URhGe is shown with the batch and selection number, and in (b) two laue scans displaying the consistent crystal structure throughout the sample, with details in the text. The crystallographic b axis, being into the page, is shown to be 2.3° off from being completely perpendicular to the flat face, which in finite-field measurements can be adjusted for in the probe.*

5.1.2 Single Crystal

Shown in Figure 5.4 is the single crystal used in this study. This particular sample was grown in Grenoble by Prof. Huxley. Whether or not this sample is a single crystal was clarified in the use of Laue scattering, performed in-house. By scattering a white beam of X-rays off one side of the sample, rotating it 180° in the horizontal x-y plane, then scattering again off the new face, then one detector image should be a 180° rotation of the other in the vertical plane; this is achieved and shown in Figure 5.4b. Additionally, whether or not this is a high-quality single crystal is a separate issue, and this is quantified fully after the heat capacity results are presented. Now, a discussion of two different approaches to calculating the heat capacity follows.

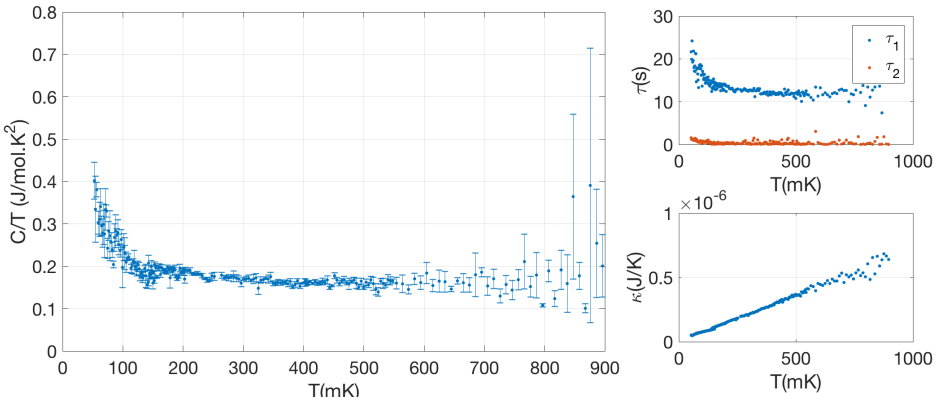

Figure 5.5 *By the 2-τ model, the temperature dependence of the specific heat capacity is measured and shown. The increase at lower temperatures stems from the values calculated for τ_1, shown top right. The lower right plot shows the thermal conductivity of the link between sample and bath, linear in temperature-dependence down to 50 mK.*

2-τ Model

In Figure 5.5 are shown the values of heat capacity found for the sample URhGe #3/2. At 205 temperature points between 50 mK and 890 mK, a heat pulse is applied four times consecutively, and a 2-τ model is applied to the data. This results in values for both relaxation times, as well as the thermal conductivity of the link between sample and thermal bath.

The results are somewhat different to those for the polycrystal, while still sharing some features. First, the high-temperature values do average around the Sommerfeld value for 0.16 J/mol.K^2, finding a mean value of 0.167 $\pm$ 0.034 J/mol.K^2, although with a spread in errors proportional to temperature. Second, the temperature at which a rise in heat capacity begins is around 130 mK, well below 300 mK as measured for the polycrystal. Down to the lowest temperature measured, this rise does not seem to cease, increasing by a factor of two by 50 mK. This rise is seen also in both relaxation times τ_1 and τ_2, shown in Figure 5.5. However, the thermal conductivity remains linear to the lowest temperatures, indicating the reliability of the addenda and thermal link to the bath.

Why there is an increase in τ_2 as temperature is lowered can be attributed to the silver epoxy bonding the sample to the addenda. Although literature suggests silver epoxy has a lack of temperature sensitivity in its heat capacity, as shown in section 3.2.6, the thermal quality of the bond will reduce at these extremities

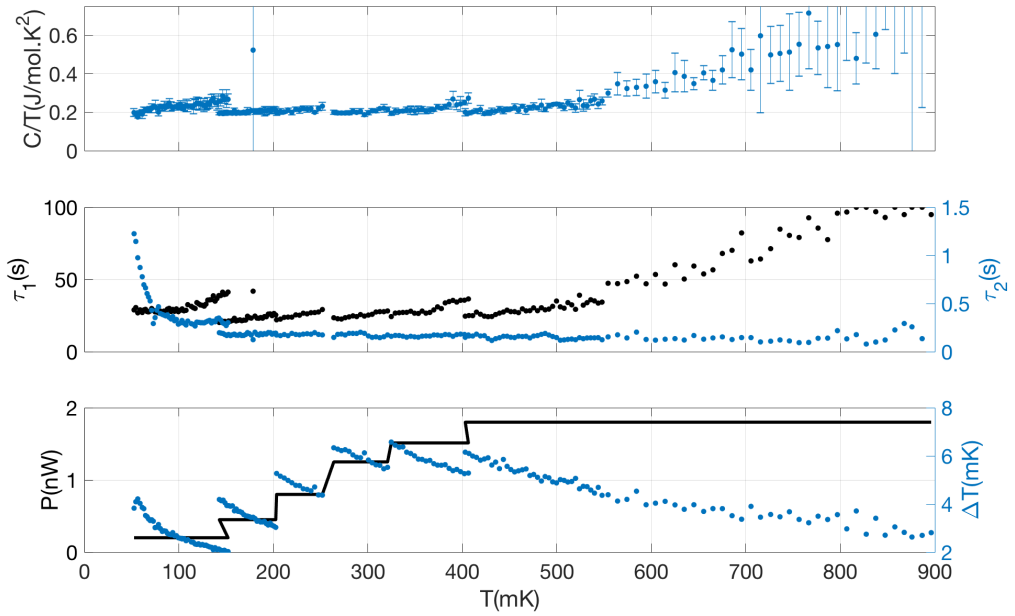

Figure 5.6 *By the 2-τ method, the heat capacity is calculated over the temperature range shown. At the same temperatures, the relaxation times τ_1 and τ_2, the power output of the sample heater, and the corresponding change in ΔT for the sample thermometer are shown. The coincidence of the discontinuities in C/T, τ and in P are discussed in the text.*

of temperature. A failure in the bond will naturally cause a lag in thermalisation between sample and platform, resulting in some finite τ_2. This quantity can be measured separately by another method, detailed below.

Brando Method

First, Figure 5.7 shows an anomaly that is the heart of the issues encountered here. The gradient of the logarithm of the change in temperature, in this case shown during the cooling period, is equal to τ_1. Shown are two plots of this, where the base temperature is different by 0.6 mK, but the power applied is different by more than double. A significant difference in τ_1 over a very small temperature range is drawn from these measurements, leading to the results shown in Figure 5.6. Large steps simultaneously in C/T, τ_1, and τ_2 (calculated from equation 2.10) occur at a variety of temperatures, corresponding to when the power sent by the heater is discontinuously changed.

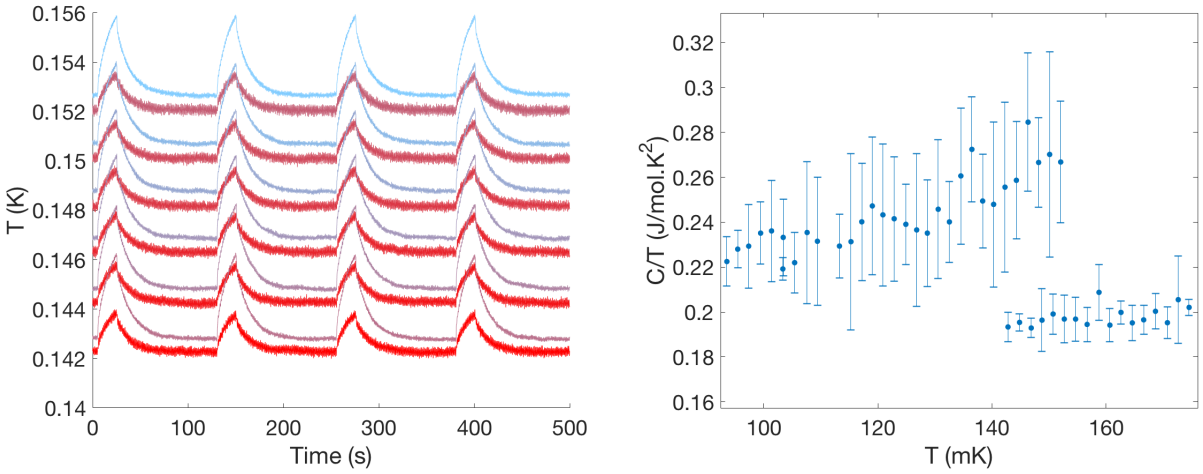

Figure 5.8 *Left: the raw data from which τ and κ are calculated. Red→blue indicates chronological order of measurements, repeating over the given T-range with a power 2.25 times bigger than the first run. Right: The resulting heat capacity over the same T-range, leading to a lack of uniqueness.*

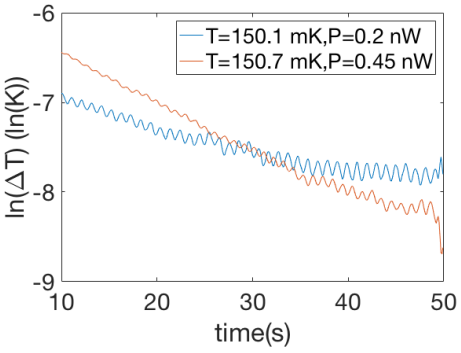

Figure 5.7 *The dependence of sample thermometer temperature on power applied from sample heater, for the same temperature to within 0.6 mK.*

The total temperature increase, ΔT, experienced by the sample thermometer suffers too from this discontinuity, and the proportionality between P and ΔT is what leads to a smooth thermal conductivity, $\kappa = P/\Delta T$. The relaxation time should well follow suit too, whereas these measurements give multiple values of τ for the same temperature. By looking at the raw data, it is possible to see these effects, shown explicitly in Figure 5.8. From red to blue, the sample thermometer data taken in chronological order are shown, repeating over the range 142 mK to 152 mK with an increased value for the power output of the sample heater, and an increased value for the excitation current of the thermometer. These changes were performed due to the very small ΔT observed leading to large variations in τ, as well as the noise being larger than the temperature resolution. The corresponding heat capacity is shown to drop for the repeated temperatures, and this is seen to stem from the values of τ shown.

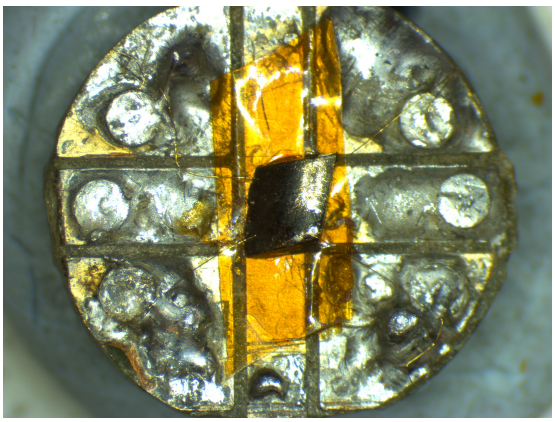

Figure 5.9 *URhGe sample #3/2 is shown glued to a terminal with GE varnish, to be loaded into a ^{4}He cryostat. Four 25 μm gold wires lead to solder pads, arranged in such a way that the Van der Pauw technique is implemented.*

The rest of the heat capacity data is no more illuminating as to the causes of these anomalies. The increase in excitation current applied to the thermometer may slightly shift the temperature, due to self-heating, although this has been argued to be non-applicable above 100 mK. The calibration of the thermometer changing between measurements could also be a cause, although unlikely given the small number of times the thermometer had been thermally cycled[2].

The scale of the full data set is much larger than those values found for the polycrystal, and the general increase of C/T with temperature could well be proportional to the increasing thermal instability of the probe. Thus, in order to see if the sample is superconducting, resistivity measurements were performed to see the second-order transition, and quantify the quality of the sample in terms of its relative resistive ratio (RRR). However, all attempts to measure the superconducting transition ultimately failed, due to grounding issues; however, the RRR measurements provide some support for the reason no superconductivity was observed in the heat capacity of the single crystal.

5.1.3 Sample Quality and Characterisation

The single and polycrystals used during this experiment were grown by Prof. A. Huxley. The crystal quality, or RRR, of URhGe #3/2 was measured previously

[2]The thermometers used were delivered pre-thermally cycled, thus insensitive to further changes.

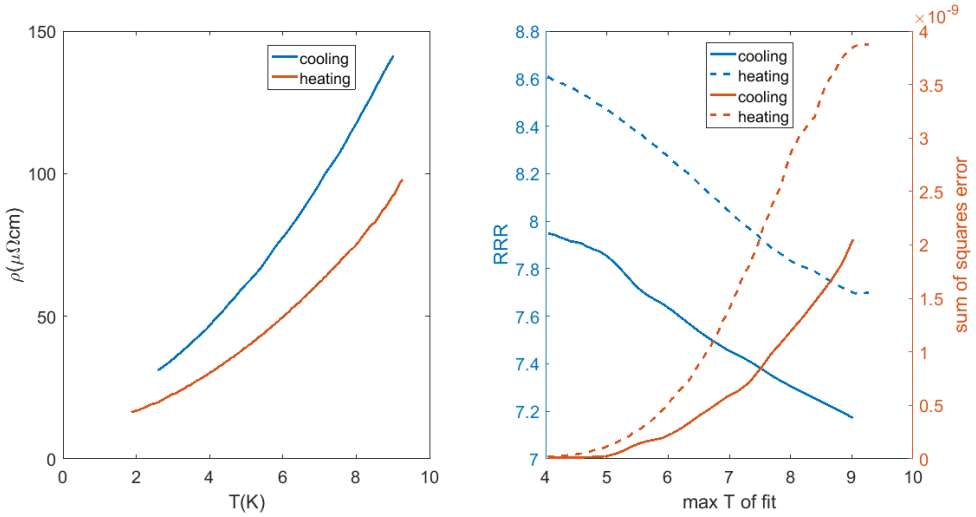

Figure 5.10 *Left: resistivity data during cooling and heating of the cryostat, with the voltage and current pins swapped between. Right: values for RRR measured plus their respective errors. Details in the text.*

by Prof. Huxley to be of the order of 8, which corresponds to the lower end of sample quality. To measure the RRR, the sample is placed in a Cryogenics cryostat, a device that can regulate a base temperature of 2 K. Spot-welded to the top surface are four 25 μm diameter gold wires in a four-probe Van der Pauw arrangement, to allow a lock-in amplifier to send a current through two of the four wires, and measure the induced voltage with the remaining pair; this is shown in Figure 5.9. 5 V are applied across a 1 KΩ resistor, which sends 5 mA into the cryostat and through the sample. The signal is then fed back out the cryostat, into a transformer which amplifies the signal by 500, and finally read with the lock-in amplifier at a frequency of 37 Hz.

An average value for the RRR is collected, as the Van der Pauw method dictates. If it was required to know the RRR along a specific axis, then the wires would be arranged along that axis, but because the heat capacity measurements taken here are at zero field, then even though the c-axis may be most susceptible to the electron dynamics present, these non-axis-specific measurements should still be useful.

In Figure 5.10 is the data collected over the temperature range 2 K - 10 K. The resistance data is converted into resistivity, taking into consideration the geometry of the sample: 3.5 $\times$ 2.5 $\times$ 1 mm. After measuring during a steady cool-down, then because the electrical connections were arranged in a

square, then the pins chosen for voltage are swapped and the resistivity re-measured during the temperature increase; a different resistivity is expected between the two temperature ramps, due to the electrical path changing. Those paths, although not confirmed with a Laue scan, are thought to be roughly along the a-axis during cooling, and c-axis during heating. In the left-hand plot, the two separate resistivity readings are shown, both obeying a non-linear temperature dependence. In the right-hand plot, the x-axis represents the maximum temperature to which a Fermi-liquid fit is applied. The idea here is that the inclusion of more data adds statistical weight, balanced with the risk of including data that is not necessarily conforming to that model. That balance is quantified in the right-hand axis, displaying the sum of squares error for each maximum temperature chosen.

The results for the RRR are 8 and 8.6 for the cooling and heating ramps respectively. This agrees with previous measurements, and as the amount of data included in the fit is increased, the variation in those values reaches a maximum of $\sim 10\%$ ($= 100\times(1 - \frac{\mathrm{RRR}_{min}}{\mathrm{RRR}_{min}})$).

In order to account for possible deviations from quadratic behaviour, one can let the power of temperature drift, i.e. $\rho(T) = \rho_0 + AT^n$. Despite the fitting, above 2 K the resistance isn't expected to adhere to a T^2-dependance. Additionally, the many paths the conduction electrons take between the pins, due to the van der Pauw arrangement, adds a potential source of systematic error. Thus, in Figure 5.11 is shown the results of allowing the power of T to drift. By allowing n to drop to a value of 1.8 ± 0.05, the RRR increases above the previously-thought value of 8. The scale of that increase however is not large enough to bring the crystal into a higher level of quality where the superconducting temperature is within 10% of 275 mK.

In [1], the authors report that the values of ρ_0, being the residual resistivity, required in order for superconductivity to be visible are less than 30 $\mu\Omega cm$. One can see by eye in Figure 5.10 that ρ_0 is of the order of 20 $\mu\Omega cm$, by following the lines into the y-axis; this could well be not low enough to satisfy the samples' requirements. Additionally, in [67] a sample of RRR = 5.5 is reported to not display superconductivity to the lowest temperature measured of 30 mK, so the crystal reported here is unsurprisingly following the same behaviour given its similar RRR to within a factor of 2.

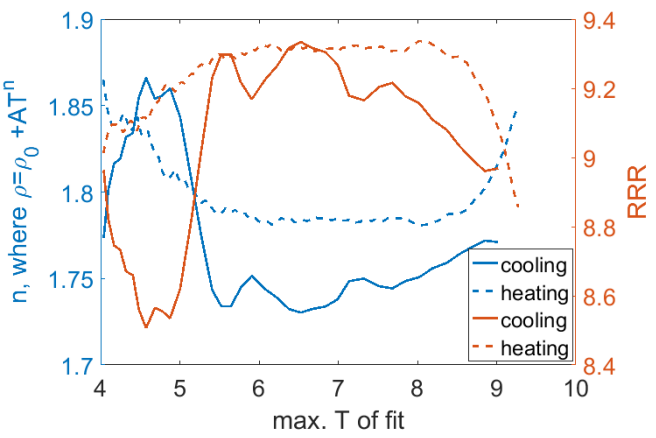

Figure 5.11 *Left axis: the best-fit power of temperature to describe the resistivity. Right axis: the RRR found for each data set, varying with maximum temperature included in the fit.*

5.2 Discussion

For the single crystal, its superconducting properties were not detectable with the addenda designed and implemented here. The temperature stability of the sample thermometer was low, failing to keep the variation less than 10% of the set point. This fed into the heat capacity measurements, meaning that when a fit is made to $T(t)$, the error in the fit parameters is large.

The polycrystal, on the other hand, does display a transition when a simple 1-τ model is applied. Figure 5.12 shows this, plus the heat capacity measured in [1]. The offset in critical temperature can be explained by differing quality, despite the origins of both data being from the same crystal growth - inhomogeneities can lead to varying qualities of polycrystal. Additionally, the size of the jump is reduced for the present sample, and the width of the peak is larger. This can occur due to the splitting-up of the superconducting phase across the multiple domains throughout the crystal structure, which leads to a staggered transition. Also shown in Figure 5.12 are the fits to both sets of data for there being a line node in the b-c plane, indicated in the legend by the fit parameters γ & A. These fits differ, as can be seen clearly, with $\gamma_{poly} = 0.171$ J/mol.K^2, and $\gamma_{Aoki} = 0.106$ J/mol.K^2. For the coefficient of temperature, $A_{poly} = 1.052$ J/mol.K^4, and $A_{Aoki} = 2.887$ J/mol.K^4. The γ term indicates a non-zero heat capacity at $T = 0$, and the two values here differ by 38%, significantly different to the percentage difference between the critical temperatures.

A feature common to both, however, is potentially the most interesting in terms of Fermi surface geometry. The non-zero value of γ implies that at zero temperature,

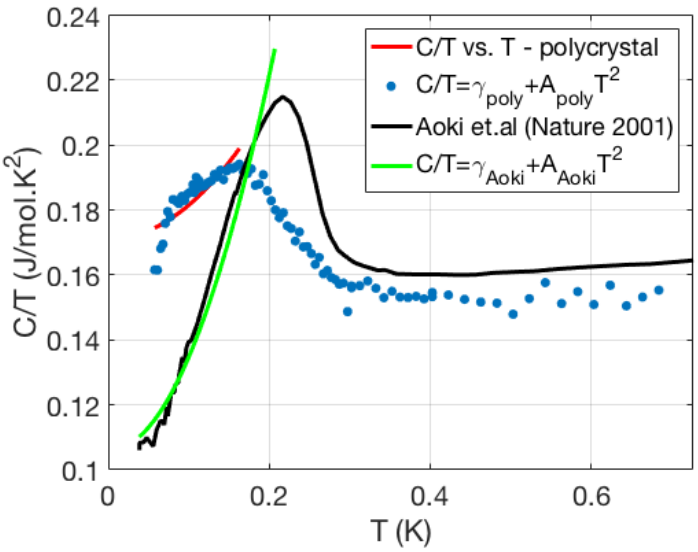

Figure 5.12 *The heat capacity divided by temperature of the poly-crystal measured both here and in [1], versus temperature. A fit is applied to both sets, with the differing fit parameters shown in the legend. These are discussed in the text.*

there is still some finite non-superconducting fraction of the electrons present. This property is common to UPt_3, and in [36, 109] it is made clear what it can imply: with the sufficient type of impurities, scattering at low temperatures results in a phase shift of $\pi/2$ for the electrons present. Such scattering broadens the angular range over which the gap is suppressed to zero close to a node. Calculations for the heat capacity for a generic spherical Fermi surface with anisotropic coupling is shown in Figure 5.13, where for a variety of both nodal types and impurity concentrations, the finite C/T at $T = 0$ is maintained. For UPt_3, this results in the line nodes being opened up into a partially-two-dimensional gapless region, allowing residual normal quasiparticles to exchange energy across the surface. This shows a

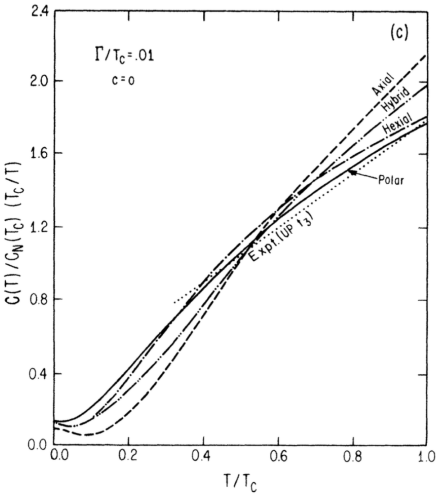

Figure 5.13 *Normalised C vs. normalised T for an impurity concentration of 0.01 and a variety of node types gives finite entropy at $T = 0$ [109].*

certain sensitivity of the material to impurities, where even the cleanest of crystals with critical temperatures very close to the ideal still display normal behaviour; the density of states, as formalised in equation 1.15, immediately becomes finite at the Fermi surface in the presence of some level of disorder. The type of scattering that can induce this phenomena is unitary scattering, corresponding to an infinite scattering length and zero effective range, thus affecting all electrons within the vicinity of the Fermi surface. It is not unreasonable to extend this phenomena to URhGe, due to the large residual heat capacity.

However, the opening up of line nodes into larger areas of gapless normal Fermi surfaces is not the only possible explanation for URhGe. Another source of error for this material is the inhomogeneity of the sample, leading to a spread of transitions and a broadening of the peak. The ferromagnetism can also lead to, say, up-spins becoming superconducting, and the remaining normal-state down-spins in some domains adding some residual entropy.

In summary, the result found here is that this polycrystal of URhGe is a superconductor, and the finite entropy when extrapolating the data to $T = 0$ can be most reasonably explained by the samples' inhomogeneity. The single crystal measured also showed some criticality at temperatures below 200 mK, but the magnitude and temperature dependence were different enough from the polycrystal for the low crystal quality to be clearly detrimental to the measurements. The method and equipment used was suitable for measurements above 100 mK, but temperature stability below became bad enough for measurements of single crystals to be inconclusive.

5.2.1 Future Work

In order to measure the heat capacity at finite values of magnetic field, a few components of the addenda would need to be finalised. First, the RuO_2 thermometer would require another calibration across both temperature and field values, to account for any drift in resistance that has occurred after multiple uses, and to see if the same issues regarding relaxation times when measuring the magnetoresistance would arise, as shown in section 3.3.3.

The magnetic signature of the addenda heat capacity would need to be traced accurately. The anomalous materials present (silver epoxy, GE varnish) have

potential impurities which are sensitive to such magnetic effects, although there is literature to suggest their field dependence is minimal [87]. A source of large Schottky anomalies is Manganin wire, which has been avoided in the setup used here. Further difficulties regarding the field-dependence of Schottky anomalies would also need to be dealt with, as was discussed in [110]; what was inferred from measurements of $CeCoIn_5$ at temperatures as low as 119 mK with the anomaly subtracted away, lose significance when compared to measurements at 300 mK, implying the difficulties of practicing at these temperatures.

The sample to measure would be a higher-quality single crystal, ideally from the same batch as used in [2], and all necessary characteristics would be measured beforehand. This includes electrical resistance at all fields down to, at the most, 50 mK. This guarantees the ability of heat capacity measurements to probe the nature of phase transitions at all parts of the phase diagram. Additionally, the method used to attach the sample to addenda would be made more robust, to minimise the effects of τ_2. Using a vice would help provide the necessary force, and a thin wooden or plastic rod to apply local pressure to the sample.

Finally the kevlar wires used to suspend the addenda would be tensioned to a higher degree; there was slackness present while attaching the addenda to the wires. This would be done with the careful application of stycast epoxy to a larger fraction of the wires where they thread the vertical copper rods shown in Figure 3.5.

Chapter 6

Results: Small Angle Neutron Scattering on URhGe

The use of neutrons allows the observation of electron dynamics within heavy fermion materials. The realisation of electron dynamics in URhGe is in the form of longitudinal fluctuations of the magnetisation. Here the background and theory of small angle neutron scattering is introduced, followed by the results of performing such measurements upon a single crystal of URhGe.

6.1 Background and theory

Here I will detail the use of neutrons for probing both structural and magnetic correlations within appropriate materials. The use of neutrons to provide insights into crystallographic and magnetic structure is well understood, having been used for decades. A particle of neutral charge, the penetrative abilities of a neutron compared to a proton or electron is extremely high due to the lack of a Coulomb-type interaction between the bombarding particle and the sample. Magnetic scattering is achieved in this work, where the spin of the neutrons interacts with the spin of the electrons present in the particular phase being probed.

For more detail than that given here, one can look to Chaikin & Lubensky [4] and to G.L. Squires [111] for magnetic neutron scattering. However, some detail is necessary; Bragg scattering is the constructive scattering of neutrons from

points of high symmetry, usually the locations of atoms with a crystallographic structure. By analysing the phase difference between incoming and outgoing neutrons, one can have an idea of the dimensionality of the crystal structure by utilising the relation between wavelength and crystal spacing: $n\lambda = 2d\sin(\theta)$. The coherent scattering that arises from domains of such periodicity is not limited to crystal structure; magnetic correlations can cause the same peak in scattering. For example, Ferromagnetism can occur in domains, with each domain's spins aligning, but the domains not necessarily aligning with one another. Each domain can have some characteristic length, ξ, and thus a function that encompasses whether two spins are in the same domain or not must be a function of distance, leading to the spin-spin correlation function, $G(r)$:

$$G(r) =< \overrightarrow{S_i}.\overrightarrow{S_j} >_r \tag{6.1}$$

where $\overrightarrow{S_j}$ represents the spin of a fermion within some domain. The measured intensity from neutron scattering is related to the correlation function via a Fourier transform [112]. The correlation function gives an indication of the characteristic length of a domain of, say, ferromagnetism, where if $r \ll \xi$ then the pairs of common points are within the same domain and $G(r) \approx 1$, and if $r \gg \xi$, then any magnetic ions present are pointing in directions unrelated to one another, and $G(r) \to 0$.

Neutron scattering of the type performed here probes, at the simplest level, a collection of nanoparticles in a matrix. That separation of the system into two parts is key, as they can be separated out in the analysis by writing down what is known as the *scattering cross section*, formulated as σ. There are different contributions to σ, being σ_{scat} and σ_{abs}, the latter accounting for those neutrons absorbed by the sample, and the former for those scattered onto the detector; this is the σ that's measured. In layman terms, σ is the effective shadow cast by the system when shone at, and thus has dimensions of area. Traditionally the unit of *barns* is used, being equal to 100 fm^2. The measured quantities in these experiments are functions of this σ_{scat}, and although one can write down a generic "simple" form for σ_{scat}, complications concerning the spin-state of the neutron bombarding the system, the magnetic orbitals of the system, and interactions of the two leads to complex formula. Here, a relatively simple form for σ_{scat} is used, based on a few assumptions.

Small angle neutron scattering (SANS) is a commonly used technique in the

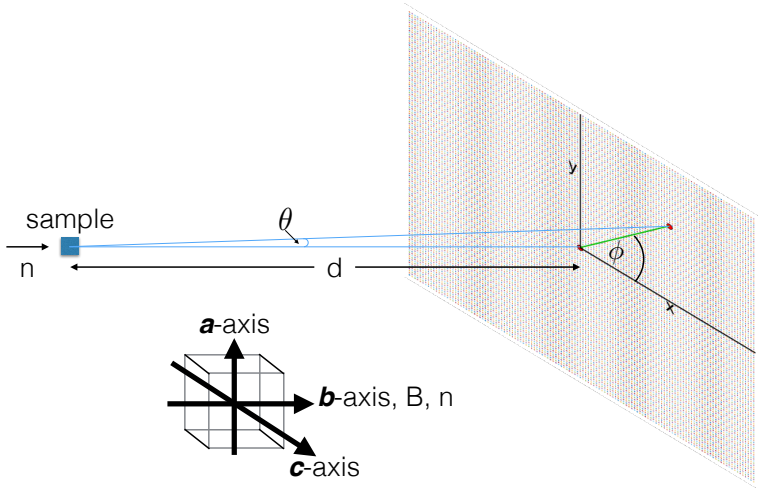

Figure 6.1 *Geometry of the experiment, showing the detector plane normal to the neutron beam, including the physical realisation of the angles θ and ϕ that are utilised in equation 6.18. The sample alignment is also shown, with the b-axis aligning with both the magnetic field B, and neutron beam n.*

determination of low-energy phenomena [9]. In this method, a beam of highly-collimated neutrons is shone at a sample, the wavelength of the beam being chosen to maximise scattering off the crystal itself. The beam is scattered weakly over a range of angles, captured on a detector which can be moved in the axis of the beam, the larger the distance from sample corresponding to a smaller angle detected significantly. The pattern captured is analysed to see where the peak scattering occurs in q-space. The geometry of the setup is shown in Figure 6.1.

A few simple assumptions about the neutrons can lead to some very powerful proposals. For example, the energy of the neutron scattered from the sample is assumed to have lost near to zero energy in the process, thus defining an elastic type of scattering. This means that the scattering wave vector, $\overrightarrow{Q}$, can be determined simply from geometry, where $\overrightarrow{Q} \approx \frac{2\pi\theta}{\lambda}$, θ is the scattering angle, and λ the neutron's de Broglie wavelength. However, in order to account for any inelastic scattering, energy is integrated over when simulations are performed, as detailed in section 6.4.

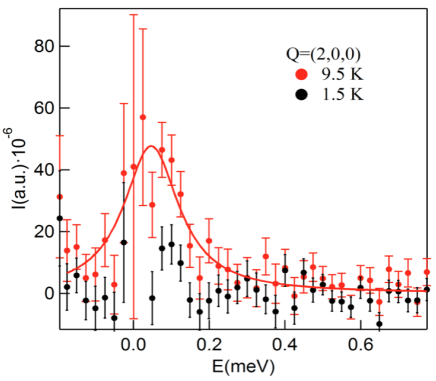

(a) *Unpublished Inelastic neutron scattering performed on URhGe, showing a peak at 9.5 K at an energy low enough to justify the need for SANS.*

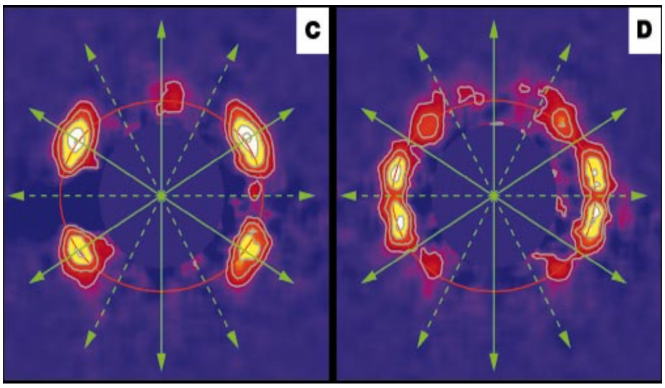

(b) *How the scattering changes in UPt_3 when zero-field cooled to different temperatures. Panel **C** shows scattering along the crystallographic directions of the hexagonal structure in the B-phase; panel **D** shows a rotation of those scattering peaks to along the lines of symmetry of the SC order parameter in the C-phase [18].*

Figure 6.2

6.1.1 Previous SANS Studies

This requirement of the resolution of small angles was evident after an inelastic experiment using triple-axis neutron scattering on URhGe at ISIS, England, the results of which showed the need for higher resolution. This is why this technique was chosen for this experiment, as the magnetic fluctuations expected in URhGe occur at an energy below 0.1 meV, as shown in Figure 6.2a [113]. Although scattering may occur across the whole spectrum of q-space, by placing the detector a distance of up to 12 metres away, this focuses the range of measured scatterings on those of low q, as the higher range will miss the detector completely. Why the key phenomena occur at such low energies is related to the spectrum of scattering existing over a large range in q, especially so for non-interacting electrons. If, however, there are some electron interactions as might be the case for URhGe, then the fluctuations can be slowed down to a point that they are measurable, particularly near a ferromagnetic transition.

This approach is also useful for measuring the flux-line lattice in type-II superconductors [18], where for UPt_3, shifts in the location of diffraction spots were detected during the transition from one superconducting phase to another, displayed in Figure 6.2b. In the same way this shift can be quantified in terms of the order parameter gaining/losing symmetry as temperature is lowered, a

shift in the critical scattering as field is applied can be quantified in terms of the energy scale of magnetic fluctuations. The similarities stop there, as it wouldn't be possible to image the flux-line lattice in this particular sample of URhGe. It's lack of superconductivity is due to the difficulties in gaining the right proportion of Ge relative to U and Rh, bringing the RRR down. Smaller samples, being of inappropriate dimensions for SANS, are more likely to display superconductivity.

6.1.2 Magnetisation Fluctuations

Why there are fluctuations in the magnetisation can be answered as follows. As mentioned in section 1.3.2, the Curie line represents a phase transition from paramagnetism to ferromagnetism. Like there is for any phase transition, the order parameter for the low-temperature phase goes through a few changes during this transition. These changes concern the fluctuation of the value of that order parameter, which in this case is the magnetisation, physically manifested by collections of electrons flipping their spin repeatedly. As the amplitude of fluctuations grow, the magnetisation will grow in sparse domains to some finite value. Accompanying this, the timescale over which the fluctuations reach peaks and troughs increases, dilating the lifetime of each possible domain. At $T = T_C$ exactly, both the length-scale and time-scale diverge completely, establishing the new phase. What SANS can observe is specifically low-energy electrons fluctuating along the directions corresponding to the easy-magnetisation axis, being the same electrons potentially responsible for superconductivity. Quantifying their contribution involves formalising the susceptibility in terms of those possible fluctuations.

To understand how one quantifies a fluctuating order parameter within a magnetic system, the Fluctuation Dissipation Theorem can be utilised [48]. What this encompasses is understanding what happens when two systems dissipate energy into one another, finding some stability from two unstable systems. In this case, the two systems are the crystal-and-magnetic structure, and how they dissipate energy into one another is seen as the magnetisation fluctuations being damped by one of a few different dissipative processes. In this work, one can narrow down those processes to three possibilities, each manifesting in reciprocal space their own q-dependences of γ_q, the energy of fluctuation-damping. They are ballistic Landau-damping, $\gamma_q \propto q$ [48], diffusive Landau damping, $\gamma_q \propto q^2$ [114], and non-Landau damping due to itinerant electrons, $\gamma_q \propto \gamma'$ [115]. The diffusive model

has been observed in Ni, Ni_3Al, and Fe [116–118]. The constant γ_q model is the newest addition, originating from itinerant electrons absorbing the magnetisation density.

A fluctuation can also be defined in real-space, corresponding to spins rotating rapidly along a particular direction. Most examples of magnetic fluctuations can be simplified into longitudinal and transverse components, and in [26] the former are proposed to induce pairing for superconductivity.

6.1.3 Dynamic and Static Susceptibility, χ'' & χ_0^{-1}

As the magnetisation in URhGe is considered due to local moments, then the no-q-dependence model works on the basis of some interaction between local and itinerant electrons; this results in $\gamma_q = \gamma'$. The other two models work on a basis of there being some motion of the local moments, and their trajectories either being ballistic and at the Fermi velocity ($\gamma_q \propto q$), or diffusive and at slower velocities ($\gamma_q \propto q^2$). Each of these possibilities are observable in the imaginary magnetic susceptibility, related to the intensity of scattering via the structure factor $S(q)$:

$$2\chi''(q,\omega) = \left(1 - e^{-\beta\omega}\right) S(q,\omega) \tag{6.2}$$

$$\chi''(q,\omega) = \chi_q \frac{\Gamma_q}{\omega^2 + \Gamma_q^2} \tag{6.3}$$

$$\Gamma_q = \chi_q^{-1} \gamma_q \tag{6.4}$$

where $\chi''(q,\omega)$ is the imaginary part of the magnetic susceptibility, assigned as being related to the dissipative processes within the response function of the system. In a conventional paramagnon theory of nearly ferromagnetic metals, the intensity of the scattering of neutrons is directly proportional to this term, and thus should be known exactly. Additionally, the proportionality of Γ_q to χ_q^{-1} means that, at the point of transition, the rate of damping will freeze up, supporting the idea of time-dilation associated with a phase transition.

The correlation length of a fluctuation can be defined in terms of the static susceptibility χ_0, and magnetic stiffness parameter c_α [48], where α represents a crystal axis. The former has a temperature dependence that diverges at T_C, whereas c_α has none, resulting in the temperature dependence between ξ and χ_0^{-1}

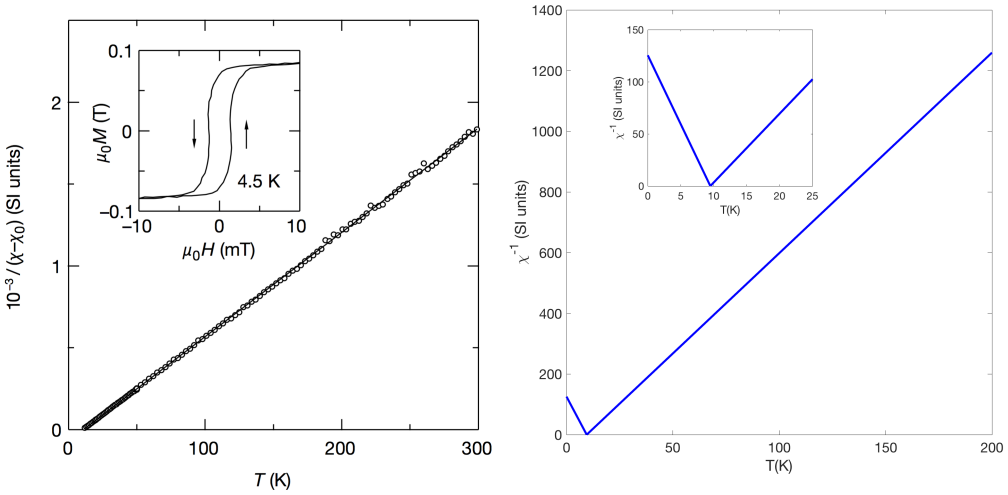

Figure 6.3 *The inverse magnetic susceptibility χ^{-1}, as measured [1] and predicted [9] for a value of Curie-Weiss moment of $1.8\mu_B$ and $T_{Curie} = 9.5$ K; the similarities between them are indisputable.*

being equal. There is frequency dependence, the origin of which is the damping expressed in equation 6.3. This allows one to express the susceptibility as follows, due to the Curie-Weiss law [9].

$$\chi_q = \chi_0(T) = \frac{n\mu_0 \left(\mu_B \mu_S\right)^2}{3K_B} \times \begin{cases} \frac{1}{T-T_C}, & \text{for } T > T_C \\ \frac{1}{2(T_C-T)}, & \text{for } T < T_C \end{cases} \tag{6.5}$$

$$\therefore \xi = \sqrt{c\chi_0(T)} \tag{6.6}$$

In Figure 6.3 is shown both the results of the above calculation for χ_0^{-1}, and the direct measurement from [1], proving the relevance of the Curie-Weiss model. Here, the susceptibility will be split into the highly-anisotropic *b*- and *c*-axis contributions, as shown in Figure 1.11. As field increases, the value of T_C changes appropriately, so this is taken into consideration within the calculations. What is expected is an increase of ξ_b as the field approaches values of 11-12 T, reflecting the rotation of the magnetic moment. This will be revealed in chapter 6. In practice, the singular nature of χ_0 around T_C will mean small errors in temperature can cause large changes to ξ. This will be taken into consideration when performed in chapter 6.

6.1.4 Implications of Landau & non-Landau Damping

Landau Damping

In [119], Lonzarich and Taillefer discuss the calculation of the dynamic susceptibility for a system under an external magnetic field. They derive forms for the fluctuation parameters that are sought after here, γ_q and c_α, from the dynamic susceptibility. The energy difference between spins aligning and anti-aligning with said field leads to a difference in occupation number of those states. The resulting magnetic susceptibility, including its q-dependence, is calculable from the Lindhard function, a form of response function for electron dynamics. When this formula is extrapolated to zero q, the resulting form for the Pauli susceptibility is

$$\lim_{q\to 0}\chi_p = \lim_{q\to 0} 2\mu_B^2 g(\epsilon_F)\left(\left(\frac{1}{2}+\frac{k_f}{2q}(1-\left(\frac{q}{2k_f}\right)^2)\right)\left(\ln(\frac{1+\left(\frac{q}{2k_f}\right)}{1-\left(\frac{q}{2k_f}\right)})\right)\right) \quad (6.7)$$

$$= 2\mu_B^2 g(\epsilon_F) \quad (6.8)$$

This relation between susceptibility and the density of states $g(\epsilon_F)$ allows one to understand more about the microscopic contributions to the magnetic behaviour. The total dynamic susceptibility calculated from this gives an equation of the form

$$\chi(q,\omega,M) = \chi^{-1}(M) + c(M)q^2 - \frac{i\omega}{\gamma'(q,\omega,M)q} \quad (6.9)$$

Landau damping has been implemented here, originating in the response function proposed in the Lindhard function. From this, the power spectrum for magnetic fluctuations can be calculated by taking the imaginary part, and the resulting Lorentzian has the familiar width Γ_q. At this point its possible to extract the values c and γ to leading order:

$$c = \frac{\chi_p^{-1}}{12k_F^2} \quad (6.10)$$

$$\gamma' = \frac{2\chi_p}{\pi\chi_0}v_F \quad (6.11)$$

Thus, it is possible to gain a value for the Fermi velocity v_F of the electrons present from measuring γ'.

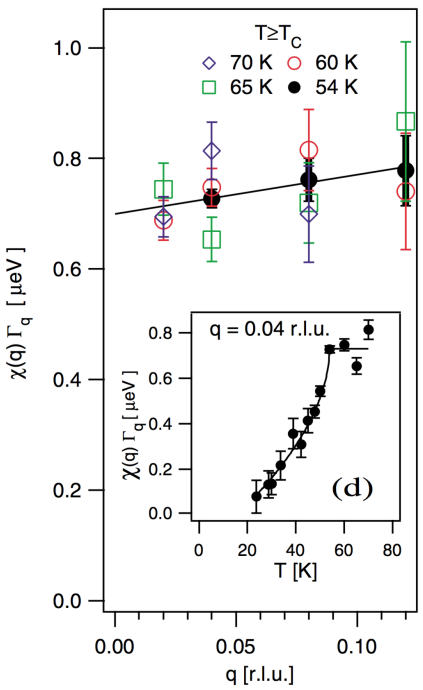

Figure 6.4 *Shown is the lack of q-dependence of $\gamma_q = \Gamma_q \chi_q$ at a variety of temperatures above T_C in UGe_2, suggesting the magnetisation density is not conserved, and that spin-orbit coupling may well be contributive; inset, how γ changes with temperature at q=(0,0,0.04) [10].*

Non-Landau Damping - Random Motion Aspects & Itinerant Electrons

As laid out in [114], for $\gamma_q \propto q^2$, the motion of the electrons around the Fermi surface is thought to be governed by the same equations that control random motion, resulting in a diffusion constant D:

$$\Gamma_q = \gamma_q \chi_0^{-1} = Dq^2 \tag{6.12}$$

By relating the distance travelled, $2\pi/q$, to the scattering time τ and number of collisions N, and by recognising that the magnetic fluctuations' energy can be interpreted as a frequency through $\Gamma_q = \hbar\omega$, then γ_q can be calculated. The mean distance covered is equal to the number of scatterings multiplied by the distance between scatterings:

$$|\Delta x| = \sqrt{N} \times v_F \tau \tag{6.13}$$

$$\therefore N = (\frac{\Delta x}{v_F \tau})^2 = (\frac{2\pi}{q v_F \tau})^2 \tag{6.14}$$

$$\therefore \Gamma_q = \frac{\hbar}{t} = \frac{\tau \hbar v_F^2}{4\pi^2} q^2 \;\&\; D = \frac{\tau \hbar v_F^2}{4\pi^2} \chi_0^{-1} \tag{6.15}$$

Thus, the product of the Fermi velocity and the scattering time can be drawn from measurements of Γ_q.

In the compounds most similar to URhGe in terms of magnetic and superconducting properties, UCoGe [120] and UGe_2 [10], non-Landau damping is observed from inelastic neutron scattering, as temperature is tuned across the magnetic transition line. These systems are thought to be controlled by a two-component order parameter, stemming from the interplay of localised and itinerant electrons. The localised electrons contribute to long-range order, like in an RKKY-type system, and also to a static susceptibility above T_{Curie}. Mineev argued [114] that the q^2-dependence of γ_q only shows significance above a certain range of q. As the localised electrons contribution to $S(q,\omega)$ dominates, which leads to spin not being conserved by those electrons, then as $q \to 0$, γ_q can remain finite. Shown in Figure 6.4 is an example of this, being the results of triple-axis neutron scattering on UGe_2 at zero pressure [10]; the values for γ_q are displayed alternatively as $\chi(q)\Gamma_q$, being equal in the approach detailed here. The q-dependence of γ_q is found to be fairly flat, with the error bars shown encompassing the possibility for a full straight line intersecting the γ_q axis at a value of 0.70 μeV, for a susceptibility in *cgs* units. The inset plot shows the temperature dependence of γ_q for a particular value of $q = 0.04$ r.l.u, reducing significantly below the Curie temperature of UGe_2.

In the rest of this chapter, the results from performing small angle neutron scattering (SANS) upon a sample of URhGe are presented. Also shown are simulations of the scattering, built from a model that quantifies the magnetic fluctuations associated with the phase transition into ferromagnetism. The form of the coupling between electrons within a magnetisation fluctuation is inferred from these results, clarifying further what is already known from heat capacity measurements on URhGe. Two slightly different approaches of applying these simulations to the data are shown, the latter accounting for lower sample quality that the former assumes to be perfect.

6.2 Equipment setup

The experiment was performed on beamline D33 at the ILL, Grenoble. The source of neutrons is a 10 kg core of highly enriched uranium, moderated by heavy water. This produces a flux of neutrons that are fed in various directions, the choice of which depends on whether hot or cold neutrons are required; a core of Graphite set to 2900 K bombarded with the neutron flux results in hot (fast) neutrons, and

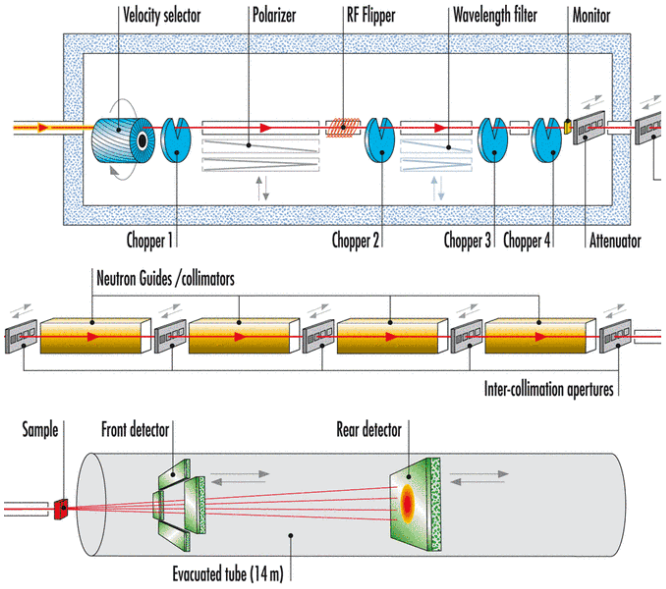

Figure 6.5 *Schematic of the path of neutrons from source to detector; the choppers and polarisers were not used in this case, as time-of-flight methods were unnecessary. The long evacuated tube inside of which lie the detectors is shown at the bottom.*

a 20 K sphere of Deuterium leads to the cold neutrons used in this experiment. Depending on the rotational speed and tilting angle of the velocity selector relative to the incident neutron-beam direction, a mean wavelength between 4.5 and 40 Å, with wavelength resolution $\delta\lambda/\lambda$ around 10% (full width at half maximum), can be selected. In the pre-sample neutron path, a series of apertures of diameter 4 mm collimates the beam. The full setup of the beamline is shown in Figure 6.5. In the lower section is shown two sets of detectors, four front and one rear. The front detectors only show high-q scattering, irrelevant for this experiment. For the rear detector, a distance of 2.3 m was chosen, generally quite a short distance in SANS usage. The phenomena observed are for such low energies that the flux of critical scattering was only detectable at this distance, after trying distances of 8-12 m. A pixel is defined as the crossing point between horizontal and vertical tubes containing ^{3}He, and the charge division across the tube is determined by the encounter of a neutron. The spacing between the tubes determines the size of the pixels, resulting in those horizontal being 2.5 mm long, and 5 mm tall. Thus, this forms an array of 128 x 256, allowing a more detailed coverage of horizontal scattering.

In order to capture enough data to see any critical scattering, the beam is inflicted upon the sample for 90 minutes in each of the points of the phase diagram to be

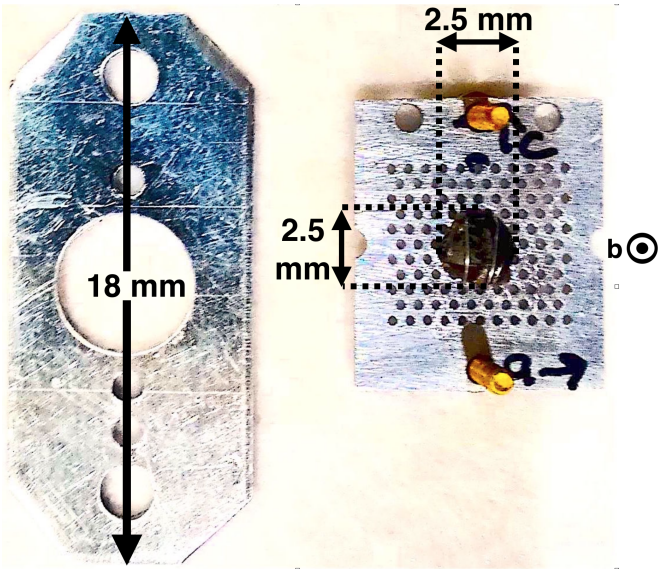

Figure 6.6 *Image of the URhGe sample secured to an aluminium sample holder, and aluminium support bracket for mounting to the mixing chamber of the cryostat. Not shown are small cadmium plates that absorb neutrons before they scatter off the aluminium mounts themselves. Sample's crystal orientation axis a, b, and c are shown.*

investigated i.e. along the Curie line at various values of external magnetic field. Thus, the total experiment lasted a full week, including overnight runs.

The sample was mounted into the beamline's view by attaching it to the aluminium plates shown in Figure 6.6, and mounting that onto an aluminium cup shown in Figure 6.7. This cup is placed in the neutron beam, housed within a vacuum. The design of this evacuated volume decreases time wasted in breaking the vacuum to replace samples, built by Prof. E. Blackburn and colleagues from the University of Birmingham [121].

The magnet used was a standard superconducting coil, aligning the field direction along the axis of the beam. By aligning the *b*-axis of the sample along the same axis, as shown in Figure 6.1, then the moment-rotation at 4 K, 12 T is accessible.

Once the data are collected, corrections are performed; normalisation to the incident beam monitor counts, a correction for the planar geometry of the sample (quantified by the solid angle for each pixel), and further corrections related to sample transmission, background scattering, and detector efficiency.

For analysing the scattering data, a mask is applied over the central few pixels.

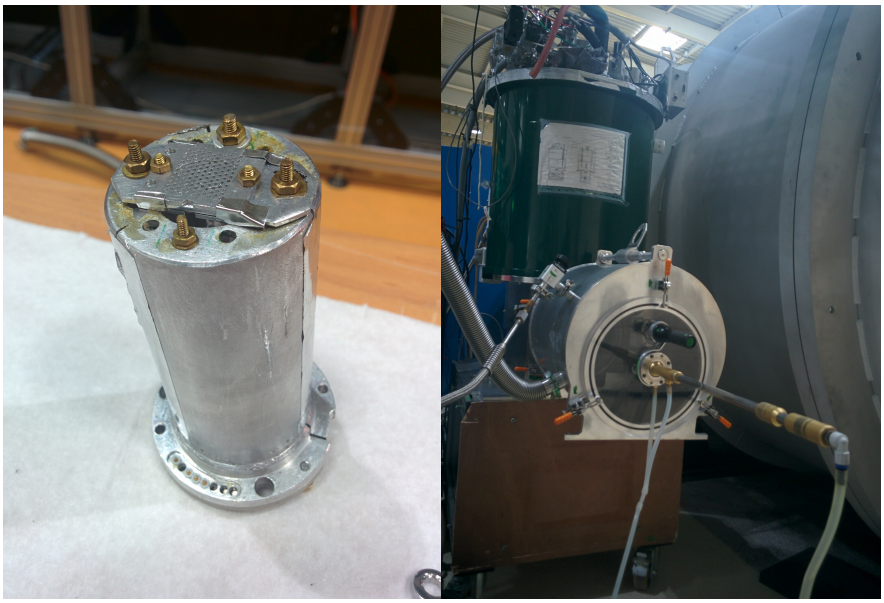

(a) **(b)**

Figure 6.7 *(a) Sample mounted to aluminium cup for insertion into evacuated environment, shown in (b). A manipulable arm protrudes out of the vacuum can; this allows the movement of samples in and out of the neutrons beam/magnet centre, without breaking the vacuum. In the background in green is the main body of the cryostat used.*

The function of the mask is to block out those detected points that correspond to neutrons that have not scattered with the sample, passing straight through instead. Their intensity is significantly higher than any of the scattered neutrons' intensity, and so must be blocked out to see any of the required data. A square shape, rather than circular, was chosen. This is due to the process of applying a mask within Matlab, which is achieved by multiplying a null matrix by the data, both of which are two-dimensional arrays. The mask was made as small as possible such that it didn't block out any significant scattering at the lowest q-values, but large enough to block out all of the straight-through neutron beam. The mask used was of size 32 $\times$ 32 pixels, which is to say the central $\frac{1}{8} \times \frac{1}{8}$ of the total detector size, or roughly 0.09Å$\times$ 0.09Å. This is the mask featured in Figures 6.8 and 6.11.

6.3 Results

6.3.1 Zero field

First, the scattering events collected are shown. In Figure 6.8 is the scattering collected upon the detector for the sample at 9.4 K, 0 T, with a background of scattering at 25 K, 12 T removed; this process results in negative values for the intensity. Over the small q-range available in these conditions[1], there is some increase of scattering along the vertical axis. The extent of the increase of scattering is visible near the top and bottom of the mask applied, and to a weaker degree across the whole q-range shown up until around $|q| \sim 0.15$ Å^{-1}. This is treated as scattering from spin fluctuations along the magnetic easy axis, being the c-axis. Scattering is from moments perpendicular to the scattering plane, which in this case are the a axis and c axis, and so for the magnetisation aligning with either b or c, scattering will be visible either horizontally or vertically in significance, respectively.

As the conditions inflicted upon the sample were changed such that one is effectively moving along the Curie line, then given that this line represents a transition between two magnetic states, then these critical fluctuations are expected to continue to occur. The rotation of the moment from pointing along the c to the b axis would also result in a shift of the critical scattering orientiation, from being along the vertical to circularly symmetric about the detector plane, is the scattering follows the moment direction. The most controversial outcome of this experiment is that the critical scattering was not detected at any field values above 1 T. This will be discussed after the results are presented fully.

Shown in Figure 6.9 are the range of data taken at 0 T, where radial averages for each value of $|q|$ result in this one-dimensional representation. This reduces the size of the data for each temperature and field down enough to allow fitting to effectively take place. This was generated in GRAS$_{ANS}$P, the Matlab interface specifically built for SANS experiments, written by C. Dewhurst and colleagues at the ILL, Grenoble [122]. This was done by drawing arcs of 45°upon the two-dimensional detector image, symmetric about the vertical. Arcs of constant $|q|$ are extracted, from 0.035 Å up to 0.15 Å, and the values for the intensity averaged,

[1] In other types of neutron experiment, like triple axis spectroscopy, the q-range accessible is of the order of at least 1 Å with a resolution generally of 10%.

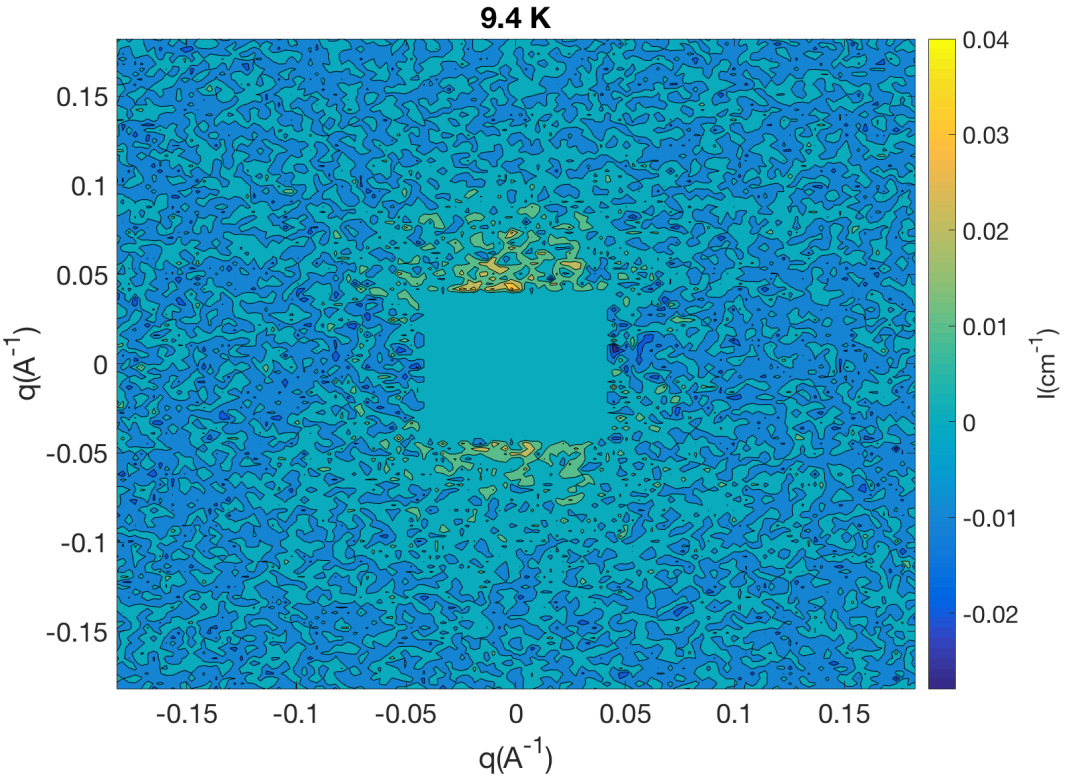

Figure 6.8 *Critical scattering from magnetic fluctuations at a temperature of 9.4 K, over a small range of scattering vector q. Detector distance is 2.8 m, incoming neutrons are of wavelength 4.77 Å, and a background of scattering at 25 K, 0 T has been removed. The vertical and horizontal directions correspond to the a and c axis of the sample, respectively. A mask is applied in the centre, removing any direct neutrons that passed through the sample unperturbed. An increase of scattering in the vertical corresponds to coherent scattering from fluctuations in URhGe along the c axis.*

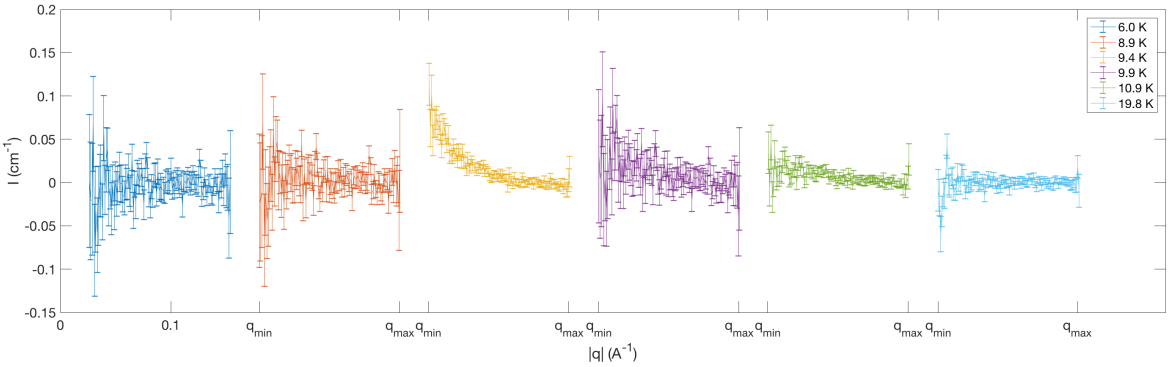

Figure 6.9 *$|q|$-space radial averages of the scattering across all temperatures encountered in zero field. Each scattering event at each temperature is juxtaposed, such that the q-axis spans $q_{min} \rightarrow q_{max}$ repeatedly, where $q_{min} = 0.02$ Åand $q_{max} = 0.15$ Å, the former defined by the mask used.*

resulting in Figure 6.9.

As the temperature passes 9.4 K, being close to T_{Curie}, the rise in critical scattering is clear; a rise in intensity as $q \rightarrow 0$ indicates the low-energy phenomena expected from a ferromagnetic fluctuating system. There is some residue of this behaviour up to 10.9 K, but above that and below 9.4 K, flat scattering ensues. The error bars are larger at minimum $|q|$, due to the significantly smaller number of possible $|q|$ states available to average over, compared to when scattering is collected further out along the detector.

6.3.2 Finite field

In Figure 6.10 the phase diagram of URhGe is shown, adapted from [123]. The detector images created from scattering are placed at a point on the diagram that correspond as-close-as-possible to the experimental conditions inflicted at the time. All scattering shown has been normalised relative to the maximum and minimum of the 0 T data, to see the dominant size of the critical scattering. This was done through the following transformation.

$$s_{normalised} = \frac{(s - s_{max.0T}) - (s - s_{min.0T})}{s_{max.0T} - s_{min.0T}} \tag{6.16}$$

where s is the scattering data. Only the 1 T data shows any reminiscent critical scattering at low-q, whereas the 6 T and 12 T lose any stand-out features, instead

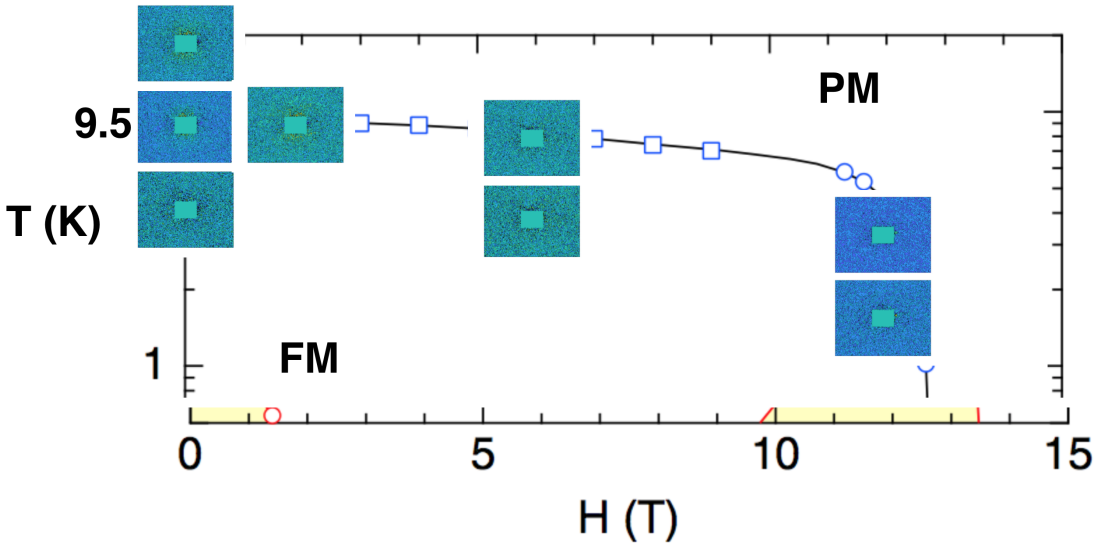

Figure 6.10 *A summary of the scattering events taken, placed in their appropriate place in the phase diagram of URhGe depending on the conditions inflicted. The images are shown in more detail with the colour scale in Figure 6.11.*

displaying flat scattering, albeit at different scales of intensity; whether this is significant or not has not been pursued, but the similar amounts of scattering time given to each event suggest that the origin of this difference can be found in sample alignment, or a lack of fluctuations at 12 T, 4.1 K.

A more detailed image of the effects of field are shown in Figure 6.11, all normalised in the same way as above. The critical scattering above and below the central mask is not observed once a field of 6 T is applied; some non-symmetric points of high intensity are discarded as being due to the direct beam. The critical scattering at zero field is significantly higher than the scattering at all other q, and that significance is reduced in the 1 T data.

6.4 Simulations

For an unpolarised plane-wave beam incident upon a body experiencing ferromagnetic fluctuations, the cross-section per sample volume per solid angle Ω and energy E of neutrons scattered from some initial momentum $\hbar k_i$ to final value $\hbar k_f = \hbar(k+q)$ and energy increase $\hbar\omega$ is expressed [119] as

$$\frac{d^2\sigma}{d\Omega dE} = \frac{k_f}{k_i}\frac{4}{\pi}\frac{\mu_0}{4\pi}\left(\frac{m_n\mu_n}{\hbar^2}\right)^2\left(\delta_{\alpha,\alpha'} - \hat{Q}_\alpha\hat{Q}_{\alpha'}\right)|F_Q|^2\frac{\chi''_{\alpha\alpha'}(q,E)}{1-e^{-\beta E}} \quad (6.17)$$

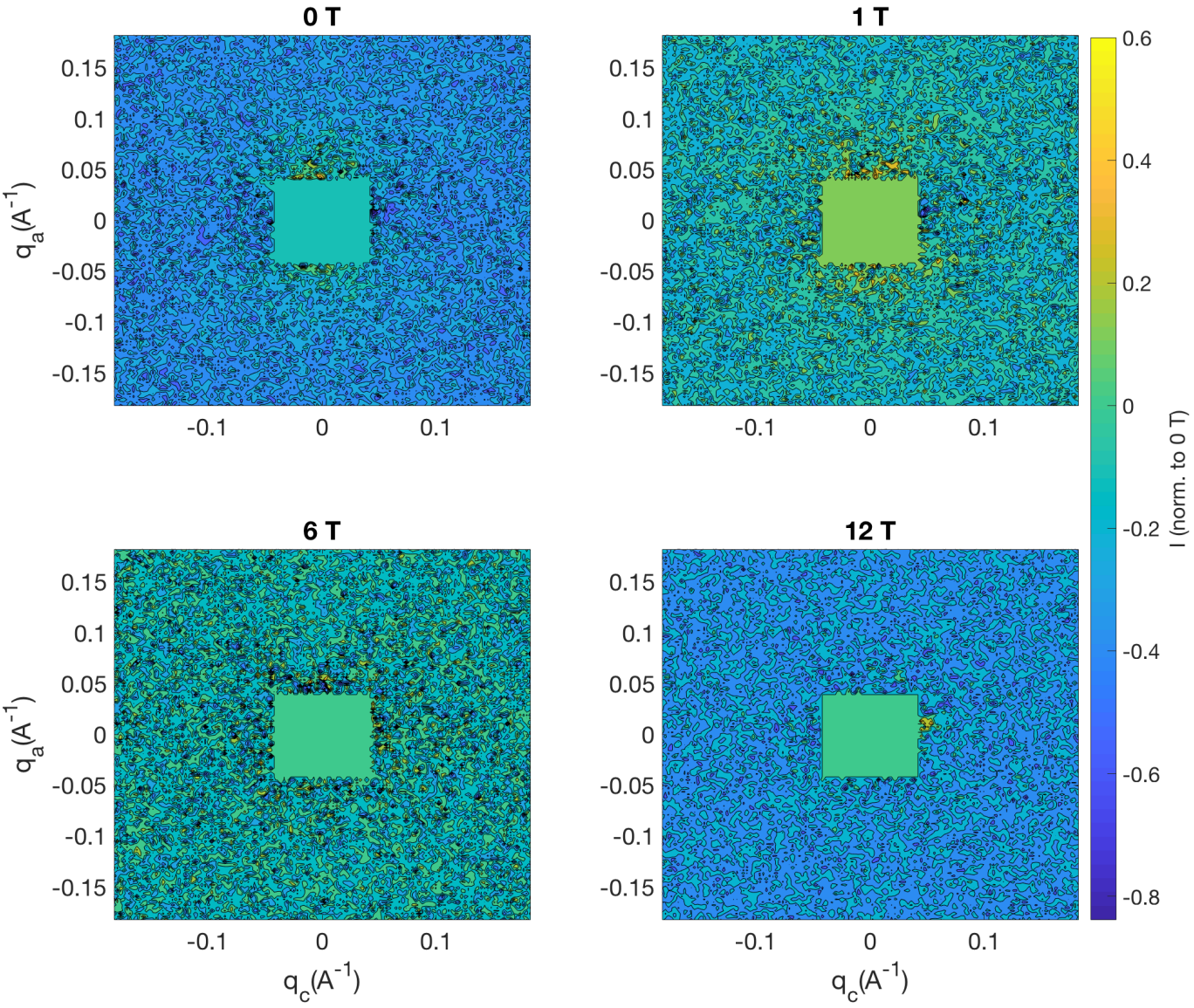

Figure 6.11 *Neutron scattering minus a 25 K, 0 T background, with a detector distance of 2.8 m, incoming neutron wavelength 4.77 Å. The vertical and horizontal axes correspond to q_c and q_a, corresponding to the c- and a-axes. The middle square represents a mask that cuts out any of the neutron beam not scattering off the sample, thus making the sample scattering statistically significant. The temperatures shown are as close to $T_{Curie}(B)$ as was possible in the experiment, being 9.5 K, 9.54 K, 7.9 K, and 4.1 K. For 0 T and 1 T, there is visibly more scattering above and below the mask; this effect is suppressed by field. The difference in the average colour between 6 and 12 T is treated as a statistical effect, where filtering the image into worse resolution would confirm this.*

where m_n is the neutron mass, μ_n the neutron magnetic moment, $|F_Q|^2$ the magnetic form factor, $\chi''_{\alpha\alpha'}(q,E)$ the imaginary part of the magnetic susceptibility, and the exponential in the denominator is the Böse factor, representing occupation of Böse states within the sample. The factor in brackets, $\left(\delta_{\alpha,\alpha'} - \hat{Q_\alpha}\hat{Q_{\alpha'}}\right)$, represents a multiplicative factor that is maximum when scattering perpendicular to the magnetic axis. The factors α and α' represent cartesian directions.

Dissipative effects are represented by $\chi''_{\alpha\alpha'}(q,E)$, and in the conditions determined by small scattering angles and low energies, the main contributions to it are spin and orbital moment fluctuations. This can lead to approximations for $\chi''_{\alpha\alpha'}(q,E)$ in terms of Γ_q, the effective relaxation rate. Following [124], a re-expression of the full scattering cross section in terms of Γ_q, while keeping the q-dependence generic as explained in Chapter 6.1, leads to the following expression for the intensity of scattering, in SI units.

$$\begin{aligned}\frac{d\sigma}{d\Omega} &= -\frac{\mu_0\mu_n^2}{2\pi^2}\int_0^\infty dk_f \frac{k_f\left(k_i^2-k_f^2\right)}{1-e^{-\beta\frac{\hbar^2}{2m_n}(k_i^2-k_f^2)}}\times ... \\ &[\quad \left(1-\frac{\left(k_f\cos(\theta)-k_i\right)^2}{q^2}\right)\frac{\gamma_{q,b}}{\left(\frac{\hbar^2}{2m_n}\left(k_i^2-k_f^2\right)\right)^2+\gamma_{q,b}^2\left(\chi_0^{-1}+c_bq^2\right)^2} \\ &+\quad \left(1-\frac{\left(k_f\sin(\theta)\cos(\phi)\right)^2}{q^2}\right)\frac{\gamma_{q,c}}{\left(\frac{\hbar^2}{2m_n}\left(k_i^2-k_f^2\right)\right)^2+\gamma_{q,c}^2\left(\chi_0^{-1}+c_cq^2\right)^2}]\end{aligned} \tag{6.18}$$

This is the equation from which simulations are built to compare to the scattering observed. The two terms within the square brackets correspond to scattering from moments along the b-axis and c-axis, respectively. The origins of θ and ϕ are shown in Figure 6.1, as is the sample geometry relative to the neutron beam. Thus, as ϕ approaches $\pi/2$, corresponding to the vertical axis, the second term starts to take value due to the prefactor $\left(1-\frac{k_{f\cdots}}{q^2}\right)\to 1$. From the physics of URhGe, only moments along the c- and b-axes are considered, i.e. when $\alpha\alpha' = bb$ & cc.

How this equation is used is as follows: the integral is calculated for some given values of γ_α, c_α, and $\chi_0^{-1}(T)$ at which the data was collected; the latter parameter is discussed more below. The resulting intensity will cover the full possible range of k_f, being the final momentum neutrons posses after scattering with the sample - most of the contribution to this integral will come from values of k_f similar

to k_i, the initial momentum of the neutrons, as the denominators will diverge. Then, this is fit to the data and some resulting value of the error is calculated, quantified in a χ^2. After enough iterations, the best-fit values for γ_α and c_α are found. The results for this method are shown below.

However, the quantity that requires forethought is the inverse static magnetic susceptibility, χ_0^{-1}; this is covered in section 6.1.3. Taken from a Curie-Weiss model, this has a temperature dependence that is reflected in the correlation length, such that the product of the two produces a temperature-independent quantity, being c_α. This means that a single value of c_α will be fit to the whole range of temperatures encountered, but through the use of $\chi_0^{-1}(T)$, the values for $\xi_\alpha(T)$ are found. At the Curie temperature, $\xi_\alpha(T_{Curie})$ is expected to diverge, enforced by $\chi_0^{-1}(T_{Curie}) = 0$. Thus, the fitting is therefore very sensitive to the exact value of T_{Curie}, which can vary with sample quality, or owing to the quality of the thermometer calibration. Thus, a second method of allowing this temperature to vary is also tried, with those results also shown below.

6.5 Non-Landau and Landau model

6.5.1 Results for T_{Curie} fixed

Shown in Figure 6.12 are the results of fitting to the azimuthally-averaged data, for the non-Landau model of $\gamma_q = \gamma$. This is displayed in the form of a three-dimensional plot where the third axis is non-linear temperature. Also shown is the resulting correlation length $\xi_c(T)$ of the magnetic fluctuations along the c-axis, calculated from values of c_c inferred; γ_b and c_b are fixed at zero due to the expectation of the system being magnetically aligned along the c-axis.

The energy scale of the magnetic fluctuations is found to be 572.43 ± 36.2 μeV, a relatively high value compared to that for UGe_2, being 9.67 μeV in SI units [10]. This value and corresponding error was obtained through the Matlab routine "lsqcurvefit" which gives the mean and variance. More will be said about this in the discussion.

The results of fitting Landau-damping and q^2-damping to the data are shown in Figure 6.13, as is the constant-γ model. Away from T_{Curie}, all models do not

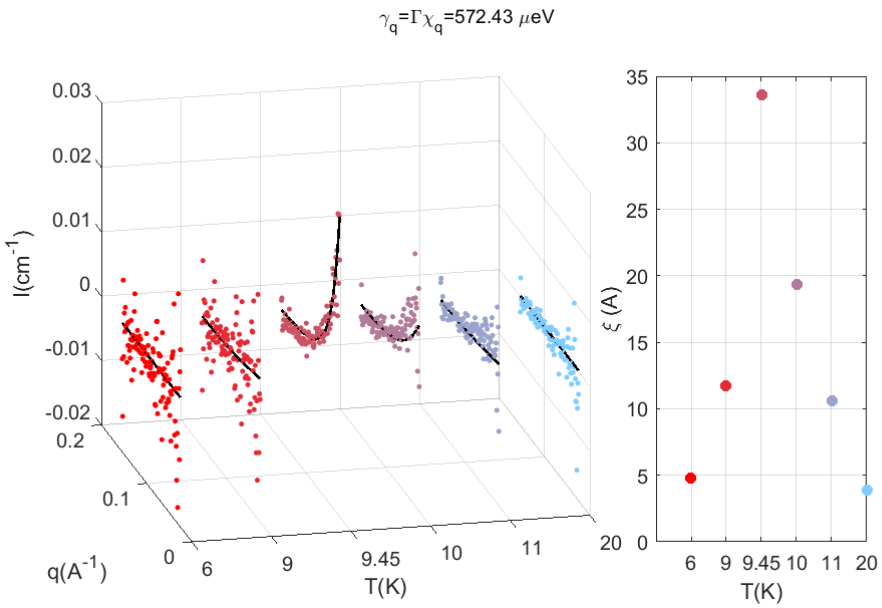

Figure 6.12 *The zero-field data and fits are shown for the constant γ_q model, noting the non-linear temperature axis. The colour changing from red to blue corresponds to data of higher temperature, as also shown in the right-hand plot of the temperature dependence of the correlation length; the lines representing the fits remain black.*

differentiate between one another, mostly due to the flat scattering presenting no features to allow the different relaxation rates to display any peaks. Near T_{Curie}, however, these models do adhere to the rising intensity. Corresponding values for ξ_c are of the order found beforehand, being around 35 Å$\pm$ 4 Å, but the values for γ' differ significantly. This is somewhat expected, due to the change in units: for $\gamma_q = \gamma' q$, $\gamma' = 0.15$ neV.Å. For $\gamma_q = \gamma' q^2$, γ'=0.22 neV.Å^2. However, the units of Γ_q remain as energy, when γ' is multiplied by the corresponding q-dependence.

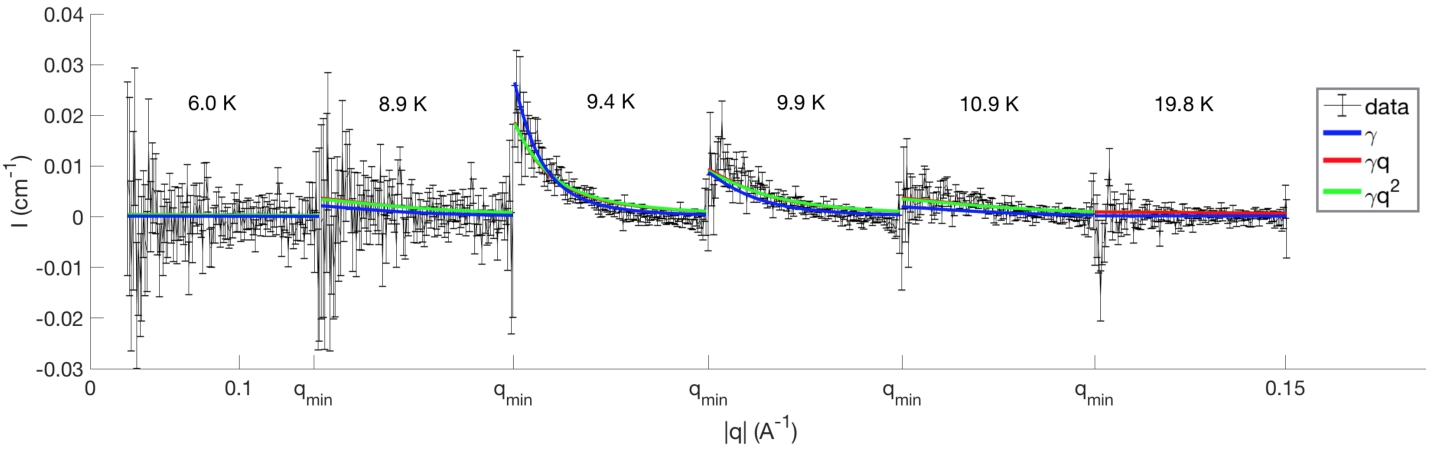

Figure 6.13 *For fixed T_{Curie}, the three proposed models are fit to the radial-averaged SANS data. In blue, red, and green respectively are the constant-γ, ballistic-Landau damping, and diffusive-Landau damping models. Although fairly similar away from T_{Curie}, the models start to differ at 9.4 K and 9.9 K, with the constant-γ model prevailing. The q-axis follows the same rule as that found in Figure 6.9.*

Table 6.1 *Full results of fitting to SANS data with fixed T_{Curie}, giving rate of relaxation and correlation lengths for both crystallographic axis. The values for ξ_α are calculated for temperatures close to T_{Curie}.*

	$\gamma_q \sim$ const				$\gamma_q \sim q$				$\gamma_q \sim q^2$			
	$\gamma'_b(\mu\text{eV})$	$\gamma'_c(\mu\text{eV})$	ξ_b (Å)	ξ_c (Å)	$\gamma'_b(\mu\text{eV.Å})$	$\gamma'_c(\mu\text{eV.Å})$	ξ_b (Å)	ξ_c (Å)	$\gamma'_b(\mu\text{eV.Å}^2)$	$\gamma'_c(\mu\text{eV.Å}^2)$	ξ_b (Å)	ξ_c (Å)
0 T	0	572.43	0	39.73	0	0.182	0	41.11	0	0.223	0	43.58
1 T	∼0	338.17	93.85	69.87	∼0	0.000861	0	64.14	∼0	0.000577	0	49.70
6 T	0.068	900	136.05	123.00	2×10^{-7}	3.1×10^{-6}	150.52	122.75	8.9×10^{-6}	13.5×10^{-6}	170.29	116.25
12 T	50.35	∼0	39.19	0	0.000819	∼0	54.35	0	0.00223	∼0	52.70	0

6.5.2 Results for varying T_{Curie}

"Brute-force" approach to fitting

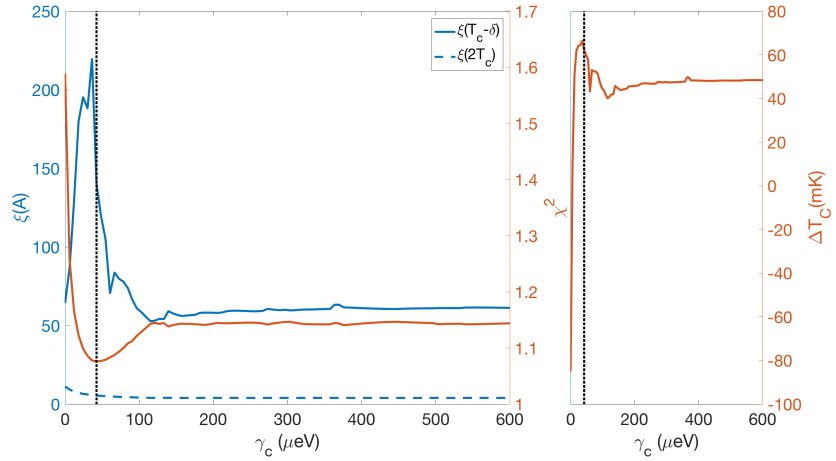

Figure 6.14 *The results of fixing γ_c to be a variety of values, while fitting the data to the same model as in equation 6.18, with the extra step of allowing T_{Curie} to vary. The left-hand plot shows how the correlation length changes at $T_{Curie} - \delta$ (a small parameter) and $2T_{Curie}$, in blue and dashed blue respectively, and $\chi^2(\gamma_c)$ in orange. The right-hand plot shows the results found for ΔT_{Curie}. A black dashed line corresponding to χ^2_{min} is on both plots. The span of γ' covers both the values found previously, and those that correspond to temperatures in the mK range.*

The above methods rely upon the Matlab function "lsqcurvefit", which uses the method of minimising the area of squares between the data and calculated fit. Some skepticism was employed in the results, due to the large difference with the values of γ_α found for UGe_2. Thus, fixing one fit parameter, monitoring the resulting χ^2, and then shifting the value of that fixed fit parameter and repeating leads to a set of values for γ_α and c_α that are known to satisfy the system to varying levels of quality. Thus, by allowing γ_c to vary between 0.1 μeV and 600 μeV, the results found are shown in Figure 6.14.

In addition, due to large amount of sensitivity on temperature for both correlation length and static susceptibility, then the value of T_{Curie} for the sample used is allowed to vary, up to ± 0.5 K. This can account for the varying sample quality that naturally arises out of the difficulties in sample growth. Due to a lack of thermodynamic or transport measurements, the accuracy of the Curie temperature cannot at this time be compared to. Additionally, due to the method

of applying this variability, this extra variable can alternately account for errors in the thermometer used within the experiment.

In the left-hand plot is the γ_c-dependence of both the correlation length at two temperatures, and the value of χ^2. One can immediately see that the previously-found value for γ_c of 572.43 μeV is in a large plateau-region of χ^2, such that there isn't significant difference between roughly 150 μeV and 600 μeV. However, this does not explain why the previous method did not arrive at the clear χ^2-minimising value of 44.50 μeV, indicated by the black-dashed line. This is an order of magnitude closer to that for UGe_2, indicating the relevance of the model. However, the amount by which the Curie temperature shifts must be taken into consideration; the right hand plot in Figure 6.14 shows the γ_c-dependence of this, taking a value of around 60 mK at the critical point. This is a shift of about 0.6%, so considered small enough to be within the bounds expected for typical sample-quality variation. The full set of results from above process is shown in Table 6.2, where the values chosen are for where there is a minimum in χ^2.

Reasons for how the matlab procedure fails include the use of too many fit variables. This is a common problem, where optimising even four variables becomes a processor-heavy process. Additionally, the order in which the program varies a fit variable can result in differing results. This was not experimented with due to time restrictions.

The rate of relaxation for UGe_2, as stated previously, is measured to be 9.67 μeV. To see if this possible candidate value is plausible within these measurements, then the error and temperature shift should be not outside the realms of reality. The corresponding values of χ^2 and ΔT for this γ' are 1.21 and 29 mK respectively, both well within reasonable limits. Thus, in summary, a reliable value for γ' is not extracted from these measurements, but rather a range of candidate values that correspond highly with that found for the comparable material, UGe_2. From this point, the value of γ' will be fixed at 44.5 μeV, and the analysis will concentrate on the value of c, the magnetic stiffness parameter.

Table 6.2 *Full results of fitting to SANS data with variable T_{Curie}, giving rate of relaxation γ_q and stiffness parameter c_α for both crystallographic axis. A reduction/growth of γ_c/γ_b is observed for the constant-γ_q model as field is increased, coinciding with the rotation of the magnetic moment. This is somewhat reflected in the alternative models.*

	$\gamma_q \sim$ const				$\gamma_q \sim q$				$\gamma_q \sim q^2$			
	$\gamma'_b(\mu\text{eV})$	$\gamma'_c(\mu\text{eV})$	$c_b(\text{Å}^2)$	$c_c(\text{Å}^2)$	$\gamma'_b(\text{neV.Å})$	$\gamma'_c(\text{neV.Å})$	$c_b(\text{Å}^2)$	$c_c(\text{Å}^2)$	$\gamma'_b(\text{neV.Å}^2)$	$\gamma'_c(\text{neV.Å}^2)$	$c_b(\text{Å}^2)$	$c_c(\text{Å}^2)$
0 T	0	44.50	0	2019.76	0	0.01	0	2656.60	0	0.51	0	2141.92
1 T	0	9.18	0	4224.05	0	0.13	0	9675.00	0	0.46	0	1903.25
6 T	0	2.03	0	2015.51	$\sim$0	7.17	0	1387.57	$\sim$0	0.01	0	9088.71
12 T	25.26	8.23	9340.93	1886.49	0.01	10.0	9875.16	1981.36	0.11	9.74	9999.99	1993.01

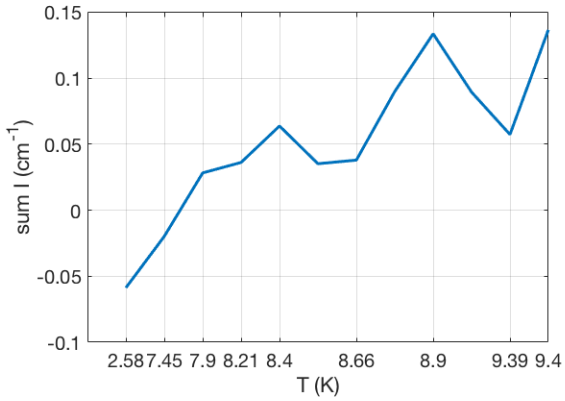

Figure 6.15 *The sum of scattering collected at a variety of temperatures (non-linear scale), with a field applied of 6 T. The scattering at $T_{Curie} \sim 8.4$ K is not significant across the temperature range.*

6.6 Discussion

Data at Field

The data at 6 T is generally lacking in distinct features to allow fitting to produce significant results for the values of rate of relaxation, and magnetic stiffness. In Figure 6.15 is shown the temperature dependence of the sum of intensity, $\sum I(q)$. The Curie temperature under a field of 6 T is expected to be 8.4 K, where the increase in $\sum I(q)$ is not significant when compared to the rest of the data. The temperature control could well be unstable enough to give an offset of 0.5 K, but given the analysis done previously in calculating the ΔT needed to fit the 0 T data, this seems unlikely. In terms of fitting to $I(q)$, this amounts to effectively fitting to the tails of possible peaks found in the beam stop; any scattering variations adds enough ambiguity to render any conclusions from fits inconclusive. Thus, this and the 12 T data is disregarded when making further calculations.

Magnetic Stiffness Field Dependence

The parameter c_α changes with field. From Figure 6.16 one can see the steady increase of both c_b and c_c as field increases from 0 T to 1 T, in all models applied. This supports the notion of a Lifshitz transition at a field higher than 6 T, which is thought to be expected at the rotation of the magnetic moment. The reason for this is as follows: a Lifshitz transition dictates a change in Fermi surface, which can be quantified by the change in the Fermi wave vector k_F. If that change came in the form of a shrinking of k_F, then this would lessen the range of momentum space in which any magnetic fluctuations exist; if they were to be measured with

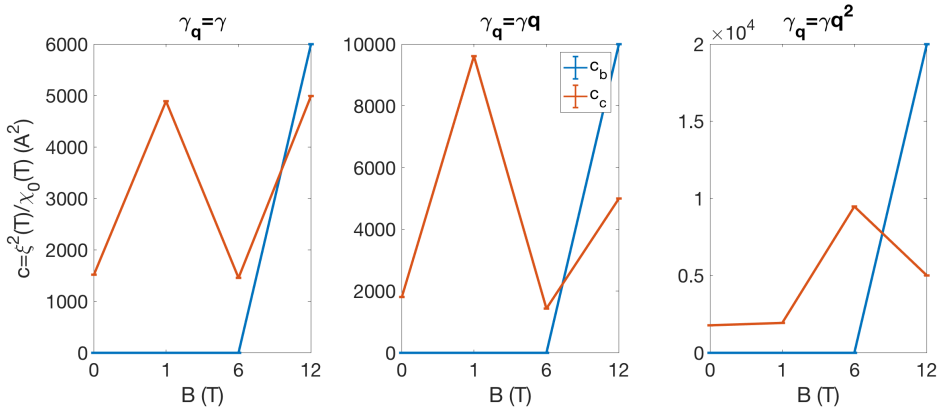

Figure 6.16 *The variation and errorbars of (a) γ_c, and (b) c_b and c_c with field, showing the three models applied. The data for 6 T can be disregarded, but the general trend is indicative of a shrinking Fermi surface; details in the text.*

SANS, then those critical scatterings would be found at values of q smaller than what is detected here. Taillefer and Lonzarich show [119], for parabolic dispersion of E with k, the relation to leading order between $\hat{c} = \sqrt{(c_b^2 + c_c^2)}$ and k_F to be

$$\hat{c} = \frac{\chi_p^{-1}}{12k_F^2} \tag{6.19}$$

The Fermi wave vector can be calculated from this by formulating the Pauli susceptibility [119] as follows.

$$\chi_p = 2\mu_B^2 n(\epsilon_F) \tag{6.20}$$

$$= 2\mu_B^2 . \frac{2\gamma_{hc}}{(\pi k_B)^2} \tag{6.21}$$

$$\therefore \hat{c} = \frac{1}{12k_F^2} \frac{(\pi k_B)^2}{4\mu_B^2 \gamma_{hc}} \tag{6.22}$$

where $n(\epsilon_F)$ is the density of states at the Fermi energy, μ_B is the Bohr magneton, γ_{hc} is the Sommerfeld value from heat capacity, and k_B the Boltzmann constant. An increase in $\hat{c}$ leads to a shrinking of the Fermi wave vector, and therefore magnetic fluctuations. The mask in the centre of the image shown in Figure 6.8 is then effectively blocking off those relevant critical scatterings found at $|q| < 0.05$ Å^{-1}. One could potentially image these by placing the detector further away, but during the experiment it was found that in order to see these low-intensity scatterings, the relatively-short distance of 2.3 m between sample and detector was required.

This proposal of a Lifshitz transition at high fields is supported in measurements of the effective mass via quantum oscillations in electrical resistivity [2]. Here a shrinking of k_F is observed via the measurement of the quasiparticle mass decreasing, although for the magnetic field inflicted $\theta = 10°$ away from the b-axis, as shown in Figure 1.14c. By utilising the relation $v_F = \frac{\hbar k_F}{m^*}$, then the values for Fermi wave vector at high fields are calculated and shown in Figure 6.17, as well as that for the data taken here via equation 6.19.

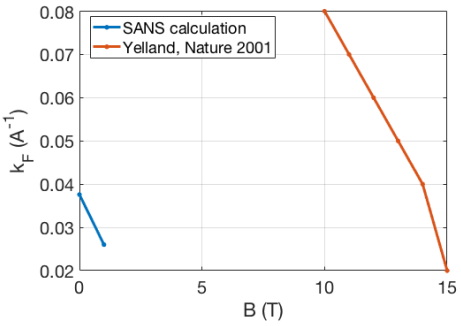

Figure 6.17 *Calculations of the Fermi vector k_F from both the data taken here, and measurements from [2]. Details in the text.*

Neglecting the difficulty in comparing data at different field-values, there is general agreement that there is a shrinking of the Fermi surface as field increases. The values of k_F are of a similar magnitude, although the sensitivity to field is much smaller in the SANS calculations. This could be due to the high-field neutron data not measuring any critical scattering, creating ambiguity in their fit. The shrinking of k_F does also support the changing orbital limit required to induce re-entrant superconductivity, although the disparity with the literature data may well coincide with this particular sample's lack of superconductivity.

Chapter 7

Conclusions and Future Outlooks

The aim of this work was to further establish how superconductivity is mediated in uranium compounds. Both compounds studied, URhGe and UAu_2, exhibit the right crystal structure, inversion symmetry, and f-electron density in order to be superconducting, but to date only the former has proved fruitful in this respect. However, the measurements performed here have helped understand further the fragility of these low-temperature states, especially with respect to the magnetic order present. Additionally, the magnetic fluctuations present in both compounds were studied in order to, in URhGe, see if their energy scale coresponded with any aspect of the superconductivity, and in UAu_2, understand if the presence of a peak in the heat capacity suggested the spontaneous symmetry break of a degenerate pair of ordered states, while already in a magentically ordered state.

The project can be divided into three main parts:

7.1 URhGe Nodal Structure and Magnetic Fluctuations

The measurements of URhGe at zero field lead to results that were not of sufficient quality to justify moving onto applying a magnetic field. However, they did reveal more concerning the ability of poly-crystals to superconduct more-so than single crystals. This result was only possible due to the high level of thermal coupling between thermometer and sample. Within the superconducting phase, the heat

capacity drops in magnitude, and when extrapolated to 0 K, shows some residual entropy. This is also true for previous measurements, implying that scattering between impurities adds entropy. In terms of the nodal structure, the proposed line nodes within the basal b-c plane are thought to open up into two-dimensional regions. This would allow further excitations to bring quasiparticles out into the normal state. Thus, the requirement of single and poly-crystals to be of sufficiently high quality is reinforced, in order to observe any quantum phase transitions expected at high magnetic fields.

Measurements of neutron scattering at small angles revealed the existence of fluctuations at zero field with energy 44.5 μeV, being close to the corresponding energy for $T_c = 0.275$ mK $\rightarrow$ E = 23.7 μeV. The q dependence of this energy was also found, as is the case for UGe_2 and UCoGe, to be non-existent. This implies that both itinerant and localised electrons contribute to the dynamics at play, which should be the case for materials with high densities of f-electrons. Measurements at high field showed no critical scattering, with one conclusion being that the q-range over which there is observed critical scattering reduces down below that measured. This is supported in the values of magnetic stiffness c_α inferred from the measurements.

Future Work

Changes to the heat capacity setup and methods would be made; these are laid out separately below. The presence of a line node proposed by previous measurements would be pursued in heat capacity measurements, revealed by a quadratic dependence upon temperature. The transition of the Curie line from being second- to first-order at fields of 12 T would be pursued in these measurements, visible in the nature of the transition becoming discontinuous. The sample suitable for these measurements would be either grown in house, or requested from colleagues with access to samples of much higher RRR.

The pursuit of observing critical neutron scattering throughout the entire temperature-field phase diagram would entail a combination of the following: running the experiment for longer times, moving the detector further away, and scattering off samples of higher quality to ensure the magnetic structure is as expected. Additionally, since the writing of this thesis, further work has been performed upon UGe_2, in which critical behaviour at much smaller angles than that measured here reveal longitudinal fluctuations arising from $5f$ electrons that

are neither fully local or itinerant [125]. This suggests a route for the exploration of URhGe that will reveal stronger links between these fluctuations and the superconducting coherence length.

7.2 Non-Fermi liquid behaviour in UAu_2

Heat capacity measurements revealed the continuation of non-Fermi liquid behaviour from 1 K down to just above 100 mK, all at zero field. Measurements below 100 mK broke down in reliability, due to an extrapolation of thermal conductivity becoming unphysical. The sample measured was un-annealed, whereas a previously measured sample did unergo annealing, reducing the fraction of impurities present. A peak at 400 mK seen in the heat capacity of the annealed sample was not recreated in the un-annealed sample, although resistance measurements did show some features at that temperature. Thus, the bulk properties of the un-annealed sample would benefit most from annealing, establishing the transition at 400 mK as characteristic of the whole sample.

This non-Fermi liquid behaviour observed is indicative of a proximity to a quantum critical point. The form of fit made to the data, being $C/T = \gamma' \ln\left(\frac{T}{T^*}\right)$ relies upon there being spin fluctuations and a level of interaction between the quasiparticles, defining the breakdown of the Fermi liquid phase. A characteristic temperature T^* and energy scale γ' is suggested by this fit. Although the values are not established as corresponding to confirmed phenomena, the conformity of the data to the form given alone implies the presence of impurities adding entropy that the system must overcome in order to be considered in an ordered phase.

Future Work

As is the case for URhGe, measurements at finite values of magnetic field are the natural next step. These have already taken place upon the same sample reported in this thesis, where the same divergence of the relaxation time is observed at low temperatures, with no signs of a transition all the way down to 70 mK. A transition was found at around 7 T, where ferrimagnetism is enforced, and the heat capacity dropped significantly, implying the release of entropy and establishment of order. The same measurements are planned to be done upon the sample that exhibited the 0 T, 400 mK transition, to understand how the sample quality can affect these impurity effects.

7.3 Heat Capacity Developments

Concerning both the equipment used, and the setup of said equipment, maximising the success of detecting a critical transition was not completely succesful. Making measurements at temperatures as low as 20 mK requires thermometry of high sensitivity and stability. Here it was possible to achieve this down to 50 mK, but not below. Much time was spent experimenting with how wires were connected to the thermometer, hoping to reduce the amount of heat lost via those wires to zero. Due to the time spent on these couplings, whether it was mending a connection that had come apart due to the epoxy disintegrating, or implementing the connection in the first place, a reliable solution that helped gain data at 20 mK was not found. To date, measurements of thermodynamic and transport properties at these temperatures are few and far between, with the most recent being thermal conductivity measurements down to 15 mK [126]. The different components' performance at such temperatures become, in most cases, singular, due to the presence of magnetic impurities. These are the the aluminium oxide substrate of the RuO_2 thermometer, and the thin film that makes up the heater.

Future measurements would consist of a calibration of the RuO_2 thermometers at both low temperature and high field. The heater would be either a strain gauge with known resistance at all temperatures, or a resistor of smaller size than the thermometer. The heater's position would be closer to the sample than that reported in this thesis, to prevent issues of split power and unwanted thermal resistances contributing destructively.

Appendix A

Radioactive Heating of Uranium

Depleted uranium, that which is used in this thesis, is a byproduct of the enriching process for producing uranium of majority-^{235}U, the most unstable isotope. The byproduct is 99.8% ^{238}U [127], and on decaying, emits mostly α particles with an energy of 4.26 MeV/Bq.

There are two ways to derive the heating power of a particular mass of uranium. The first relies on the known rate of decay of one mole, dN/dt, and the half life of ^{238}U, $\tau_{1/2} = 4.5 \times 10^9$.

$$\begin{aligned} P &= \text{energy of decay particle } \times \frac{dN}{dt} && \text{(A.1)} \\ &= 4.26 \text{ MeV/Bq } \times \frac{N_0 \ln(2)}{\tau_{1/2}} && \text{(A.2)} \\ &= 6.816 \times 10^{-13} \text{ J/Bq } \times \frac{6 \times 10^{23}}{238} \frac{\ln(2)}{(4.5 \times 10^9)(\pi \times 10^7)} && \text{(A.3)} \\ &= 8.425 \times 10^{-9} \text{ W/Bq} && \text{(A.4)} \end{aligned}$$

In one second, for one gram of U, this results in 8.425 nW/g. Thus, for a 22.08 mg sample of URhGe, assuming the U makes up one third of the sample, this results in 62 pW.

Alternatively, [127] gives a value of 14.6 KBq/g as the activity for depleted uranium. Thus, by assuming this activity is mostly α particles of the same

energy as in the calculation above, the value for the power is

$$14600 \times 4.26 \text{ MeV} = 9.951 \times 10^{-9} \text{ Bq/g J/Bq} \quad (A.5)$$

$$= 9.95 \times 10^{-9} \text{ J/g} \quad (A.6)$$

For the same mass of URhGe, this gives a heating power of 73 pW.

Appendix B

Heat Flow Modelling

B.1 Heater between Sample & Bath

For a model of the heat capacity addenda where the power sent by the heater will be split between the sample and elsewhere, it is required to know how the relaxation time and thermal conductivity will be affected. These are the quantities calculated from measurements, so their shift due to the presence of extra thermal links not accounted for in an ideal model must be quantified. Thus, the data is determined to be representative, or not, of the sample measured.

Figure 2.6a is representative of the analysis performed here. First, the power sent by the heater is split between the sample and the thermal bath.

$$P = P_s + P_b \tag{B.1}$$

A differential equation that describes heat flow through the sample involves the heat flow to the sample.

$$C_s \dot{T}_s = P_s \tag{B.2}$$

Thus, to find the relaxation time τ and thermal conductivity of the link to the thermal bath, K_b, this equation is to be changed into the form

$$T - \frac{\dot{T}}{\tau} = \frac{P}{C_s} \tag{B.3}$$

In order to do this, the power to the bath and sample must be formulated in terms of the measureable quantities, being the power supplied by the heater P, temperature of the sample T_s. The power supplied to the bath is related to the thermal conductivity of the link between the two. This comes in the form of a gold wire, so this conductivity is represented in terms of its reciprocal quantity, the resistivity $R_g = 1/K_g = 1/K_b$. The temperature of the heater T_k too is important, where here this is represented in terms of the material between heater and the gold wire, being kapton tape.

$$P_b = \frac{T_k}{R_g} \tag{B.4}$$

The power to the sample is related to the temperature difference between heater and sample, as well as the thermal resistivity between the two.

$$P_s = \frac{T_k - T_s}{R_k} \tag{B.5}$$

Inserting one power into the other, by rearranging equation (B.4), results in the power to the sample in terms of the power supplied.

$$\begin{aligned} P_s &= \frac{P_b R_g - T_s}{R_k} && \text{(B.6)} \\ &= P_b \frac{R_g}{R_k} - \frac{T_s}{R_k} && \text{(B.7)} \\ &= (P - P_s)\frac{R_g}{R_k} - \frac{T_s}{R_k} && \text{(B.8)} \\ \therefore P_s &= \frac{PR_g - T_s}{R_g + R_k} = C_s \dot{T}_s && \text{(B.9)} \end{aligned}$$

Rearranging this final equation into the form shown in equation (B.3), one arrives at

$$\begin{aligned} C_s \dot{T}_s &= P\frac{1}{1 + \frac{R_k}{R_g}} - \frac{T_s}{R_g + R_k} && \text{(B.10)} \\ \therefore \dot{T}_s + \frac{T_s}{C_s(R_g + R_k)} &= \frac{P}{C_s(1 + \frac{R_k}{R_g})} && \text{(B.11)} \end{aligned}$$

The relaxation time τ is elongated by the finite resistance between heater and sample, R_k, and the power sent to the thermal bath decreased by the finite ratio R_k/R_g. The combination of these leads to a reduction of the apparant heat capacity, $C_s = \tau/R_g$. The value of R_k/R_g can be calculated, by the following,

noting that C' and P' are the observed values of heat capacity and power delivered by the heater.

$$\begin{aligned} C' = K\tau &= \frac{P'}{\Delta T}\tau \\ &= \frac{P\tau}{\Delta T(1+\frac{R_k}{R_g})} \qquad \text{(B.12)} \\ \therefore \Delta C = C' - C &= \frac{P\tau}{\Delta T}\left(1 - \frac{1}{1+\frac{R_k}{R_g}}\right) \\ &= \frac{P\tau}{\Delta T}\frac{R_k}{R_g + R_k} \qquad \text{(B.13)} \\ \therefore \frac{R_g}{R_k} &= \frac{P\tau}{\Delta C \Delta T} - 1 \qquad \text{(B.14)} \end{aligned}$$

The effects of this are discussed in chapter 4.

B.2 Sample between Heater & Bath

To see what the relaxation time is when the sample is situated between the heater and the bath, the heat flow is modelled as shown schematically in Figure 2.6a. Concentrating on the heat capacity of the sample, rather than that of the thermometer (which has been shown to be comparably negligible), the heat flow follows an equation of the form

$$C_s\dot{T}_s = \frac{T_p - T_s}{R_s} \qquad \text{(B.15)}$$

where C_s is the heat capacity of the sample, T_s is the temperature of the sample, T_p is that of the platform that binds all components together, and R_s is the thermal resistance between platform and sample. Ideally this is zero, but this calculation will show its contribution when finite.

An equivalent of Kirchoff's law for heat flow can be performed here, where the power delivered by the heater is conserved.

$$P_s + P_0 + P_t = 0 = \frac{T_p - T_s}{R_s} + \frac{T_p - T_0}{R_a} + \frac{T_p - T_t}{R_t} \qquad \text{(B.16)}$$

where T_0 is the temperature of the bath, and T_t is the temperature of the thermometer. The goal is eliminate T_p and T_t from the equation for the heat

capacity, and once in the form of equation B.3, extract the augmented relaxation time.

First, substituting for T_p from equation B.15 into equation B.16, one achieves

$$\frac{R_s C_s \dot{T}_s + T_s - T_s}{R_s} + \frac{R_s C_s \dot{T}_s + T_s - T_0}{R_a} + \frac{R_s C_s \dot{T}_s + T_s - T_t}{R_t} = 0 \quad \text{(B.17)}$$

$$C_s \dot{T}_s \left(1 + \frac{R_s}{R_a} + \frac{R_s}{R_t}\right) + \frac{T_s - T_0}{R_a} + \frac{T_s - T_t}{R_t} = 0 \quad \text{(B.18)}$$

Here, two assumptions are made: (a) $T_0 = 0$, the bath temperature is set to zero, without loss of generality, and (b) $T_s = T_t$, the steady-state sample temperature is equivalent to the thermometer temperature. These gives the following

$$C_s \dot{T}_s \left(1 + \frac{R_s}{R_a} + \frac{R_s}{R_t}\right) = -\frac{T_s}{R_a} \quad \text{(B.19)}$$

Thus, by rearranging into a form which resembles the expected main contributor to thermal resistance, R_a, multiplied by a factor, one can see the effect upon the relaxation time to be its elongation.

$$\therefore \dot{T}_s = -\frac{T_s}{C_s R_a \left(1 + R_s(\frac{R_a + R_t}{R_a R_t})\right)} \quad \text{(B.20)}$$

$$= -\frac{T_s}{C_s \left(R_a + \frac{R_s}{R_t}(R_a + R_t)\right)} \quad \text{(B.21)}$$

By setting the ideal conditions, i.e. sample and thermometer are fully thermalised with the platform and thus one another ($R_s = R_t = 0$), one arrives at the original result of the thermal resistance between platform and bath being the only contributor to the relaxation time.

Appendix C

Euler-Bernoulli Theorem for Bending Rods

A model for the forces experienced by a bent solid rod is shown. This was first worked on around 1750 [128], but was applied in large scale to the Eiffel Tower in the 19th century. Here, the copper rods that hold the kevlar wires and ultimately the heat capacity addenda are treated as rods with a geometry shown in Figure C.1b. It is shown that the forces inflicted by the tensioned Kevlar wire do not exceed those needed to irreversibly break the rods.

Define the bending moment $= |\tau|$. When the rod is in equilibrium, the total torque $= 0$. That is to say, the torque applied to the stretched-top-end of the rod balances with the torque experienced by the compressed-bottom-end; see Figure C.1a.

$$0 = -\frac{\partial \tau}{\partial x} dx - F dx \tag{C.1}$$

$$\therefore F = -\frac{\partial \tau}{\partial x}, \text{ and additionally, } \tau = -\int_0^L F dx \tag{C.2}$$

Define the weight, W...

$$W = \frac{\partial F}{\partial x} = -\frac{\partial^2 \tau}{\partial x^2} \tag{C.3}$$

Now if we consider a rod that has a finite 3^{rd} dimension, lets say of length dz, then to calculate the spread of forces along the y-dimension, one must consider the relative radius of curvature for every point along the beam. The difference in

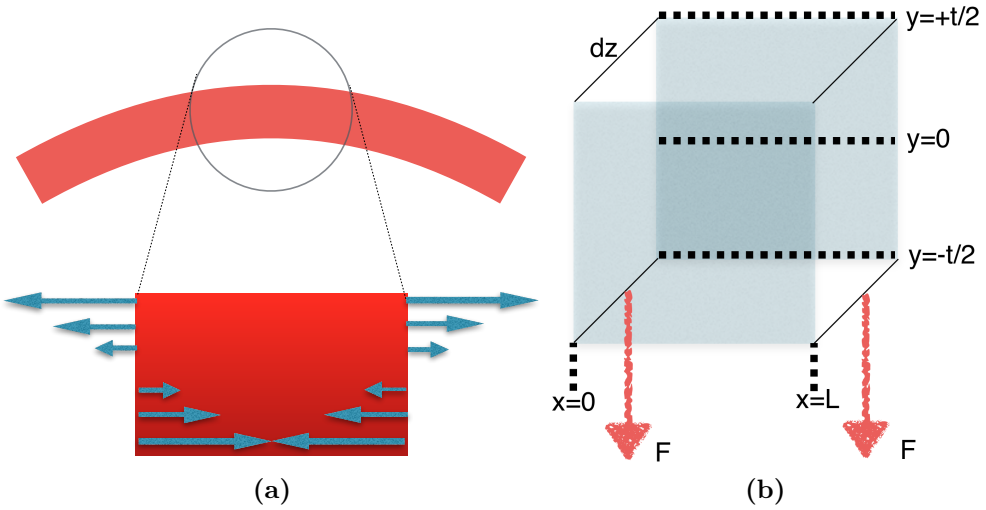

Figure C.1 *(a) Breakdown of forces at play upon a bent rod; the top is tensioned, whereas the bottom is compressed. (b) Dimensionality of beam.*

the relative radius of curvature between the upper-and-lower edges ($y = t/2$ and $y = -t/2$) gives a scale for the difference in torque across the beam.

$$f = E(\frac{(L+y)d\theta - Ld\theta}{Ld\theta}) \tag{C.4}$$

$$= \frac{Ey}{L} \tag{C.5}$$

where E is the Youngs Modulus of the material. Now if we treat the length L as the general radius of curvature, i.e:

$$L = \frac{d^2x}{dy^2} \tag{C.6}$$

then we can quantify the force upon the rod in terms of its dimensions:

$$f = E\frac{d^2y}{dx^2}y \tag{C.7}$$

$$\therefore \tau = -\int_{-t/2}^{+t/2}(ydz)fdy \tag{C.8}$$

$$= -E\frac{d^2y}{dx^2}dz\int_{-t/2}^{+t/2}y^2dy \tag{C.9}$$

$$= -E\frac{d^2y}{dx^2}dz(\frac{t^3}{12}) \tag{C.10}$$

It should be noted that the integral for τ multiplies together the height and depth of the rod, which acts as a geometric factor to scale in the amount of matter that's

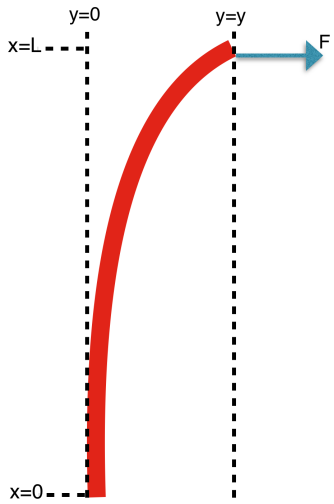

Figure C.2 *How a cantilevered beam reacts to a point force*

experiencing the torque.

Let $I = t^3 dz/12$, and treat this as a geometric factor that can be taken purely from observations.

$$\therefore \tau = -EI\frac{d^2y}{dx^2} \tag{C.11}$$

$$\therefore W = EI\frac{d^4y}{dx^4} \tag{C.12}$$

If we are to gain an equation for the profile of the rod from this equation, then this means integrating up to get $y(x)$, and thus we can expect something of cubic order. An assumption that simplifies things is considering the weight of the rod to be negligible as compared to the magnitude of the forces at play. This is considered valid, due to the weight of the whole copper mount being $\sim$ 100 g, equivalent to just under 1 N.

$$\therefore W = 0, \text{ so } y = A + Bx + Cx^2 + Dx^3 \tag{C.13}$$

The first coefficient A is zero, otherwise the beam would be displaced from the point that it's fixed. If we use previously derived equations, rather than boundary conditions, then we can gain a form for the other coefficients:

$$F = -EI\frac{d^2y}{dx^2}, \ \therefore D = -\frac{F}{6EI} \tag{C.14}$$

$$\tau = EI\frac{d^2y}{dx^2} = EI(2C + 6Dx) \tag{C.15}$$

For this second constraint, we know from the basic mechanics of moments that relative to the end at which the force is applied, one can say $\tau = F(L-x)$, and so for $x = 0$:

$$F(L-x)|_{x=0} = EI(2C + 6Dx)|_{x=0} \quad \text{(C.16)}$$

$$\therefore C = \frac{FL}{2EI} \quad \text{(C.17)}$$

$$\text{Thus, finally we have } y = \frac{F}{EI}(\frac{Lx^2}{2} - \frac{x^3}{6}) \quad \text{(C.18)}$$

$$= \frac{F}{EI}\frac{L^3}{3}|_{x=L} \quad \text{(C.19)}$$

Now we have a handle on relating the forces at play with the required stretching distance. This distance is calculated from a combination of the thermal expansion of Kevlar and its tensile stretching limit from tensioning. These are defined below:

$$L_{Kevlar final} = (2.4\% + 0.049\% + 2.4\%)L_0 \quad \text{(C.20)}$$

$$= 1.04849L_0 \quad \text{(C.21)}$$

$$\therefore F = \frac{3EI}{L^3}y_{max} \text{ where } y_{max} = (1.04849 - 1)L_0 \quad \text{(C.22)}$$

The repeating of the 2.4%, indicative of the length increase from stretching [129], is due to the cooling down of Kevlar causing growth. The size of the growth due to cooling is calculated from the thermal expansion coefficient $\alpha = -2.2 \times 10^{-6}\text{K}^{-1}$, and is negligible compared to that from mechanical stretching.

Below is a calculation of the forces inflicted by a copper rod, of size 2 mm $\times$ 2 mm $\times$ 22 mm, after being strained as modelled in Figure C.2, with L_0 spanning 5 mm and 8 mm. To get a handle on whether the wire shall be stretched to its absolute limit or not, a range of the fractional expansion coefficients are trialled, between 1 and 1.04849. The second plot is for a single fractional expansion, namely the maximum of 1.04849, which shows that even if 7 mm of kevlar wire is used, the forces inflicted by the rod fail to exceed 15 N. This shows that the dimensions of the components used all fall within reasonable bounds, allowing the heat capacity measurements to take place without the threat of any breakages occuring.

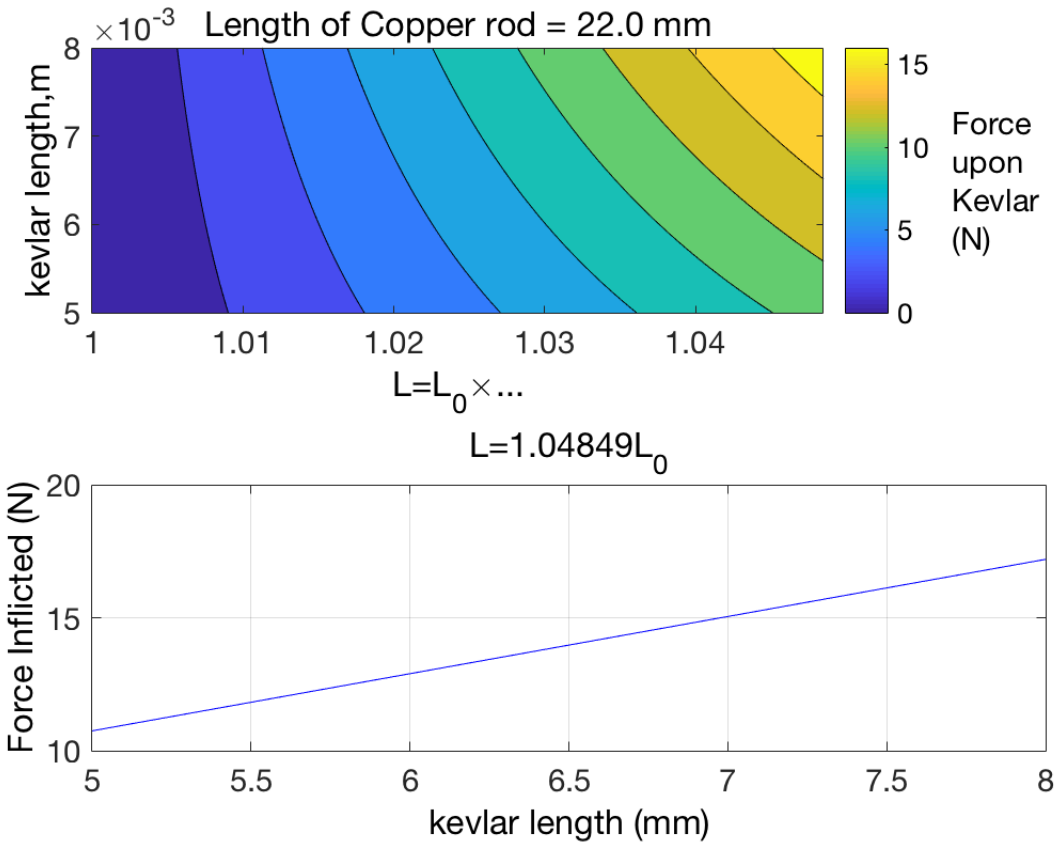

Figure C.3 *Upper: Calculation of forces upon the bent beam, indicated by colour. This is found by spanning the length of Kevlar wire used, and a variable coefficient of expansion as a fraction of the length. Lower: results for* $L=L_0\times 1.04849$*, resulting in a maximum force of 16 N for 8 mm of Kevlar wire.*

Appendix D

Table of Components' Properties

Table D.1 *The dimensions, heat capacities, and thermal conductivities of the main components used in the heat capacity addenda are shown below. Units vary between values due to different conventions across the literature.*

Material	Dimensions/weight	(Specific) Heat Capacity	Thermal Conductivity
Gold	Platform - 3×3×0.1 mm, 1.84×2=3.68 mg Wire - 25 μm diameter, 3 mm length	$11.76 + 0.4245T^3$ mJ/mol.K	1.1091T W/cm.K [96]
Kevlar	20 filaments, 3 mm	-	$3.9 \times 10^{-5}T^{1.17}$ W/cm.K [94]
Silver epoxy	<1 mg	$2.5T + 3.84T^3 - 0.091T^4$ μJ/g.K [100]	0.03 W/m.K [103]
Kapton	0.51 mg, 3×2×0.03 mm	1.09 J/g.K [130]	$\log K = 5.73 - 39.52 \log T + ...$ [131]
RuO_2	1.45×1.27×0.08 mm	$5.7T + 0.001637T^{-2}$ mJ/mol.K [99]	-
Strain Gauge (NiCr)	3.2×2.4×0.1 mm	$a + bT^{-3}$ [98]	-

Bibliography

[1] D. Aoki, A. Huxley, E. Ressouche, and D. Braithwaite, "Coexistence of superconductivity and ferromagnetism in URhGe," *Nature*, pp. 9–12, 2001.

[2] E. Yelland, J. Barraclough, W. Wang, K. Kamenev, and A. Huxley, "High-field superconductivity at an electronic topological transition in URhGe," *Nature Physics*, vol. 7, no. 6792, p. 890, 2011.

[3] N. Mathur, F. Grosche, S. Julian, I. Walker, D. Freye, R. Haselwimmer, and G. Lonzarich, "Magnetically mediated superconductivity in heavy fermion compounds," *Nature*, vol. 394, no. 6688, pp. 39–43, 1998.

[4] P. M. Chaikin and T. C. Lubensky, *Principles of condensed matter physics*. Cambridge university press, 2000.

[5] J. Schmehr, C. O'Neill, D. A. Sokolov, H. Keen, A. Hermann, P. Manuel, T. F. Telling, D. Wermeille, and A. D. Huxley, "Quantum criticality below the Neél temperature in the frustrated heavy fermion magnet UAu_2." unpublished paper, 2018.

[6] J. Custers, P. Gegenwart, H. Wilhelm, K. Neumaier, Y. Tokiwa, O. Trovarelli, C. Geibel, F. Steglich, C. Pépin, and P. Coleman, "The break up of heavy electrons at a quantum critical point," *arXiv preprint cond-mat/0308001*, 2003.

[7] H. v. Löhneysen, T. Pietrus, G. Portisch, H. Schlager, A. Schröder, M. Sieck, and T. Trappmann, "Non-Fermi-liquid behavior in a heavy-fermion alloy at a magnetic instability," *Physical Review Letters*, vol. 72, no. 20, p. 3262, 1994.

[8] V. P. Mineev, "Superconductivity in uranium ferromagnets," *Physics-Uspekhi*, vol. 60, no. 2, p. 121, 2017.

[9] N. W. Ashcroft, N. D. Mermin, and S. Rodriguez, "Solid state physics," 1998.

[10] A. D. Huxley, S. Raymond, and E. Ressouche, "Magnetic excitations in the ferromagentic superconductor UGe_2," *Physical Review Letters*, vol. 91, no. 20, p. 207201, 2003.

[11] C. Kittel and H. Kroemer, "Thermal physics," 1980.

[12] R. Bowley and M. Sanchez, *Introductory statistical mechanics*. Clarendon Press Oxford, 1999.

[13] L. Landau and E. Lifshitz, "Statistical physics," *Course of Theoretical Physics*, vol. 5, p. 230, 1958.

[14] J. C. Slater, "The theory of complex spectra," *Physical Review*, vol. 34, no. 10, p. 1293, 1929.

[15] R. Shankar, *Quantum Field Theory and Condensed Matter: An Introduction*. Cambridge University Press, 2017.

[16] S. Nishizaki, Y. Maeno, and Z. Mao, "Changes in the superconducting state of Sr_2RuO_4 under magnetic fields probed by specific heat," *Journal of the Physical Society of Japan*, vol. 69, no. 2, pp. 572–578, 2000.

[17] E. Hassinger, P. Bourgeois-Hope, H. Taniguchi, S. Rene de Cotret, G. Grissonnanche, M. Shahbaz Anwar, Y. Maeno, N. Doiron-Leyraud, and L. Taillefer, "The break up of heavy electrons at a quantum critical point," *Phys. Rev. X*, vol. 7, p. 011032, 2017.

[18] A. Huxley, P. Rodiere, D. M. Paul, N. van Dijk, *et al.*, "Realignment of the flux-line lattice by a change in the symmetry of superconductivity in UPt_3," *Nature*, vol. 406, no. 6792, p. 160, 2000.

[19] J. Sauls, "The order parameter for the superconducting phases of UPt_3," *Advances in Physics*, vol. 43, no. 1, pp. 113–141, 1994.

[20] M. Tinkham, *Introduction to superconductivity*. Courier Corporation, 1996.

[21] H. K. Onnes, "Further experiments with liquid helium. g. on the electrical resistance of pure metals, etc. vi. on the sudden change in the rate at which the resistance of mercury disappears.," in *Through Measurement to Knowledge*, pp. 267–272, Springer, 1991.

[22] D. Van Delft and P. Kes, "The discovery of superconductivity," *Physics Today*, vol. 63, no. 9, pp. 38–43, 2010.

[23] J. Bardeen, L. N. Cooper, and J. R. Schrieffer, "Theory of superconductivity," *Physical Review*, vol. 108, no. 5, p. 1175, 1957.

[24] F. London and H. London, "Supraleitung und diamagnetismus," *Physica*, vol. 2, no. 1, pp. 341–354, 1935.

[25] J. F. Annett, *Superconductivity, superfluids and condensates*, vol. 5. Oxford University Press, 2004.

[26] D. Fay and J. Appel, "Coexistence of p-state superconductivity and itinerant ferromagnetism," *Physical Review B*, vol. 22, no. 7, p. 3173, 1980.

[27] J. G. Bednorz and K. A. Müller, "Possible high T_c superconductivity in the Ba-La-Cu-O system," *Zeitschrift für Physik B Condensed Matter*, vol. 64, no. 2, pp. 189–193, 1986.

[28] S. Saxena, P. Agarwal, K. Ahilan, F. Grosche, R. Haselwimmer, M. Steiner, E. Pugh, I. Walker, S. Julian, P. Monthoux, *et al.*, "Superconductivity on the border of itinerant-electron ferromagnetism in UGe_2," *Nature*, vol. 406, no. 6796, pp. 587–592, 2000.

[29] M. Sigrist and K. Ueda, "Phenomenological theory of unconventional superconductivity," *Reviews of Modern physics*, vol. 63, no. 2, p. 239, 1991.

[30] C. Nayak, S. H. Simon, A. Stern, M. Freedman, and S. D. Sarma, "Non-abelian anyons and topological quantum computation," *Reviews of Modern Physics*, vol. 80, no. 3, p. 1083, 2008.

[31] J. Jang, D. Ferguson, V. Vakaryuk, R. Budakian, S. Chung, P. Goldbart, and Y. Maeno, "Observation of half-height magnetization steps in Sr_2RuO_4," *Science*, vol. 331, no. 6014, pp. 186–188, 2011.

[32] P. Debye, "Zur theorie der spezifischen wärmen," *Annalen der Physik*, vol. 344, no. 14, pp. 789–839, 1912.

[33] C. Luengo, M. Maple, and J. Huber, "Magnon heat capacity, magnon magnetization and magnetic entropy of the weak ferromagnet UPt," *Journal of Magnetism and Magnetic Materials*, vol. 3, no. 4, pp. 305–308, 1976.

[34] R. De Batist, R. Gevers, and M. Verschueren, "Magnon contribution to the low-temperature specific heat of UO_2," *Physica Status Solidi (b)*, vol. 19, no. 1, pp. 77–88, 1967.

[35] F. Hardy, C. Meingast, V. Taufour, J. Flouquet, H. v. Löhneysen, R. Fisher, N. Phillips, A. Huxley, and J. Lashley, "Two magnetic grüneisen parameters in the ferromagnetic superconductor UGe_2," *Physical Review B*, vol. 80, no. 17, p. 174521, 2009.

[36] R. Joynt and L. Taillefer, "The superconducting phases of UPt_3," *Reviews of Modern Physics*, vol. 74, no. 1, p. 235, 2002.

[37] A. Montorsi, *The Hubbard Model: A Reprint Volume*. World Scientific, 1992.

[38] J. Schmehr, *Incommensurate Magnetism in UAu_2*. PhD thesis, The University of Edinburgh, 2016.

[39] S. Niitaka, K. Yoshimura, K. Kosuge, M. Nishi, and K. Kakurai, "Partially disordered antiferromagnetic phase in Ca_3CoRhO_6," *Physical Review Letters*, vol. 87, no. 17, p. 177202, 2001.

[40] W. Yelon, D. Cox, and M. Eibschütz, "Magnetic ordering in $CsCoBr_3$," *Physical Review B*, vol. 12, no. 11, p. 5007, 1975.

[41] M. Mekata and K. Adachi, "Magnetic structure of $CsCoCl_3$," *Journal of the Physical Society of Japan*, vol. 44, no. 3, pp. 806–812, 1978.

[42] V. Plakhty, J. Wosnitza, N. Martin, Y. Marchi, O. Smirnov, B. Grenier, and S. Gavrilov, "Isostructural transition coupled with spin ordering in $CsCuCl_3$: A spatially frustrated spiral crystal lattice," *Physical Review B*, vol. 79, no. 1, p. 012410, 2009.

[43] O. Trovarelli, C. Geibel, S. Mederle, C. Langhammer, F. Grosche, P. Gegenwart, M. Lang, G. Sparn, and F. Steglich, "$YbRh_2Si_2$: Pronounced non-Fermi-liquid effects above a low-lying magnetic phase transition," *Physical Review Letters*, vol. 85, no. 3, p. 626, 2000.

[44] F. Steglich, P. Gegenwart, R. Helfrich, C. Langhammer, P. Hellmann, L. Donnevert, C. Geibel, M. Lang, G. Sparn, W. Assmus, *et al.*, "Are heavy-Fermion metals Fermi liquids?," *Zeitschrift für Physik B Condensed Matter*, vol. 103, no. 2, pp. 235–242, 1996.

[45] B. Andraka and A. Tsvelik, "Observation of non-Fermi-liquid behavior in $U_{0.2}Y_{0.8}Pd_3$," *Physical Review Letters*, vol. 67, no. 20, p. 2886, 1991.

[46] H. von Löhneysen, "Non-Fermi-liquid behaviour in the heavy-Fermion system," *Journal of Physics: Condensed Matter*, vol. 8, no. 48, p. 9689, 1996.

[47] T. Moriya and T. Takimoto, "Anomalous properties around magnetic instability in heavy electron systems," *Journal of the Physical Society of Japan*, vol. 64, no. 3, pp. 960–969, 1995.

[48] G. Lonzarich and M. Springford, *Electron: A Centenary Volume*. Cambridge University Press Cambridge, 1997.

[49] A. J. Schofield, "Non-Fermi liquids," *Contemporary Physics*, vol. 40, no. 2, pp. 95–115, 1999.

[50] K. Prokeš, T. Tahara, Y. Echizen, T. Takabatake, T. Fujita, I. Hagmusa, J. Klaasse, E. Brück, F. De Boer, M. Diviš, *et al.*, "Electronic properties of a URhGe single crystal," *Physica B: Condensed Matter*, vol. 311, no. 3, pp. 220–232, 2002.

[51] V. Tran, R. Troć, and G. André, "Magnetic ordering in URhSi and URhGe," *Journal of magnetism and magnetic materials*, vol. 186, no. 1, pp. 81–86, 1998.

[52] F. De Boer, E. Brück, V. Sechovsky, L. Havela, and K. Buschow, "UTX compounds in high magnetic fields," *Physica B: Condensed Matter*, vol. 163, no. 1-3, pp. 175–178, 1990.

[53] D. Braithwaite, D. Aoki, J.-P. Brison, J. Flouquet, G. Knebel, A. Nakamura, and A. Pourret, "Dimensionality driven enhancement of ferromagnetic superconductivity in URhGe," *arXiv preprint arXiv:1710.09097*, 2017.

[54] F. Lévy, I. Sheikin, and A. Huxley, "Acute enhancement of the upper critical field for superconductivity approaching a quantum critical point in URhGe," *Nature Physics*, vol. 3, no. 7, pp. 460–463, 2007.

[55] W. Fertig, D. Johnston, L. DeLong, R. McCallum, M. Maple, and B. Matthias, "Destruction of superconductivity at the onset of long-range magnetic order in the compound $ErRh_4B_4$," *Physical Review Letters*, vol. 38, no. 17, p. 987, 1977.

[56] M. Ishikawa and Ø. Fischer, "Destruction of superconductivity by magnetic ordering in $Ho_{1.2}Mo_6S_8$," *Solid State Communications*, vol. 23, no. 1, pp. 37–39, 1977.

[57] D. Moncton, D. McWhan, P. Schmidt, G. Shirane, W. Thomlinson, M. Maple, H. MacKay, L. Woolf, Z. Fisk, and D. Johnston, "Oscillatory magnetic fluctuations near the superconductor-to-ferromagnet transition in $ErRh_4B_4$," *Physical Review Letters*, vol. 45, no. 25, p. 2060, 1980.

[58] P. C. Canfield, S. L. Bud'ko, and B. Cho, "Possible co-existence of superconductivity and weak ferromagnetism in $ErNi_2B_2C$," *Physica C: Superconductivity*, vol. 262, no. 3-4, pp. 249–254, 1996.

[59] F. Lévy, I. Sheikin, B. Grenier, and A. D. Huxley, "Magnetic field-induced superconductivity in the ferromagnet URhGe," *Science*, vol. 309, no. 5739, pp. 1343–1346, 2005.

[60] F. Lévy, I. Sheikin, B. Grenier, C. Marcenat, and A. Huxley, "Coexistence and interplay of superconductivity and ferromagnetism in URhGe," *Journal of physics. Condensed matter : an Institute of Physics journal*, vol. 21, no. 16, p. 164211, 2009.

[61] N. Huy, A. Gasparini, D. De Nijs, Y. Huang, J. Klaasse, T. Gortenmulder, A. de Visser, A. Hamann, T. Görlach, and H. v. Löhneysen, "Superconductivity on the border of weak itinerant ferromagnetism in UCoGe," *Physical Review Letters*, vol. 99, no. 6, p. 067006, 2007.

[62] T. Akazawa, H. Hidaka, T. Fujiwara, T. Kobayashi, E. Yamamoto, Y. Haga, R. Settai, and Y. Ōnuki, "Pressure-induced superconductivity in ferromagnetic UIr without inversion symmetry," *Journal of Physics: Condensed Matter*, vol. 16, no. 4, p. L29, 2004.

[63] C. Pfleiderer, M. Uhlarz, S. Hayden, R. Vollmer, H. v. Löhneysen, N. Bernhoeft, and G. Lonzarich, "Coexistence of superconductivity and ferromagnetism in the *d*-band metal $ZrZn_2$," *Nature*, vol. 412, no. 6842, pp. 58–61, 2001.

[64] M. Maple, "Experiments on magnetically-ordered superconductors," *Journal of Magnetism and Magnetic Materials*, vol. 31, pp. 479–483, 1983.

[65] D. J. Hykel, C. Paulsen, D. Aoki, J. R. Kirtley, and K. Hasselbach, "Magnetic fields above the superconducting ferromagnet UCoGe," *Phys. Rev. B*, vol. 90, p. 184501, Nov 2014.

[66] I. Sheikin, A. Huxley, D. Braithwaite, J. Brison, S. Watanabe, K. Miyake, and J. Flouquet, "Anisotropy and pressure dependence of the upper critical field of the ferromagnetic superconductor UGe_2," *Physical Review B*, vol. 64, no. 22, p. 220503, 2001.

[67] F. Hardy and A. Huxley, "p-wave superconductivity in the ferromagnetic superconductor URhGe," *Physical Review Letters*, vol. 94, no. 24, p. 247006, 2005.

[68] P. W. Anderson, "Theory of dirty superconductors," in *A Career In Theoretical Physics*, pp. 45–50, World Scientific, 1994.

[69] A. D. Huxley, "Ferromagnetic superconductors," *Physica C: Superconductivity and its Applications*, vol. 514, pp. 368–377, 2015.

[70] F. Hardy, D. Aoki, C. Meingast, P. Schweiss, P. Burger, H. v. Löhneysen, and J. Flouquet, "Transverse and longitudinal magnetic-field responses in the Ising ferromagnets URhGe, UCoGe, and UGe_2," *Physical Review B*, vol. 83, no. 19, p. 195107, 2011.

[71] J. Pospíšil, Y. Haga, S. Kambe, Y. Tokunaga, N. Tateiwa, D. Aoki, F. Honda, A. Nakamura, Y. Homma, E. Yamamoto, *et al.*, "Switching of magnetic ground states across the $UIr_{1-x}Rh_xGe$ alloy system," *Physical Review B*, vol. 95, no. 15, p. 155138, 2017.

[72] Y. Tokunaga, D. Aoki, H. Mayaffre, S. Krämer, M.-H. Julien, C. Berthier, M. Horvatić, H. Sakai, S. Kambe, and S. Araki, "Reentrant superconductivity driven by quantum tricritical fluctuations in urhge: Evidence from ^{59}Co NMR in $URh_{0.9}Co_{0.1}Ge$," *Physical Review Letters*, vol. 114, no. 21, p. 216401, 2015.

[73] V. Taufour, D. Aoki, G. Knebel, and J. Flouquet, "Tricritical point and wing structure in the itinerant ferromagnet UGe_2," *Physical Review Letters*, vol. 105, no. 21, p. 217201, 2010.

[74] H. Kotegawa, V. Taufour, D. Aoki, G. Knebel, and J. Flouquet, "Evolution toward quantum critical end point in UGe_2," *Journal of the Physical Society of Japan*, vol. 80, no. 8, p. 083703, 2011.

[75] N. Kabeya, H. Maekawa, K. Deguchi, N. Kimura, H. Aoki, and N. K. Sato, "Non-Fermi liquid state bounded by a possible electronic topological transition in $ZrZn_2$," *Journal of the Physical Society of Japan*, vol. 81, no. 7, p. 073706, 2012.

[76] S. Blundell, *Magnetism in Condensed Matter (Oxford master series in condensed matter physics)*. Oxford University Press, 2001.

[77] V. Taufour, U. S. Kaluarachchi, and V. G. Kogan, "Constraints on the merging of the transition lines at the tricritical point in a wing-structure phase diagram," *Physical Review B*, vol. 94, no. 6, p. 060410, 2016.

[78] S. Nakamura, T. Sakakibara, Y. Shimizu, S. Kittaka, Y. Kono, Y. Haga, J. Pospíšil, and E. Yamamoto, "Wing structure in the phase diagram of the Ising ferromagnet URhGe close to its tricritical point investigated by angle-resolved magnetization measurements," *ArXiv e-prints*, Aug. 2017.

[79] N. Giordano and W. Wolf, "Experimental study of the tricritical "wings" in dysprosium aluminum garnet," *Physical Review Letters*, vol. 39, no. 6, p. 342, 1977.

[80] T. Kirkpatrick and D. Belitz, "Third law of thermodynamics and the shape of the phase diagram for systems with a first-order quantum phase transition," *Physical Review Letters*, vol. 115, no. 2, p. 020402, 2015.

[81] S. Nakamura, T. Sakakibara, Y. Shimizu, S. Kittaka, Y. Kono, Y. Haga, J. Pospíšil, and E. Yamamoto, "Wing structure in the phase diagram of the Ising ferromagnet URhGe close to its tricritical point investigated by angle-resolved magnetization measurements," *Physical Review B*, vol. 96, no. 9, p. 094411, 2017.

[82] J. Black, *Lectures on the Elements of Chemistry, Delivered in The University of Edinburgh by the Late Joseph Black...* For A. Constable, and TN Longman & O. Rees, London, 1803.

[83] P. F. Sullivan and G. Seidel, "Steady-state, ac-temperature calorimetry," *Physical Review*, vol. 173, no. 3, p. 679, 1968.

[84] G. R. Stewart, "Measurement of low-temperature specific heat," *Review of Scientific Instruments*, vol. 54, no. 1, pp. 1–11, 1983.

[85] G. Ventura and M. Perfetti, *Thermal properties of solids at room and cryogenic temperatures*. Springer, 2016.

[86] N. E. Phillips, "Heat capacity of aluminum between 0.1 K and 4.0 K," *Physical Review*, vol. 114, no. 3, p. 676, 1959.

[87] A. Rost, *Magnetothermal Properties near Quantum Criticality in the Itinerant Metamagnet $Sr_3Ru_2O_7$, A thesis presented by*. PhD thesis, The University of St Andrews, 2009.

[88] Y.-S. Li, A. Gibbs, A. MacKenzie, C. Hicks, and M. Nicklas, "Heat capacity measurements of Sr_2RuO_4 under uni-axial stress," in *APS Meeting Abstracts*, p. L16.004, 2017.

[89] R. Bachmann, F. J. DiSalvo, T. H. Geballe, R. L. Greene, R. E. Howard, C. N. King, H. C. Kirsch, K. N. Lee, R. E. Schwall, H. U. Thomas, and R. B. Zubeck, "Heat capacity measurements on small samples at low temperatures," *Review of Scientific Instruments*, vol. 43, no. 2, pp. 205–214, 1972.

[90] M. Brando, "Development of a relaxation calorimeter for temperatures between 0.05 and 4 K," *Review of Scientific Instruments*, vol. 80, no. 9, p. 095112, 2009.

[91] R. Trainor, G. Knapp, M. Brodsky, G. Pokorny, and R. Snyder, "Low-temperature heat-pulse calorimetry for self-heating radioactive samples," *Review of Scientific Instruments*, vol. 46, no. 10, pp. 1368–1373, 1975.

[92] F. Pobell, "Chapter 12: Low-Temperature Thermometry," *Matter and Methods at Low Temperatures*, 2007.

[93] O. V. Lounasmaa, *Experimental principles and methods below 1K*. academic Press, 1974.

[94] G. Ventura and V. Martelli, "Thermal conductivity of Kevlar 49 between 7 and 290 K," *Cryogenics*, vol. 49, no. 12, pp. 735–737, 2009.

[95] J. Ekin, *Experimental techniques for low-temperature measurements: cryostat design, material properties and superconductor critical-current testing*. Oxford university press, 2006.

[96] R. A. Matula, "Electrical resistivity of copper, gold, palladium, and silver," *J. Phys. Chem.*, vol. 8, no. 4, 1979.

[97] W. Lawless, "Specific heat of nichrome, 2–30 K," *Cryogenics*, vol. 20, no. 9, pp. 527–528, 1980.

[98] D. Moy and A. C. Anderson, "Use of commercial metallic strain gauges as low temperature heaters," *Cryogenics*, vol. 23, no. 6, pp. 330–331, 1983.

[99] Y. E. Volokitin, R. C. Thiel, and L. J. de Jongh, "Heat capacity of thick-film resistor thermometers and pure RuO_2 at low temperatures," *Cryogenics*, vol. 34, no. 9, pp. 771–773, 1994.

[100] A. L. Dawson and D. Ryan, "Heat capacity of silver paint," *Review of scientific instruments*, vol. 67, no. 7, pp. 2648–2649, 1996.

[101] F. Du Chatenier and J. De Nobel, "Heat capacities of pure copper and silver and of dilute alloys of Cu, Ag, Zn, Mg and Al with transition metals of the first row at low temperatures," *Physica*, vol. 32, no. 6, pp. 1097–1109, 1966.

[102] M. Barucci, E. Gottardi, I. Peroni, and G. Ventura, "Low temperature thermal conductivity of Kapton and Upilex," *Cryogenics*, vol. 40, pp. 145–147, 2000.

[103] R. I. Amils, J. D. Gallego, J. L. Sebastián, S. Muñoz, A. Martín, and A. Leuther, "Thermal conductivity of silver loaded conductive epoxy from cryogenic to ambient temperature and its application for precision cryogenic noise measurements," *Cryogenics*, vol. 76, pp. 23–28, 2016.

[104] R. Goodrich, D. Hall, E. Palm, and T. Murphy, "Magnetoresistance below 1 K and temperature cycling of ruthenium oxidebismuth ruthenate cryogenic thermometers," *Cryogenics*, vol. 38, no. 2, pp. 221–225, 1998.

[105] K. Uhlig, "Magnetoresistance of thick-film chip resistors at milli-kelvin temperatures," *Cryogenics*, vol. 35, no. 8, pp. 525–528, 1995.

[106] K. Hasselbach, L. Taillefer, and J. Flouquet, "Critical point in the superconducting phase diagram of UPt_3," *Physical review letters*, vol. 63, no. 1, p. 93, 1989.

[107] J.-P. Brison, H. Suderow, P. Rodière, A. Huxley, S. Kambe, F. Rullier-Albenque, and J. Flouquet, "Transport in the superconducting phase of UPt_3 at low-temperature: magnetic field and impurity effects," *Physica B: Condensed Matter*, vol. 281, pp. 872–877, 2000.

[108] E. Miranda, V. Dobrosavljevic, and G. Kotliar, "Kondo disorder: a possible route towards non-fermi-liquid behaviour," *Journal of Physics: Condensed Matter*, vol. 8, no. 48, p. 9871, 1996.

[109] P. Hirschfeld, P. Wölfle, and D. Einzel, "Consequences of resonant impurity scattering in anisotropic superconductors: Thermal and spin relaxation properties," *Physical Review B*, vol. 37, no. 1, p. 83, 1988.

[110] T. Sakakibara, S. Kittaka, and K. Machida, "Angle-resolved heat capacity of heavy fermion superconductors," *Reports on Progress in Physics*, vol. 79, no. 9, p. 094002, 2016.

[111] G. L. Squires, *Introduction to the theory of thermal neutron scattering*. Cambridge university press, 2012.

[112] L. Van Hove, "Correlations in space and time and born approximation scattering in systems of interacting particles," *Physical Review*, vol. 95, no. 1, p. 249, 1954.

[113] A. D. Huxley and D. Sokolov, "Inelastic scattering upon URhGe." unpublished paper.

[114] V. Mineev, "Magnetic relaxation in uranium ferromagnetic superconductors," *Physical Review B*, vol. 88, no. 22, p. 224408, 2013.

[115] A. V. Chubukov, J. J. Betouras, and D. V. Efremov, "Non-landau damping of magnetic excitations in systems with localized and itinerant electrons," *Physical review letters*, vol. 112, no. 3, p. 037202, 2014.

[116] G. Shirane, P. Böni, and J. Wicksted, "Dynamics of itinerant ferromagnets above T_c," *Physica B+ C*, vol. 127, no. 1-3, pp. 264–270, 1984.

[117] F. Semadeni, B. Roessli, P. Böni, P. Vorderwisch, and T. Chatterji, "Critical fluctuations in the weak itinerant ferromagnet Ni_3Al: a comparison between self-consistent renormalization and mode-mode coupling theory," *Physical Review B*, vol. 62, no. 2, p. 1083, 2000.

[118] K. Yamada, Y. Todate, Y. Endoh, Y. Ishikawa, P. Böni, and G. Shirane, "Anisotropic spin fluctuations in the itinerant-electron ferromagnet MnP," *Journal of Applied Physics*, vol. 61, no. 8, pp. 3400–3402, 1987.

[119] G. Lonzarich and L. Taillefer, "Effect of spin fluctuations on the magnetic equation of state of ferromagnetic or nearly ferromagnetic metals," *Journal of Physics C: Solid State Physics*, vol. 18, no. 22, p. 4339, 1985.

[120] C. Stock, D. Sokolov, P. Bourges, P. Tobash, K. Gofryk, F. Ronning, E. Bauer, K. Rule, and A. Huxley, "Anisotropic critical magnetic fluctuations in the ferromagnetic superconductor UCoGe," *Physical Review Letters*, vol. 107, no. 18, p. 187202, 2011.

[121] J. Chang, E. Blackburn, A. T. Holmes, N. B. Christensen, J. Larsen, J. Mesot, R. Liang, D. A. Bonn, W. N. Hardy, A. Watenphul, M. v. Zimmermann, E. M. Forgan, and S. M. Hayden, "Funding report: Magnetic flux line structures and phase transitions in unconventional and conventional superconductors," tech. rep., University of Birmingham, 2012.

[122] "$Gras_{ANS}p$." `https://www.ill.eu/users/support-labs-infrastructure/software-scientific-tools/grasp/`. Accessed: 2018-09-06.

[123] D. Aoki, G. Knebel, and J. Flouquet, "Fermi surface instabilities in ferromagnetic superconductor URhGe," *Journal of the Physical Society of Japan*, vol. 83, no. 9, p. 094719, 2014.

[124] N. Bernhoeft and G. Lonzarich, "Scattering of slow neutrons from long-wavelength magnetic fluctuations in UPt_3," *Journal of Physics: Condensed Matter*, vol. 7, no. 37, p. 7325, 1995.

[125] F. Haslbeck, S. Säubert, M. Seifert, C. Franz, M. Schulz, A. Heinemann, T. Keller, P. Das, J. D. Thompson, E. D. Bauer, C. Pfleiderer, and M. Janoschek, "Interplay of itinerant and localized spin fluctuations in the ferromagnetic superconductor UGe_2," *ArXiv e-prints*, Jan. 2018.

[126] M. Taupin, G. Knebel, T. Matsuda, G. Lapertot, Y. Machida, K. Izawa, J.-P. Brison, and J. Flouquet, "Thermal conductivity through the quantum critical point in $YbRh_2$ Si_2 at very low temperature," *Physical Review Letters*, vol. 115, no. 4, p. 046402, 2015.

[127] "Depleted uranium." https://www.iaea.org/topics/spent-fuel-management/depleted-uranium#. Accessed: 2018-03-21.

[128] C. Truesdell and L. Euler, *The Rational Mechanics of Flexible Or Elastic Bodies, 1638-1788: Introduction to Leonhardi Euleri Opera Omnia Vol X Et XI Seriei Secundae*, vol. 11. Orell Füssli, 1960.

[129] "Kevlar aramid fiber - technical guide." http://www.dupont.co.uk/content/dam/dupont/products-and-services/fabrics-fibers-and-nonwovens/fibers/documents/Kevlar_Technical_Guide.pdf. Accessed: 2018-03-23.

[130] "Dupont^{TM} kapton." http://www.dupont.com/content/dam/dupont/products-and-services/membranes-and-films/polyimde-films/documents/DEC-Kapton-summary-of-properties.pdf. Accessed: 2018-03-21.

[131] E. Marquardt, J. Le, and R. Radebaugh, "Cryogenic material properties database," in *Cryocoolers 11*, pp. 681–687, Springer, 2002.